Applications of Quantum Metrology and Thermodynamics in Emerging Quantum Technologies

by

Ali Pedram

A Dissertation Submitted to the
Graduate School of Sciences and Engineering
in Partial Fulfillment of the Requirements for
the Degree of

Doctor of Philosophy

in

Physics

KOÇ ÜNİVERSİTESİ

June 4, 2024

Applications of Quantum Metrology and Thermodynamics in Emerging Quantum Technologies

Koç University

Graduate School of Sciences and Engineering

This is to certify that I have examined this copy of a doctoral dissertation by

Ali Pedram

and have found that it is complete and satisfactory in all respects,

and that any and all revisions required by the final

examining committee have been made.

Committee Members:

Prof. Özgür E. Müstecaplıoğlu (Advisor)

Assoc. Prof. Menderes Işkın

Prof. Adolfo del Campo

Date:

To the children of the night ...

ABSTRACT

Applications of Quantum Metrology and Thermodynamics in Emerging Quantum Technologies
Ali Pedram
Doctor of Philosophy in Physics
June 4, 2024

The emerging field of quantum technologies is poised to revolutionize various aspects of science, engineering, and computing. One of the most promising branches of quantum information sciences is quantum metrology, which plays a pivotal role in modern quantum technologies by enabling ultra-precise measurements that underpin their functionality and performance. At the heart of quantum metrology lies the exploitation of quantum resources such as entanglement which allow for unprecedented levels of sensitivity and resolution. Additionally, optimal design of quantum devices makes it necessary to study the fundamental principles governing energy transfer, work extraction, and entropy production in quantum systems. Hence, quantum thermodynamics offers profound insights into the efficiency limits of energy conversion processes, ultimately shaping the design of quantum technologies.

In this thesis, I review my five manuscripts, three of which are on optical quantum metrology and two of which are on thermodynamics of engineered quantum devices, which are presented in chapter 2 to chapter 6. In chapter 2, we calculate the precision bounds of Fock state optical probes for extracting information from an artificial neural network, which mimics the behavior of the retinal network. We shown that Fock state probes yield higher sensitivity than their coherent and thermal counterparts. In chapter 3 we investigate the precision bounds of polarization entangled Bell state for a polarimetric task. Theoretical calculations are accompanied by experimental data. We show that although entanglement provides quantum advantage in terms of precision, environmental noise introduces bias in the estimated values of the parameters which limits the mentioned advantage. In chapter

4 we calculate the precision bounds on estimation of rotation angle due to a birefringent medium in a general polarimetric setup. In our study we take into account several models of depolarization and ordering of polarimetric channels and include the effect of optical losses. Our results show that NOON state probes provide superior metrological performance compared with coherent and anticoherent states as depolarization as diattenuation of the probe is not strong. Even for relatively high depolarization rates, NOON state with small mean photon numbers yield a better precision bound compared with the coherent and anticoherent states.

In chapter 5 we investigate the effect of coupling strengths and coherence within a structured environment on the steady-state heat transfer in an engineered biomimetic system, using collision model for simulating the open quantum dynamics. We show that interaction with the environment modulates the energy levels of the system and decreases the transition energy between certain eigenstates, making these transitions more accessible to the hot thermal bath. In chapter 6 we implement counterdiabatic drive to accelerate adiabatic and hot isochoric branches of a quantum Otto engine. Our results for a single cycle show that, taking the control costs into consideration, the heat engine with both adiabatic and isochoric controlled branches reaches a higher power output, albeit with slightly reduced efficiency compared with the engine with counterdiabatic drive only implemented on its adiabatic strokes. However, in limit cycle, it is possible to allocate stroke durations such that the engine with both controlled adiabatic and isochoric branches operates with higher efficiency and power output. Finally, a detailed analysis and discussion of the results for all chapters is given in the conclusions section.

ÖZETÇE

Kuantum Teknolojilerinde Kuantum Metroloji ve Termodinamiğin Uygulamaları
Ali Pedram
Fizik, Doktora
10 Mayıs 2024

Kuantum teknolojileri ünvanında ortaya çıkan yeni alan, bilim, mühendislik ve bilgi işlem alanlarının çeşitli yönlerininde devrim niteliğinde gelişmelere yol açacaktır. Kuantum bilimlerinin en umut verici dallarından biri olan kuantum metroloji, modern kuantum teknolojilerinde anahtar rol oynayarak işlevselliklerini ve performanslarını temellendiren ultra hassas ölçümleri sağlayarak bu alana katkıda bulunuyor. Kuantum metroloji çerçevesinde klasik ölçümlerden çok daha yüksek bir hassasiyet ve çözünürlük seviyesinde ölçümleri mümkün kılan dolaşıklık gibi kuantum kaynaklardır. Ayrıca, kuantum cihazlarının optimal tasarımı, enerji transferi, iş çıkarma ve kuantum sistemlerdeki entropi üretiminin temel prensiplerinin incelenmesini gerektirir. Bu nedenle, kuantum termodinamiği, enerji dönüşüm süreçlerinin verimlilik sınırlarına dair derinlemesine anlayışlar sunar ve nihayetinde kuantum teknolojilerinin tasarımını şekillendirir.

Bu tez, 2. bölümden 6. bölüme sunulan beş makaleden oluşmaktadır. Bu makalelerin üçü optik kuantum metroloji ve ikisi kuantum cihazların termodinamği konularındaki araştırmalarımın sonuçlarıdır. 2. bölümde, retinanın fonksiyonal modelini temsil eden yapay bir sinir ağının fiziksel parametrelerinin ölçümü için Fock durumu ışığın hassasiyet sınırlarını hesapladık. Fock durumu optik prob, koherent ve termal problariyle kıyasta daha yüksek hassasiyet sağladığını gösterdik. 3. bölümde, polarizasyon dolaşıklı Bell durumunun bir polarimetrik görev için hassasiyet sınırlarını araştırıyoruz. Teorik hesaplamalar deneysel verilerle desteklenir. Dolaşıklığın hassasiyet açısından kuantum avantajı sağladığını gösteriyoruz, ancak çevresel gürültü, parametrelerin tahmin edilen değerlerinde yanlılık oluşturarak bu avantajı sınırlar. 4. bölümde, genel bir polarimetrik kurulumdaki bir bire-

fringent ortam nedeniyle dönme açısının tahmini üzerindeki hassasiyet sınırlarını hesaplarız. Çalışmamızda, depolarizasyon ve polarimetrik kanalların sıralanmasının çeşitli türlerini dikkate alırız ve optik kayıpların etkisini de içeririz. Sonuçlarımız, NOON durumu probunun, depolarizasyon ve diattenuasyonun güçlü olmadığı durumlarda, koherent ve antikoherent durumlarla karşılaştırıldığında üstün metrolojik performans sağladığını göstermektedir. Nispeten yüksek depolarizasyon oranları için bile, küçük ortalama foton sayılarına sahip NOON durumu, koherent ve antikoherent durumlarla karşılaştırıldığında daha iyi bir hassasiyet sınırı sağlar.

5. bölümde, yapay biyomimetik bir sistemdeki kararlı hal ısı transferi üzerinde yapılandırılmış bir ortamdaki bağlanma kuvvetlerinin ve koherensin etkisini inceliyoruz, açık kuantum dinamiklerini simüle etmek için çarpışma modelini kullanıyoruz. Ortamla etkileşim, sistemin enerji seviyelerini modüle eder ve belirli özdurumlar arasındaki geçiş enerjisini azaltır, bu geçişleri sıcak termal banyoya daha erişilebilir hale getirir. 6. bölümde, adyabatik ve sıcak izokorik branşları hızlandırmak için karşıdiyabatik kontrol uygularız. Tek bir döngü için sonuçlarımız, kontrol maliyetlerini dikkate aldığımızda, adyabatik ve izokorik kontrollü branşları olan Otto motorunun, sadece adyabatik vuruşlarında uygulanan karşıdiyabatik kontrol'ile kıyasta biraz azaltılmış verimlilikle daha yüksek bir güç çıkışına ulaştığını göstermektedir. Ancak, sınırlı döngüde, adyabatik ve izokorik dalgalanmaları olan motorun, daha yüksek verimlilik ve güç çıkışı ile çalışması için vuruş sürelerini tahsis etmek mümkündür. Son olarak, tüm bölümler için ayrıntılı bir analiz ve sonuçların tartışılması bölümünde sunulmuştur.

ACKNOWLEDGMENTS

First of all, I would like to express my sincere gratitude to my advisor, Prof. Özgür Esat Müstecaplıoğlun for giving me the opportunity to work on theoretic physics, even though I was originally trained as a mechanical engineer during my B.Sc. and M.Sc. years. Without his guidance, academic rigor, vision and most importantly kindness, patience and support, non of my works would be possible. I will benefit from what I learned from him, both within the context of academic work and generally in the context of attitude towards life and other people, for the rest of my life.

I would also like to thank Prof. Menderes Işkın, Prof. Alkan Kabakçıoğlu and Prof. Kaan Güven for the many lessons that they taught me during my courses and for enlightning and fun conversations that we had. Many thanks to Prof. Adolfo del Campo who accepted to be in my thesis committee and his many papers from which I benefited from during my PhD.

I want to thank my collaborators Prof. Onur Pusuluk, Prof. Barış Çakmak, Prof. Iannis Kominis, Prof. Frank Setzpfandt, Dr. Vira Besaga and Lea Gassab for their fruitful collaborations and insightful discussions. I am grateful to the present and past QuEST group members for their friendship and all the laughters that we shared (specially during the times that we shouldn't have laughed).

Finally, I have to thank my family for their kindness and continuous support throughout my life. Mom, dad, my twin sister and my niece, I love you all.

This thesis is based on the following papers and preprints by the author for the duration of doctoral studies.

- A. Pedram, Ö. E. Müstecaplıoğlu, and I. K. Kominis, Phys. Rev. Research 4, 033060 (2022)
- A. Pedram, V. R. Besaga, F. Setzpfandt, Ö. E Müstecaplıoğlu, arXiv:2402.11932 (2024)
- A. Pedram, V. R. Besaga, L. Gassab, F. Setzpfandt, Ö. E Müstecaplıoğlu, arXiv:2304.08258 (2024)
- A. Pedram, B. Çakmak, Ö. E Müstecaplıoğlu, Entropy 2022, 24(8), 1162 (2022)
- A. Pedram, S. C. Kadıoğlu, A. Kabakçıoğlu, Ö. E. Müstecaplıoğlu, New J. Phys. 25 113014 (2023)

Other papers and preprints by the author during PhD are:

- L. Gassab, A. Pedram, Ö. E. Müstecaplıoğlu, Eur. Phys. J. Plus 139, 379 (2024)
- A. Ullah, A. Pedram, M. T. Naseem, Ö. E. Müstecaplıoğlu, arXiv:2312.15691 (2023)
- A. Pedram, Ö. E. Müstecaplıoğlu, IJUC 18.1, p. 67-81 (2023)
- A. Pedram, O. Pusuluk, Ö. E. Müstecaphoglu, J. Phys.: Conf. Ser. 2191 012018 (2022)

TABLE OF CONTENTS

LIST OF FIGURES

ABBREVIATIONS

MSE	Mean Squared Error
FI	Fisher Information
QFI	Quantum Fisher Information
CRB	Cramer Rao Bound
CRLB	Cramer Rao Lower Bound
QCRB	Quantum Cramer Rao Bound
SQL	Standard Quantum Limit
HL	Heisenberg Limit
RNFL	Retinal Nerve Fiber Layer
CPTP	Completely Positive Trace Preserving
FMO	Fenna-Matthews-Olson
EET	Electronic Energy Transfer
RET	Resonance Energy Transfer
FRET	Förster Resonance Energy Transfer
HSE	Hierarchically Structured Environment
QHO	Quantum Harmonic Oscillator
QHE	Quantum Heat Engine
STA	Shortcuts to Adiabaticity
STE	Shortcuts to Equilibration
UNA	Uncontrolled Non-adiabatic
STÆ	Shortcuts to Adiabaticity and Equilibration

Chapter 1

INTRODUCTION

Quantum technologies represent the cutting edge of scientific and technological advancement, promising revolutionary breakthroughs across various fields. Rooted in the principles of quantum mechanics, these technologies harness the unique properties of quantum systems to manipulate information and physical processes in ways previously unimaginable. From quantum computing to quantum communication and sensing, the potential applications are vast and transformative. The importance of quantum technologies lies in their capability to transcend the limitations of classical approaches, offering unparalleled computational power, enhanced security, and unprecedented levels of precision. As classical computing approaches its fundamental physical limits, quantum computing emerges as a promising solution to tackle complex problems in areas such as cryptography, drug discovery, optimization, and materials science. Furthermore, quantum communication holds the promise of ultra-secure networks resistant to hacking and interception, revolutionizing the way information is transmitted and safeguarded.

In addition to computing and communication, quantum technologies also offer breakthroughs in sensing and metrology. With the rapid development of science and technologies, methods to perform measurements with higher precision become a hot issue in various research areas. Quantum metrology, also known as quantum parameter estimation, is a subject utilizing quantum resources including quantum correlation and quantum entanglement to do estimation on parameters with precision beyond the limit in classical schemes. Quantum sensors have the potential to detect minute changes in physical parameters with unprecedented sensitivity, enabling advancements in fields ranging from medical imaging to environmental monitoring and navigation systems. In an idealistic scenario, provided with N quantum-entangled probes, the mean squared error for estimating a phase-like parameter can achieve the Heisenberg limit, which is characterized by its $1/N^2$ scaling beyond the classical limit with $1/N$ scaling. As the optimal probe states and optimal measurements to be performed on the system being identified, the ultimate precision for quantum parameter estimation can be obtained, which is the most crucial problem in quantum metrology. If available, additional controls can be employed to achieve higher precision by optimizing the parameter-encoding process, such as eliminating the decoherence or correcting quantum errors.

Another research field which is gaining more ground with ongoing advancements in quantum technologies is quantum thermodynamics [Deffner and Campbell, 2019]. Quantum thermodynamics emerges as a relatively recent domain, blossoming into a dynamic sector of contemporary investigation. Its primary focus lies in elucidating the transformation of heat, work, and information within quantum systems. Analogous to classical thermodynamics, quantum thermodynamics employs idealized processes that universally delineate a broad spectrum of scenarios. Notably, the inception of the first quantum heat engine dates back to the late 1950s [Scovil and Schulz-DuBois, 1959]. However, it is only within the past decade or so that the literature concerning quantum thermal devices has truly burgeoned. This surge can be attributed to quantum heat engines offering straightforward, instructive portrayals of otherwise considerably intricate quantum scenarios. It's worth noting that thermodynamics emerged alongside the Industrial Revolution, originally aimed at comprehending and improving the efficiency of steam engines. Similarly, we find ourselves in a comparable era, sometimes dubbed the Second Quantum Revolution. Moreover, the proliferation of genuine quantum devices' inaugural experimental realizations further contributes to this expanding discourse.

In this thesis I utilize the frameworks of quantum metrology and quantum thermodynamics to address some of the problems which are relevant to the ongoing efforts in quantum technologies. A special emphasis is given to the optical quantum metrology, quantum polarimetry and thermodynamics of engineered quantum systems. The topics covered in this work are divided into five sections (chapter 2 to chapter 6) and the organization of thesis is as follows.

In chapter 2, we investigate the fundamental metrological capabilities of different quantum states of light to probe the retina, which is modeled using a simple neural network. Stimulating the rod cells by Fock, coherent and thermal states of light, and calculating the Cramer-Rao lower bound (CRLB) and Fisher information matrix for the signal produced by the ganglion cells in various conditions, we determine the volume of minimum error ellipsoid. Comparing the resulting ellipsoid volumes, we determine the metrological performance of different states of light for probing the retinal network. The results indicate that the thermal state yields the largest error ellipsoid volume and hence the worst metrological performance, and the Fock state yields the best performance for all parameters. This advantage persists even if another layer is added to the network or optical losses are considered in the calculations.

In chapter 3, we present a nonlocal quantum approach to polarimetry, leveraging the phenomenon of entanglement in photon pairs to enhance the precision in sample property determination. By employing two distinct channels, one containing the sample of interest and the other serving as a reference, we explore the conditions under which the inherent correlation between entangled photons can increase measurement sensitivity. Specifically, we calculate the quantum Fisher information (QFI) and compare the accuracy and sensitivity for the cases of single sample channel versus two channel quantum state tomography measurements. The theoretical results are verified by experimental analysis. Our theoretical and experimental framework demonstrates that the nonlocal strategy enables enhanced precision and accuracy in extracting information about sample characteristics more than the local measurements. Depending on the chosen estimators and noise channels present, theoretical and experimental results show that noise-induced bias decreases the precision for the estimated parameter. Such a quantum-enhanced nonlocal polarimetry holds promise for advancing diverse fields including material science, biomedical imaging, and remote sensing, via high-precision measurements through quantum entanglement.

In chapter 4, drawing inspiration from polarimetric investigations in biological tissues, we investigate the precision limits of polarization rotation angle estimation about a known rotation axis, in a quantum polarimetric process, comprising three distinct quantum channels. The rotation angle to be estimated is induced by the retarder channel on the Stokes vector of the probe state. The diattenuator and depolarizer channels, acting on the probe state, can be thought of as effective noise processes. We explore the precision constraints inherent in quantum polarimetry by evaluating the quantum Fisher information (QFI) for probe states of significance in quantum metrology, namely NOON, Kings of Quantumness, and Coherent states. The effects of the noise channels as well as their ordering is analyzed on the estimation error of the rotation angle to characterize practical and optimal quantum probe states for quantum polarimetry. Furthermore, we propose an experimental framework tailored for NOON state quantum polarimetry, aiming to bridge theoretical insights with empirical validation.

In chapter 5, inspired by the research works on quantum effects in photosynthetic light harvesting complexes and related engineered biomimetic systems, we explore the effect of an auxiliary hierarchically structured environment interacting with a system on the steady-state heat transport across the system. The cold and hot baths are modeled by a series of identically prepared qubits in their respective thermal states, and we use a collision model to simulate the open quantum dynamics of the system. We investigate the effects of system-environment, inter-environment couplings and coherence of the structured environment on the steady state heat flux and find that such a coupling enhances the energy transfer. Our calculations reveal that there exists a non-monotonic and non-trivial relationship between the steady-state heat flux and the mentioned parameters.

In chapter 6, we investigate the energetic advantage of accelerating a quantum harmonic oscillator (QHO) Otto engine by use of shortcuts to adiabaticity (for the expansion and compression strokes) and to equilibrium (for the hot isochore), by means of counter-diabatic (CD) driving. By comparing various protocols with and without CD driving, we find that, applying both type of shortcuts leads to enhanced power and efficiency even after the driving costs are taken into account. The hybrid protocol not only retains its advantage in the limit cycle, but also recovers engine functionality (i.e., a positive power output) in parameter regimes where an uncontrolled, finite-time Otto cycle fails. We show that controlling three strokes of the cycle leads to an overall improvement of the performance metrics compared with controlling only the two adiabatic strokes. Moreover, we numerically calculate the limit cycle behavior of the engine and show that the engines with accelerated isochoric and adiabatic strokes display a superior power output in this mode of operation.

1.1 Preliminaries of Classical and Quantum Parameter Estimation

The classical problem of parameter estimation can be described mathematically as follows: Suppose there's a random variable, X, governed by a probability distribution function, $p_\theta(x)$, where θ is an unknown parameter of interest. Sampling X, N times yields a dataset, $\boldsymbol{x} = x_1, x_2, ..., x_N$, comprising N independent identically distributed random variables X^N, following $p_\theta(x) = \prod_{i=1}^{N} p_\theta(x_i)$. To estimate θ, one must devise an estimator, $\hat{\theta}(\boldsymbol{x})$, which is a function of the dataset $\boldsymbol{x}$. It's worth noting that since $\boldsymbol{x}$ is a random variable, $\hat{\theta}(\boldsymbol{x})$ is also a random variable and possesses a mean value and variance. In the frequentist approach, θ is treated as a deterministic value, and thus the problem is tackled locally for this particular value. The quality of an estimator is evaluated by its mean squared error (MSE).

$$\Delta^2\hat{\theta} = \mathbf{E}\left\{(\hat{\theta}(\boldsymbol{x}) - \theta)^2\right\} \tag{1.1}$$

in which $\mathbf{E}$ denotes the expected value. Minimizing Eq. (1.1) gives the optimal estimator. An efficient estimator should output the true value of the parameter at least asymptotically. Hence, it is natural to assume that the estimator is unbiased, $\mathbf{E}(\hat{\theta}) = \theta$. Fisher information plays a central role in the theory of parameter estimation. It quantifies the amount of information given by a probability distribution about a parameter. It is formally defined as variance of score,

$$\mathcal{I} = \mathbf{E}\left\{(\frac{\partial}{\partial\theta}\log(p_\theta(x)))^2\right\}. \tag{1.2}$$

Here, the base of logarithm is e. If the probability distribution depends on more than one parameter, the Fisher information takes a matrix form. The parameters under consideration for our problem are the weight factors. For the multivariate parameter estimation case, we can write the Fisher information matrix as

$$[\mathcal{I}]_{i,j} = \mathbf{E}\left\{(\frac{\partial}{\partial\theta_i}\log(p_\theta(\boldsymbol{x})))(\frac{\partial}{\partial\theta_j}\log(p_\theta(\boldsymbol{x})))\right\}. \tag{1.3}$$

For single-parameter estimation the CRLB establishes a connection between the lower bound on the variance of unbiased estimators of the parameter and Fisher information as

$$\Delta^2\hat{\theta} \geq \frac{1}{N\mathcal{I}} \tag{1.4}$$

For multivariate case, if we take the estimator $\hat{\theta}$ to be unbiased, we have the following relation

$$\mathbf{cov}(\hat{\theta}) \geq [\mathcal{I}]^{-1}_{i,j}, \tag{1.5}$$

which means that $\mathbf{cov}(\hat{\theta}) - [\mathcal{I}]^{-1}_{i,j}$ is positive semidefinite. This is the statement of CRLB for the multivariate case. To understand the meaning of this statement, let us assume $\hat{\theta}$ is a Gaussian with zero mean; its probability density function is given by

$$p(\hat{\theta}) = \frac{exp[-\frac{1}{2}\hat{\theta}^T\mathbf{cov}^{-1}(\hat{\theta})\hat{\theta}]}{\sqrt{(2\pi)^N|\mathbf{cov}(\hat{\theta})|}}. \tag{1.6}$$

The contours of this probability distribution with equal value are given by

$$\hat{\theta}^T \mathbf{cov}^{-1}(\hat{\theta})\hat{\theta} = K. \tag{1.7}$$

In this equation, K is a constant which determines the size of the confidence region. Knowing that the covariance matrix is symmetric, it is easy to show that the mentioned contours are ellipsoids. With this insight, the geometric interpretation of CRLB for the case of multiple parameters is that the error ellipsoids formed using the covariance matrix of any unbiased estimator will be larger than the error ellipsoid formed using the inverse of Fisher information matrix. Hence, by comparing the sizes of error ellipsoids in different scenarios, we can compare their metrological capabilities. For the purpose of demonstrating some basic properties of error

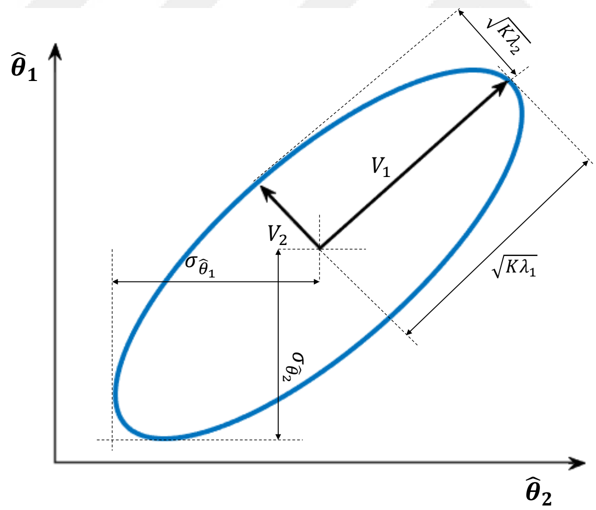

Figure 1.1: An error ellipse for two positively correlated parameters. The eigenvalues of the covariance matrix and the constant K which determines the size of the confidence region, are used to calculate the length of the axes. The SD of the parameters is proportional to the distance from the center.

ellipsoids, we take the two-dimensional case $\hat{\theta} = [\hat{\theta}_1 \quad \hat{\theta}_2]^T$ for which the confidence region will be elliptic. The semi major and semi minor axes of error ellipse are along the direction of eigenvectors of the covariance matrix and their sizes are given by $K\sqrt{\lambda_i}$ in which λ_i are the eigenvalues. The volume of an n-dimensional ellipsoid is given by the formula

$$V = \frac{\pi^{n/2}}{\Gamma(\frac{n}{2}+1)} M_1 M_2 ... M_n, \tag{1.8}$$

in which M_1 through M_n are principal axes and Γ is the gamma function. Since the axis lengths are given by

$$M_n = \sqrt{K\lambda_n}, \tag{1.9}$$

the expression for the volume of the error ellipsoid becomes

$$V = \frac{(K\pi)^{n/2}}{\Gamma(\frac{n}{2}+1)} \sqrt{\lambda_1 \lambda_2 ... \lambda_n}. \tag{1.10}$$

The SD of the parameters for the given covariance matrix is given by the distance between the center of the ellipse to the line parallel to the axes. If $\hat{\theta}_1$ and $\hat{\theta}_2$ are not correlated, the ellipse will be aligned with the axes, and the SD values will be the lengths of the semi-major and semi-minor axes. The error ellipse will be circular if they are uncorrelated and the SD for parameters is equal. If they are positively correlated (positive Pearson coefficient), the orientation of the error ellipse will be similar to Fig. 1.1.

Quantum parameter estimation involves applying the aforementioned strategies within quantum systems. Essentially, instead of employing classical probes, quantum ones can be utilized to leverage quantum effects and achieve greater precision. In quantum systems, the parameter estimation problem can typically be depicted as Fig. 1.2. Let's assume that we have a quantum system starting in an initial state ρ. To extract information about parameter θ, we encode θ into the quantum state by constructing a quantum evolution, ϵ_θ, that depends on θ. We then allow the density matrix to evolve under the action of the quantum channel. The evolution encodes the parameter on the density matrix and the final state becomes ρ_θ. After performing a quantum measurement, denoted as Π, on the resulting state ρ_θ, we obtain a measurement outcome with a probability that depends on both θ and the measurement Π. For a parameterized state the lower bound for the variance of any unbiased estimator $\hat{\theta}$ of the parameter, is given by the QCRB [Helstrom, 1967, Helstrom, 1968, Helstrom, 1969, Braunstein and Caves, 1994, PARIS, 2009, Sidhu and

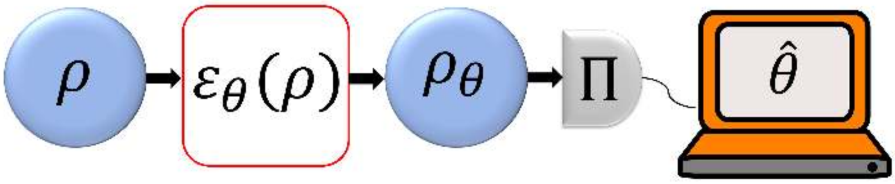

Figure 1.2: In order to estimate the parameter θ associated with a given quantum channel ϵ, the process begins by preparing a probe state ρ. Subsequently, the probe state evolves under the dynamics ϵ_θ, resulting in the final parametrized state ρ_θ. Following this evolution, quantum measurement is performed on the final state, yielding outcomes that are likewise dependent on θ. The final step involves constructing an estimator, $\hat{\theta}$, which utilizes the measurement outcomes to provide an estimation of the parameter θ.

Kok, 2020a]

$$(\Delta\hat{\theta})^2 \geq \frac{1}{N\mathcal{F}_Q(\theta)}. \tag{1.11}$$

Here, $\mathcal{F}_Q$ is the QFI and N is the number of measurement repetitions. QFI is a generalization of the classical Fisher information. For a pure state QFI is defined as,

$$\mathcal{F}_Q(\theta) = 4[\langle\partial_\theta\psi|\partial_\theta\psi\rangle - |\langle\partial_\theta\psi|\psi\rangle|^2]. \tag{1.12}$$

For a mixed state, one can define QFI using the symmetric logarithmic derivative (SLD) operator as

$$\mathcal{F}_Q(\theta) = \mathrm{Tr}[\hat{\rho}\hat{L}_\theta^2]. \tag{1.13}$$

SLD is implicitly defined by the following equation

$$\partial_\theta\hat{\rho} = \frac{\hat{L}_\theta\hat{\rho} + \hat{\rho}\hat{L}_\theta}{2}. \tag{1.14}$$

By expressing $\hat{L}_\theta$ in the eigenbasis of $\hat{\rho}$, one can write QFI as

$$\mathcal{F}_Q(\theta) = 2\sum_{k,l}\frac{|\langle k|\partial_\theta\hat{\rho}|l\rangle|^2}{\lambda_k + \lambda_l}. \tag{1.15}$$

Here, k, l and λ_k, λ_l are the eigenvalues and eigenvectors of $\hat{\rho}$.

Chapter 2

USING QUANTUM STATES OF LIGHT TO PROBE THE RETINAL NETWORK

2.1 Introduction: Limits of Human Vision

The minimum intensity of light for triggering visual experience has been a research topic for over a century. However, due to technological deficiencies, a reliable answer was not given until recent years. The earliest academic record investigating this question dates back to 1889 by Langley [Langley, 1889]. He used a bolometer to measure the minimum energy of light necessary for vision. Later on, researchers started investigating the minimum quanta of light for vision with the advent of quantum mechanics and understanding the quantum nature of light. One of the earliest studies on this topic was done by Lorentz [Bouman, 2012].

Vision experiments can be classified into two broad groups: psychophysical experiments and single-cell physiology experiments performed in-vitro. After dark adaptation, subjects are interrogated about their visual experience in psychophysical experiments, and conclusions are drawn by analyzing the answers. Hecht et al. showed that humans are capable of seeing as low as 5 to 7 photons [Hecht et al., 1942]. These types of experiments are usually called HSP experiments in the literature after the authors' initials. Van der Velden [van der Velden, 1946] showed that 2 photons are sufficient for visual perception. Barlow stated that the noise in the optical pathway influences the vision threshold [Barlow, 1956]. By rating the visual experience on a scale instead of a yes/no option and comparing the statistical characteristics of the light source and observer responses, Sakitt et al. [Sakitt, 1972] showed that humans could see single photons. Teich et al. studied the influence of controllable photon fluctuations on the response of the visual system [Teich et al., 1982a, Prucnal and Teich, 1982, Teich et al., 1982b] based on HSP type experiments. Holmes et al. [Holmes et al., 2017, Holmes, 2017] have utilized single-photon sources to study the temporal summation window of the human visual system. Vaziri et al. [Tinsley et al., 2016] performed a series of HSP experiments with a two-alternative forced-choice design and demonstrated that humans could detect single photons with a probability significantly above chance.

Physiological (in-vitro) experiments expose isolated photoreceptor cells to a dim flash of light and measure their electric response in a measurement circuit to study visual phototransduction [Rieke and Baylor, 1998]. Baylor et al. [Yau et al., 1977, Baylor et al., 1979a] were able to show that the extracellular membrane of the toad rod cells responds to single photons by electrical current in the order of pA. Later on, using in-vitro experiments and analyzing the statistical responses of the photocurrents, Baylor et al. showed that the rod cells of toads [Baylor et al., 1979b] and monkeys [Baylor et al., 1984] respond to single photons. Combining electrophysiological data and the results obtained from computational models of the visual signaling cascade, Reingruber et al. [Reingruber et al., 2013] showed that toad and mouse rods could detect single photons. Using a single-photon light source based on spontaneous parametric down-conversion (SPDC), which can produce a fixed number of photons, Krivitsky et al. demonstrated that the rod cells could measure the photon statistics of the stimulating light source [Sim et al., 2012] and later showed that the rod cells can indeed respond to single photons [Phan et al., 2014].

A deeper understanding of the visual system's response to few photons has led to several ideas exploring possible applications of the retina used as a photodetector. Creating new technologies, like introducing more secure biometric processes [Loulakis et al., 2017] and increasing the accuracy of retinal images using quantum imaging [Berchera and Degiovanni, 2019] are notable examples of these developments. Researchers also have designed possible experimental scenarios investigating the role of the human observer in quantum mechanics [Brunner et al., 2008, Dodel et al., 2017].

However, metrological capabilities and limitations of different quantum states of light within the context of the visual system are relatively unexplored. Furthermore, quantum mechanical studies of the visual system currently do not consider the sophisticated neural network structure of the retina. This work will synthesize the presently independent research directions of neural networks and quantum optical modeling of the visual system. Specifically, we will model the retina as a simple input-output model based on an artificial neural network. These types of models are widely used in computer vision and visual information processing and vision research communities [Glorot et al., 2011, Wen et al., 2017, Tran et al., 2015, Uchida et al., 2016, Kim et al., 2016, Lozano et al., 2018, McIntosh et al., 2016]. The goal is to derive the bounds on the estimation of the network parameters using different states of light, namely Fock, thermal, and coherent states. The network parameters chosen for this study are the weight factors of the neural network which effectively quantify the degree of dependence of the output on the corresponding input. The efficacy of these states to probe retinal network will be compared using standard measures of metrology and parameter estimation theory, Fisher information, and CRLB. The figure of merit for the metrological performance in our study for the error estimation is the inverse of the Fisher information in the single parameter problem and the volume of the error ellipsoid for the multiparameter problem. Our study shows that using Fock state light gives the lowest CRLB and smallest error ellipsoid for the considered range of parameters when using few number of photons and therefore the estimation error is smaller for this state. Practically, this result can mean that using quantum light sources that can produce few photon states, provides less noisy optical probes to explore retinal diseases relative to more traditional laser (coherent) or thermal light.

2.2 The Model

In the context of this work, we start with a relatively simple model to get a clear picture of the efficacy of various states of light. At this stage, we model transmission effects from photoreceptors to ganglion cells using a weight factor and ignore inhibitory neurotransmission effects within the retina. In our functional modeling of the retinal neural network, the weight factors do not correspond to a specific biological function of the real retina network. However, they can be seen as the fitting parameters of the responses of the retina based on a given input [Lozano et al., 2018, McIntosh et al., 2016]. We take the values for these parameters to be between zero and one, simply to reflect what fraction of the signal contributes to the output of the ganglion cell. Our model consists of an artificial neuron which is a two-layer neural network. A schematic picture of the model is given in Fig. 2.1.

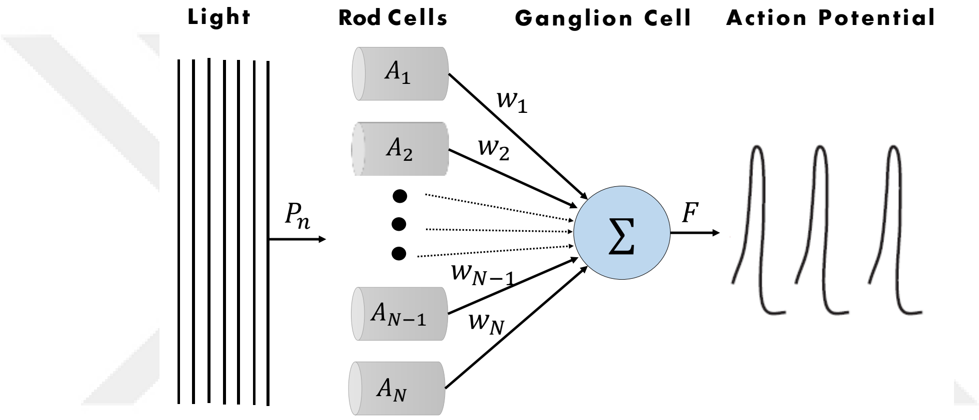

Figure 2.1: Neural network model of the retina. First, light illuminates the rod cells, causing them to produce a response. The weighted response of the rod cells is given as an input to the activation function of the ganglion cell, output of which is the action potential rate.

First, light in a certain state (with its corresponding photon distribution) illuminates the retina. The light then impinges on rhodopsin molecules of the rod cells, which in turn go through isomerization if they have detected any photon. It is evident from this description that the conditional probability distribution for isomerization of k molecules with an imperfect photodetection efficiency η by n photons is given by a binomial distribution [Gardiner, 1991]

$$P(k|n) = \binom{n}{k} \eta^k (1-\eta)^{n-k}. \tag{2.1}$$

Given that in most cases, instead of the number of photons, we deal with their probability distribution p_n, using the Bayes' rule, we can write the isomerization probability of k molecules as

$$P_I(k) = \sum_{n=0}^{\infty} P(k|n)p_n. \tag{2.2}$$

In this work we consider Fock, coherent and thermal states of light and their respective photon distributions are given by:

$$\begin{aligned} p_n^{(f)} &= \delta_{n,\bar{n}}, \\ p_n^{(c)} &= e^{-\bar{n}}\frac{\bar{n}^n}{n!}, \\ p_n^{(t)} &= \frac{\bar{n}^n}{(\bar{n}+1)^{n+1}}. \end{aligned} \tag{2.3}$$

in which $\bar{n}$ is the average photon number. In response to isomerization, photoreceptor cells produce photocurrents. The probability distribution for a photocurrent with amplitude A in response to k isomerizations is given by [Bialek, 2012]

$$P(A|k) = \frac{1}{\sqrt{2\pi(\sigma_D^2 + k\sigma_A^2)}} e^{-(A-k\bar{A}_0)^2/2(\sigma_D^2+k\sigma_A^2)}, \tag{2.4}$$

where $\bar{A}_0$ is the average of photocurrent, σ_A is the standard deviation (SD) of photocurrent amplitude for a single isomerization, and σ_D is the photocurrent SD in darkness. Applying Bayes' rule, we can obtain the probability distribution for photocurrent as

$$P(A) = \sum_{k=0}^{\infty} P(A|k)P_I(k). \tag{2.5}$$

After this stage, considering the input photocurrents, the ganglion cells produce an action potential to convey visual information to several regions of the brain. In this work, we have considered the activation function for action potential to be a rectified linear unit (ReLU) function. If the weighted sum of photocurrents is smaller than a certain threshold, T, then the action potential F is zero. Otherwise, it is proportional to the difference between this weighted input and the threshold. Here, we have neglected the saturation effect. The equation describing the action potential is

$$F(A_i, w_i, T) = \begin{cases} 0, & \sum w_i A_i \leq T; \\ \sum w_i A_i - T, & \sum w_i A_i \geq T. \end{cases} \tag{2.6}$$

Given the relationship between photocurrents and the rate of action potential and the probability distribution for photocurrents of single rod cells, we need to calculate $P(A_i)$ in order to calculate the probability distribution for F. If we assume that the wavefront of light is much larger than the dimension of the cells and the photoreceptor efficiency is small, we can make the calculations simpler. In this case, the probability that the photons cross any particular cell becomes negligible. Hence the expected number of isomerizations k is also small, i.e., $k \ll n$. So we can neglect the photon number change due to absorptions by each rod and consider that the probability distribution $P(A_i)$ for the current A_i produced by each rod cell is parameterized by the same photon number distribution p_n. So apart from the variable change, the probability distributions $P(A_i)$ are the same. The parameters are given in [Sim et al., 2012] fit into this description.

For large photoreceptor efficiencies, one rod cell might absorb a considerable fraction of the total impinging photons in its vicinity, reducing the number of available photons for the other rod cells. In this scenario Eq. (1) must be corrected in order to give a better expression for the effective probability distribution of photons sensed by each photoreceptor cell. For the case of two rod cells, if one of the cells has isomerized q molecules, then the other photoreceptor will have $n - q$ photons to isomerize its k molecules. Accordingly, we can write

$$P(k|n) = \sum_q \binom{n}{q} \binom{n-q}{k} \eta^{k+q} (1-\eta)^{2(n-q)-k}. \tag{2.7}$$

It is straightforward to generalize this expression for a larger number of rod cells. Using these distributions, we can calculate the probability distribution for action potential P_F. For the moment, let us consider the case for three rod cells. We can express the probability distribution of action potential as the convolution of probability distributions of photocurrents for each cell. For a single cell, since the action potential is given by the linear transformation of the photocurrent distribution, the probability distribution function for the action potential is given by

$$P_F(F) = \frac{1}{w} P_A(\frac{F+T}{w}). \tag{2.8}$$

For the details of derivation, the reader can refer to [Grimmett and Stirzaker, 2020]. For two cells, the action potential is given by the weighted sums of two random variables. Hence, we need to convolve the probability distributions of the rod outputs in order to obtain $P_F(F)$ [Grimmett and Stirzaker, 2020]. This takes into account every possible way that the weighted sum of the photocurrents of the rods equals to the certain value of F

$$P_F(F) = \frac{1}{w_1 w_2} \int_{-\infty}^{\infty} P_{A_1}(\frac{X}{w_1}) P_{A_2}(\frac{F+T-X}{w_2}) dX. \tag{2.9}$$

For n cells, in order to obtain the probability distribution for action potential, we need to calculate the convolution of $A_1, A_2, ..., A_n$.

2.3 Optical Losses

As light travels through the eyes, some of the photons get absorbed by the various materials in the eyes, some of them are reflected, and the remaining photons are transmitted. Presence of optical losses affects the number (and in some cases the distribution) of the photons on the retina. To model the optical losses, we will use the biological photodetector model presented in 2.2 preceded by a beam splitter [Loudon, 2000]. Quantum mechanically, each port of the beam splitter is modeled using creation and annihilation operators as shown in Fig. 2.2.

The photons are sent through port 1. Port 2 is empty (contains vacuum). The photons are transmitted to the retina through port 3, and the photons in port 4 are discarded. The transformation relations between the input and output ports can be written in matrix form [Gerry and Knight, 2004]. Elements of the transformation matrix M are limited by the commutation relations of the field operators and conservation of energy. In this work, we take the beam splitter matrix to be

$$M = \begin{pmatrix} \sqrt{u} & i\sqrt{1-u} \\ i\sqrt{1-u} & \sqrt{u} \end{pmatrix}, \tag{2.10}$$

in which u is the transmission parameter of the beam splitter. Using these transformations, we can find the state of port 3 given any state we choose to input in

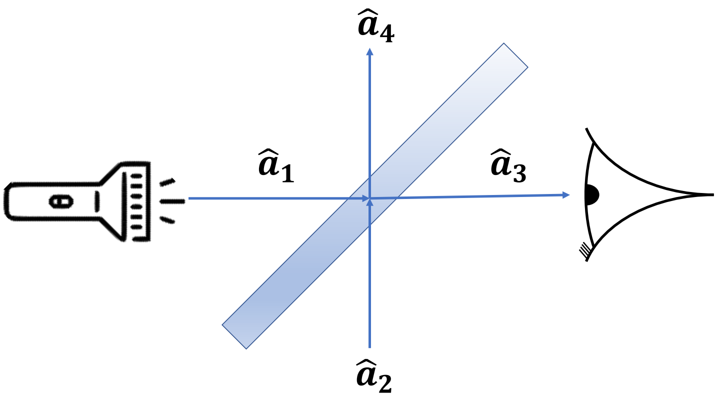

Figure 2.2: Schematic view of the quantum beam splitter. $\hat{a}_i$ are the annihilations operators of their respective ports. In our scheme, the light is sent to the eye through port 1. The port 2 is empty (vacuum state). The output port 4 is discarded, which amounts to the experienced optical loss. The photons coming out of output 3, are sent to the retina.

port 1. Then, by writing the state in port 3 in number basis, we can obtain the photon statistics after optical losses. For example, Fock state light with n photons undergoes the following transformation in the beam splitter.

$$|n\rangle_1 |0\rangle_2 = \frac{1}{\sqrt{n!}}(\hat{a}_1^\dagger)^n |0\rangle_1 |0\rangle_2 = \frac{1}{\sqrt{n!}}(\sqrt{u}\hat{a}_3^\dagger + i\sqrt{1-u}\hat{a}_4^\dagger)^n |0\rangle_3 |0\rangle_4 . \tag{2.11}$$

Expanding using the binomial theorem, we find

$$|n\rangle_1 |0\rangle_2 = \sum_{m=0}^{n} \sqrt{\frac{n!}{m!(n-m)!}} \sqrt{u}^m (i\sqrt{1-u})^{n-m} |m\rangle_3 |n-m\rangle_4 . \tag{2.12}$$

Hence, the initial number state transforms into a linear superposition of number states conserving the total photon number. Thus, for each $m < n$, the photon distribution for the Fock state light received by the retina after going through the beam splitter becomes

$$p_m^{'(f)} = \frac{n!}{m!(n-m)!} u^m (1-u)^{n-m}. \tag{2.13}$$

Applying the same procedure for coherent and thermal states we find that the probability distribution of photons in port 3 for the coherent and thermal states as having the same form as Eq. (5.3) with the average photon number modified by a factor of u.

2.4 Results

This section compares the efficacy of the Fock, coherent and thermal states of light for probing retinal network in various conditions using the framework described in the previous section. The simulations are performed for multiple photoreceptor cells in lossy and lossless conditions and consider variations in key parameters to study different parametric regimes and better understand the underlying effects. In all of our calculations σ_D, σ_A, $\bar{A}_0$ and T are taken to be $0.15pA$, $0.5pA$, $0.7pA$ and $0.1pA$ respectively. These parameters are taken from the seminal work by Krivitsky et al. [Phan et al., 2014]. We will use the volume given by Eq. (1.9) as the criterion for metrological performance, which describes the overall estimation errors for all parameters. Our objective is to characterize total estimation errors using CRLB without having to deal with specific metrological procedures. Minimization of this volume corresponds to maximization of the determinant of the information matrix. For constructing the error ellipsoids, a 99% confidence region is used.

2.4.1 In-Vitro Metrology of the Retina

For in-vitro setup, it is desirable to find the response of the retina to a few photons. In this section we will assume that the optical losses are negligible ($u = 1$). First, we check how a single cell model behaves within our framework. In Fig. 2.3 the results for CRLB vs weight factors is given for different states of light for $n = 1$ and $n = 5$ given that the photoreceptor efficiency is $\eta = 0.4$. Here, CRLB in the vertical axes denote the Cramer-Rao lower bound calculated for the corresponding states which is given by the reciprocal of the Fisher information.

It is clear that the thermal state gives the largest result for CRLB and the Fock state provides a better metrological advantage compared to thermal and coherent states throughout the parametric regime. It is also obvious that for $\bar{n} = 5$ the overall performance is better for all states compared to $\bar{n} = 1$. Performing the same

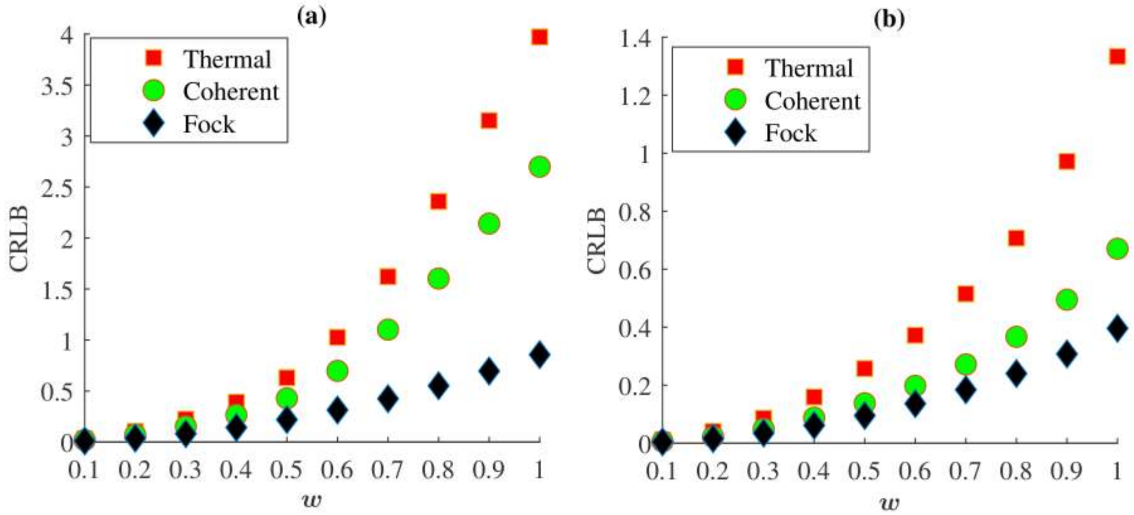

Figure 2.3: CRLB vs w for $\eta = 0.4$. (a) $\bar{n} = 1$ (b) $\bar{n} = 5$.

calculations using different photoreceptor efficiencies and average photon numbers show that the discrepancy between the Fock and coherent states becomes larger for higher η and smaller for higher $\bar{n}$. Hence, the Fock state light is particularly useful for low-photon imaging and metrology of the retina where it is desirable to avoid strong probe signal intensities in order to decrease the noise. In general, a lower overall value for CRLB is obtained using the Fock state and for the larger photon numbers and photoreceptor efficiencies. This can also be understood by analyzing the properties of the input signal of the ganglion cell with different mean number of photons. From Eq. (5.8) it is clear that for the case of single rod cell, the mean and the variance of the input photocurrent (A) and the output of the ganglion cell (F) are related by the weight factor (w). Hence, for a poor signal quality with high uncertainty in the input we will get an output signal with high uncertainty and therefore the estimation error for w will be higher. Using the probability distribution in Eq. (5.7) we can define the expected value, variance and signal to noise ratio (SNR) of A as:

$$\begin{aligned} E(A) &= \int_0^{A_{max}} P(A) A dA \\ \mathrm{Var}(A) &= \int_0^{A_{max}} P(A) A^2 dA - E(A)^2, \\ \mathrm{SNR}(A) &= \frac{E(A)}{\sqrt{\mathrm{Var}(A)}} \end{aligned} \tag{2.14}$$

in which A_{max} is the maximum of the photocurrent amplitude used in the calculations. Using $SNR(A)$ as a figure of merit for the quality of the photocurrent signal we give the SNR of the total photocurrent for different values of the mean photon number in Fig. 2.4 It is also evident from Fig. 2.4 that increasing the mean number

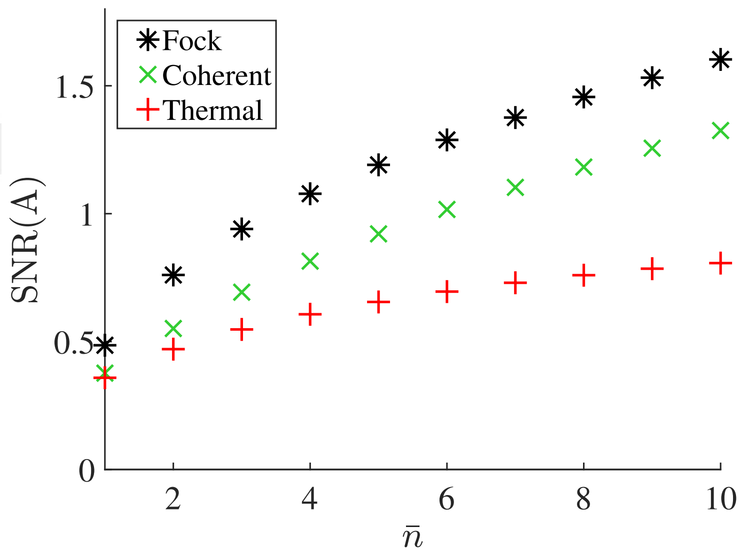

Figure 2.4: SNR of the total photocurrent for different values of the mean photon number.

of photons results in a higher $SNR(A)$. This result is also expected from the form of Eq. (5.6). For a larger $\bar{n}$ more molecules will be isomerized. From Eq. (5.6), variance and mean of the photocurrent per photoisomerization scales with k, which means that for a single isomerization event the SNR scales as k. In conclusion, for this specific classical parameter estimation problem we see that the Fock state light results in smaller error when used as a probe. Additionally, if we assume that we have a 2-layer neural network with N-cells for which all the respective weight factors always take the same value ($w_i = w_j$), then they can't be treated as separate random variables and the problem reduces to a single parameter estimation problem. This effectively means that we can fit the output data of the network to the input data using a single parameter. So, all the results obtained for the single parameter estimation scenario so far can be applied to this problem as well. It is worth mentioning that the optimality of Fock state for other quantum estimation problems involving transmission or loss scenarios and intensity-sensitive measurements is also well established [Monras and Paris, 2007, Adesso et al., 2009].

In contrast, for the cases where $w_i \neq w_j$ for any i and j as shown in Fig. 2.1, we need to treat each weight factor as an individual random variable and find the area/volume of the error ellipse/ellipsoid, which describes the collective estimation errors of all parameters. In these cases, the problem is a genuine multiparameter estimation problem. Fig. 2.5 and Fig. 2.6 show the logarithm of volume for minimum error ellipsoids for the Fock, coherent and thermal states with mean photon number of 1 and 5 and rod cells with $\eta = 0.4$.

It is evident that the thermal state performs considerably worse than the coherent and Fock states, and the Fock state has a smaller error ellipse area than the coherent state. The volume of the error ellipses increases with the weight factors w. Hence the better performance is achieved for lower weight factors. This is also suggested by the form of the probability distribution given in Eq. (5.10) and Eq. (2.9) in which the inverse of the weights appears as the coefficient of the distribution.

Since this analysis is valid for any line on the w-plane, we can choose a line on this plane and compare the error bounds for the three states on that line. This approach is beneficial for a larger number of rod cells since it is not feasible to compare more than two-rod cells graphically. In Fig. 2.7 for example, the area for minimum error ellipses are shown for $w_2 = 0.7w_1$ and photoreceptor efficiency of $\eta = 0.4$. The horizontal axis is taken to be $w_1 = w$. This image is a cross-sectional

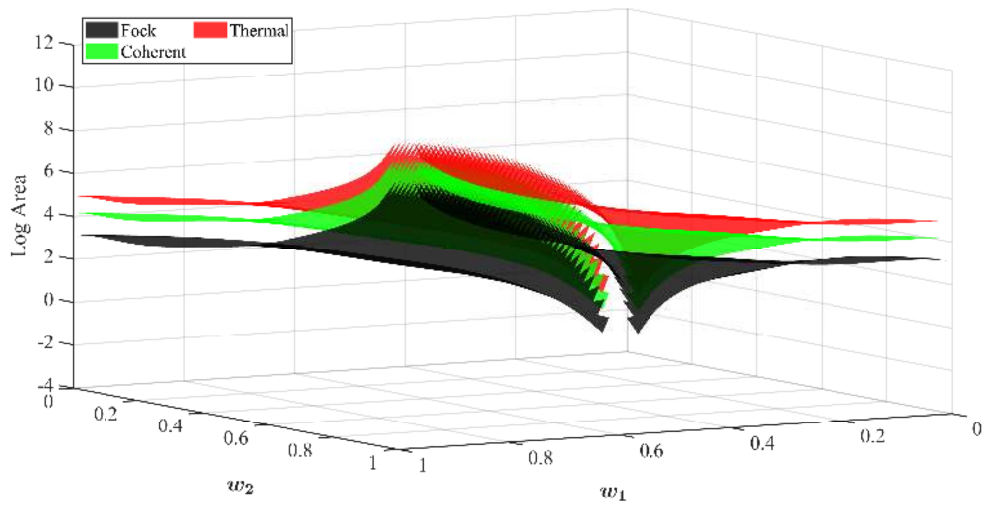

Figure 2.5: Minimum error ellipse area for $\eta = 0.4$ and $\bar{n} = 1$ for the whole domain of weight factors ($w_1 \neq w_2$).

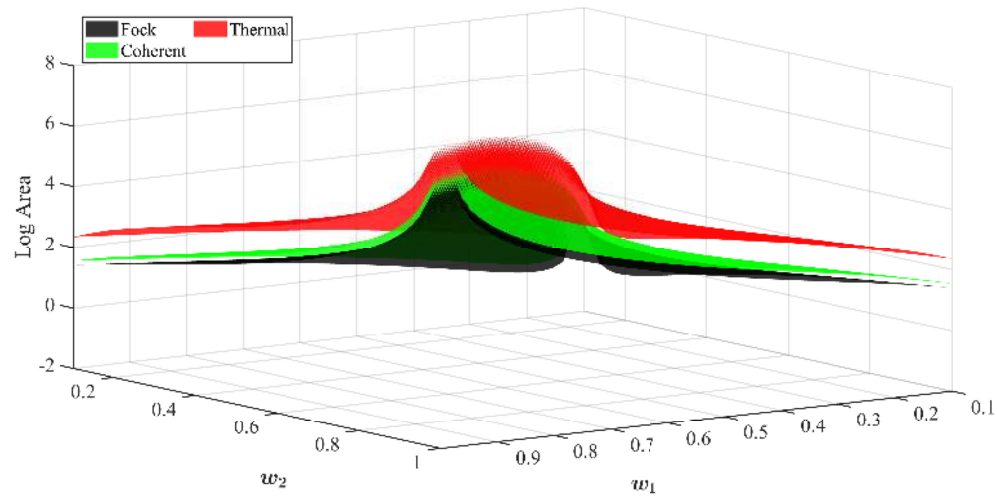

Figure 2.6: Minimum error ellipse area for $\eta = 0.4$ and $\bar{n} = 5$ for the whole domain of weight factors ($w_1 \neq w_2$).

view of Fig. 2.5 and Fig. 2.6. As it is seen in Fig. 2.7, for a larger $\bar{n}$, the advantage that the Fock state has over the coherent state is smaller. However, for small $\bar{n}$, the difference in their performance becomes more and more considerable.

The same trend exists for higher number of rod cells. As an example, for the case of 3 cells, in Fig. 2.8 the error ellipsoid volumes for different states of light are compared when the average photon number is set to $\bar{n} = 1$. The weight factors are chosen such that $w_2 = 0.5w_1$ and $w_3 = 0.7w_1$. Similarly to the previous case, the horizontal axis is $w_1 = w$. As it was the case for two rod cells, Fig. 2.8 shows that the Fock state and coherent state outperform the thermal state after we add another cell to the layer. Unlike the previous figures, the vertical axis in Fig. 2.8 is denoted as "Log Volume" simply because for 3 independent parameters, we will have an error ellipsoid (not an ellipse) and its size is characterized by volume (not area). For a higher number of rod cells, we get similar results. The calculations are done using various ratios of the weight factors, and in all cases, similar results are obtained.

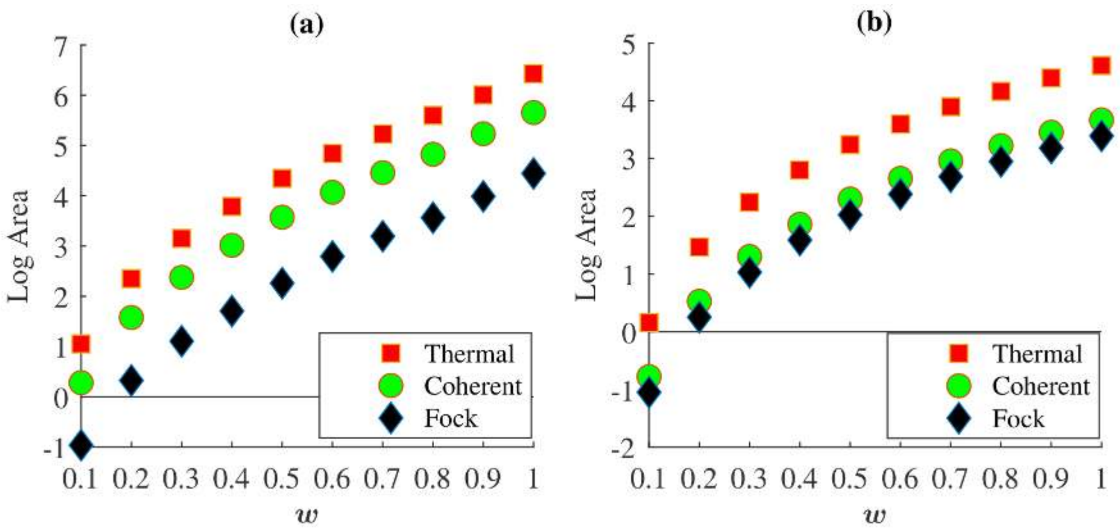

Figure 2.7: Minimum error ellipse area for $w_2 = 0.7w_1$ and $\eta = 0.4$. (a) $\bar{n} = 1$ (b) $\bar{n} = 5$.

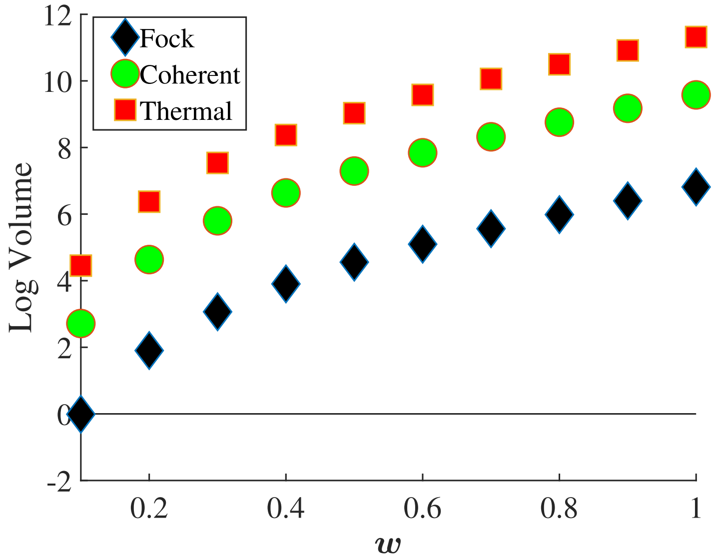

Figure 2.8: Minimum error ellipsoid volume for $w_2 = 0.5w_1$, $w_3 = 0.7w_1$ and $\eta = 0.4$ and $\bar{n} = 1$.

In order to have a more detailed description of the retina, now we add another layer in between the rod and ganglion cells which will account for the function of the bipolar cells as shown in Fig. 2.9. Like the ganglion cells, the bipolar cells are modeled using a ReLU function.

In this 3-layer network, the rod cells produce photocurrent upon interacting with photons and these photocurrents are directed to the bipolar cells. The outputs of the bipolar cells are determined by sum of the photocurrents and hence their probability distributions are given by the convolution of their respective input photocurrent probability distributions. Finally, the output of the ganglion cell is given by the weighted sum of the signals of the bipolar cells and therefore the probability distribution for the action potential will be given by the convolution of the bipolar cell distributions. Hence, we have 2 convolution steps in this model. Our goal is to calculate an estimate for the total error in this network for the parameters w_i, which are the weights of the input to the ganglion cells, as was the case for the 2-layer network. In Fig. 2.10 the results for the simplest 3-layer model with four rod cells

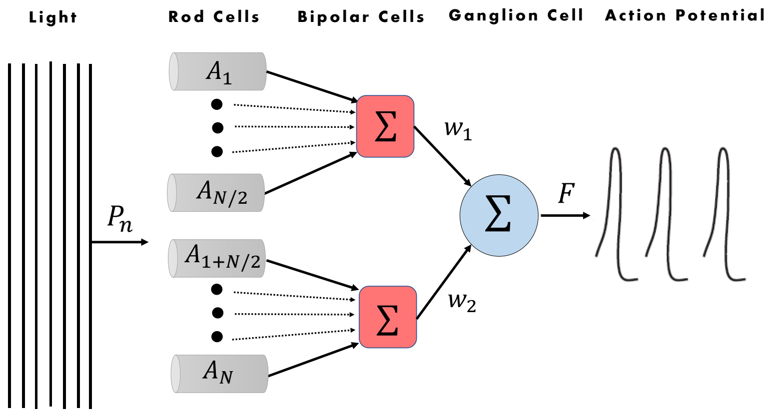

Figure 2.9: Schematic illustration for the 3-layer neural network model of the retina. The weighted sum of the photocurrents produced by the rod cells are given as an input to the bipolar cells. Then, the output of the bipolar cells is sent to the ganglion cell, the output of which is the action potential.

and two bipolar cells are given. The average photon number used is $\bar{n} = 5$, and the activation threshold for the bipolar cells is chosen to be zero. The results are consistent with the ones obtained previously.

2.4.2 In-Vivo Metrology of the Retina

Now, assume that we want to investigate the retina in-vivo using light pulses and record the response of the ganglion cells. In this case the optical losses become significant because the photons need to pass through a medium before targeting the rod cells ($u < 1$). In this scenario, the probing light signals must contain a higher number of photons on average for the effective stimuli to reach the rod cells after experiencing optical losses. Using the beam splitter framework describing the optical losses and given the transmission parameter u, which is taken to be 0.5 in our calculations, we find the probability distribution of photons after passing through the beam splitter for Fock, coherent and thermal input states. Assuming that the photoreceptor cells have an efficiency of $\eta = 0.4$, we want to check if the advantage of quantum states of light still holds once we introduce optical losses. In Fig. 2.11

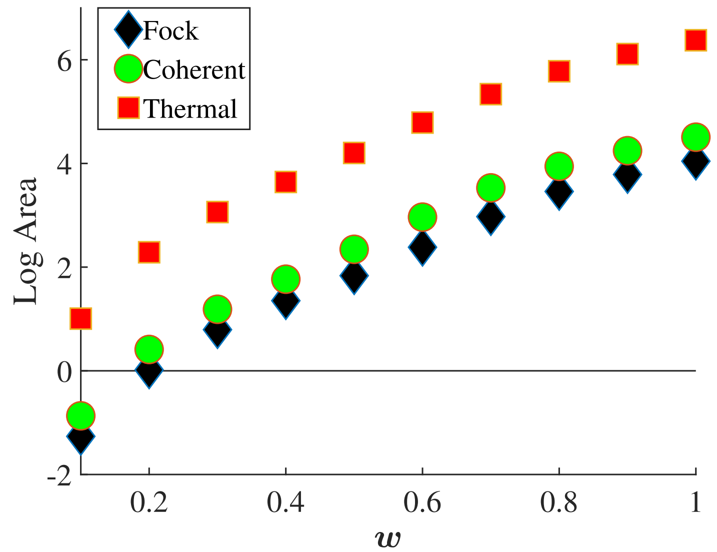

Figure 2.10: Minimum error ellipse area for the 3-layer network. $w_2 = 0.7w_1, w_1 = w$, $\bar{n} = 5$ and $\eta = 0.4$.

the CRLB is given for a network with a single rod cell.

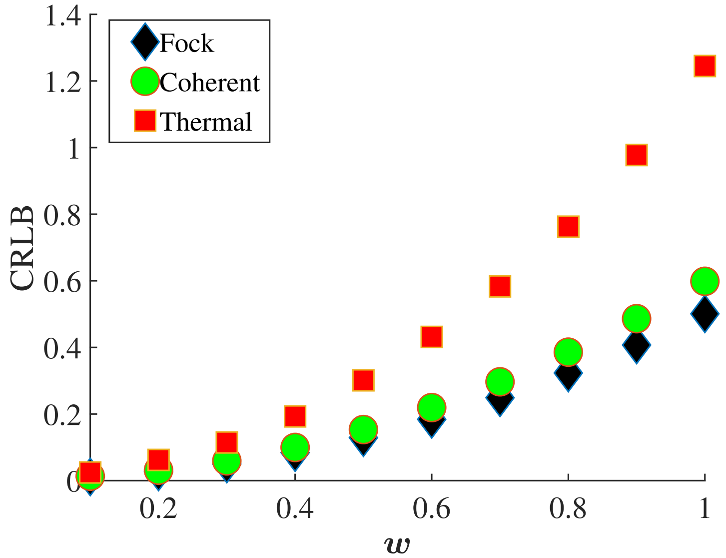

Figure 2.11: CRLB vs w for $\eta = 0.4$ and $\bar{n} = 10$ including optical losses.

Comparing Fig. 2.11 and Fig. 2.3 we see that similar to the case with no optical losses, coherent and Fock states give a smaller value for CRLB. This shows that the advantage of the Fock state persists even after optical losses alter its photon distribution. In order to analyze the effect of optical losses on unequal weight factors, as an example, the case for two rod cells is demonstrated in Fig. 2.12.

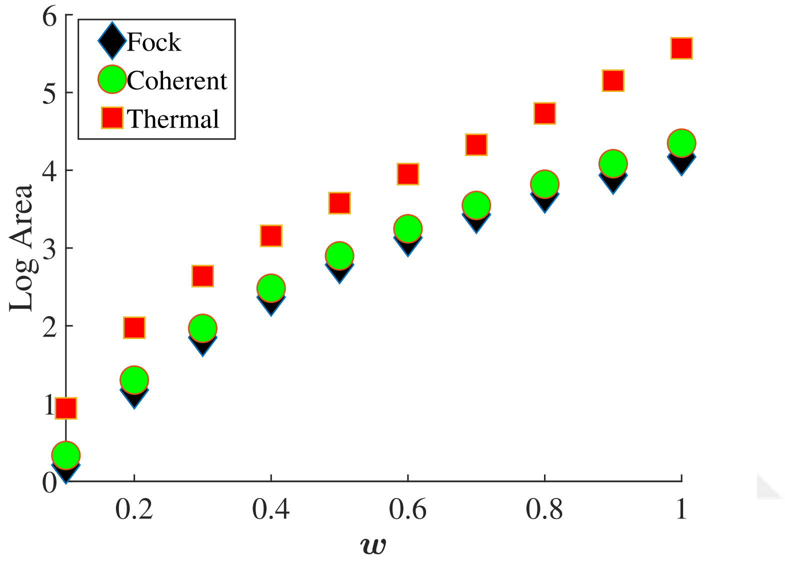

Figure 2.12: Minimum error ellipse area for $w_2 = 0.8w_1$, $\eta = 0.4$ and $\bar{n} = 10$ including optical losses.

As expected, the trend is similar to the case with no optical losses. The area for the error ellipse is the largest for the thermal state and the smallest for the Fock state. We can conclude that the quantum states of light have better metrological capabilities even if optical losses are introduced. Calculation of the error ellipsoid volume for more rod cells and more complicated network topologies (3-layer network) gives similar results.

Adding optical losses results in a decrease in the mean number of photons and (for the case of Fock state) change in the photon distribution function. So the net effect of the loss is that it decreases the number of photons available for isomerization. Our calculations for this case show that similar to the case with no losses, an increase in the mean photon number enhances the metrological performance. It is also worth mentioning that even when optical losses are included, probing the retina using light in the Fock or coherent states results in a smaller overall error than the thermal state. Performance enhancement of the Fock state over coherent and thermal states in our in-vivo metrology calculations suggests that there is a possibility of developing more accurate effective neural network models of the retina using Fock state light in order to stimulate it. One can use an electroretinogram or as recently suggested, optically pumped magnetometers [Westner et al., 2021] in order to measure the response of the retina to the photonic stimuli and statistically infer more accurate effective network parameters for retina modeling using Fock state light compared with thermal and coherent states.

Chapter 3

NONLOCALITY ENHANCED PRECISION IN QUANTUM POLARIMETRY VIA ENTANGLED PHOTONS

3.1 Introduction: Entanglement-Assisted Metrology

The concept of light polarization is fundamental, depicting the directional behavior of electric field oscillations within the electromagnetic context. In cases where light encompasses diverse polarization states, it remains unpolarized. Polarizers, materials adept at transforming unpolarized light into a single polarization, play a vital role in this context. Meanwhile, analyzing how light's polarization evolves upon interaction with materials offers insights into their inherent properties, forming the core of polarimetry [Vitkin et al., 2015a, He et al., 2021a].

In the realm of contemporary metrology, the pursuit of refined techniques for enhancing precision measurements is unceasing. One intriguing avenue is quantum enhanced metrology in which the goal is to use quantum resources such as entanglement and squeezing, for transcending classical precision bounds [Caves, 1981, Ma et al., 2011, Engelsen et al., 2017, Nagata et al., 2007, Israel et al., 2014a, Giovannetti et al., 2006, Pezzè et al., 2018, Giovannetti et al., 2004]. Entangled photon pairs, generated through processes like spontaneous parametric down-conversion [Burnham and Weinberg, 1970, Hong and Mandel, 1985], have enabled remarkable applications in quantum communication and cryptography [Brendel et al., 1999, Bennett et al., 1993, Bouwmeester et al., 1997, Furusawa et al., 1998, Long and Liu, 2002, Deng et al., 2003, Kimble, 2008, Luo et al., 2023]. Due to this fact, quantum entanglement, a phenomenon where particles achieve intrinsic correlation regardless of spatial separation, has captured particular attention in optical quantum metrology and it is revealed that prudent use of entanglement can be effective in mitigating classical noise, potentially elevating precision beyond classical limits [Dowling, 2008, Cable and Durkin, 2010, Berry et al., 2009, Cappellaro et al., 2005, Wolfgramm et al., 2013a, Demkowicz-Dobrzański and Maccone, 2014, Czekaj et al., 2015, Zhang et al., 2015, Augusiak et al., 2016, Huang et al., 2016, Wang et al., 2018, Long et al., 2022]. This leads to the natural question, whether the integration of quantum entangled light could potentially amplify the precision of polarimetric measurements.

To reveal the sensitivity of quantum states of light for estimating physical parameters of optical samples one needs to treat light-matter interaction in a fully quantum manner. To this end attempts have been made to describe the polarization states within the framework of quantum optics [Luis, 2016, Luis and Sánchez-Soto, 1993, Shumovsky and Müstecaplıoğlu, 1998, Luis, 2005, Söderholm et al., 2012, Goldberg et al., 2021a]. It is well established that the classical definition for degree of polarization fails to capture polarization characteristics of quantum states of light and quantum states can contain so called "hidden polarization" or higher order polarization to which higher moments of the Stokes vectors contribute. Several works have been published to demonstrate the discrepancy between quantum and classical concepts of polarization and also new measures for quantifying the quantum degree of polarization have been proposed [Klyshko, 1992, Alodjants and Arakelian, 1999, Luis, 2002, Klimov et al., 2005, Luis, 2007b, Klimov et al., 2010, Björk et al., 2010, Luis, 2007a, Iskhakov et al., 2011, Nogueira et al., 2013, Kothe et al., 2013, Sánchez-Soto et al., 2013].

One can describe polarization transformation of light interacting with a medium using Jones calculus or more generally using Mueller calculus [Hecht, 2017]. Interaction of the optical signal with a medium can induce various effects on the signal including attenuation due to absorption or reflection, diattenuation of the signal due to dichroism, rotation of its Stokes vector due to birefringence or depolarization due to random scattering. In the classical theory of polarimetry, in case that the Mueller matrix is not singular, the Lu-Chipman decomposition (polar decomposition) can be utilized to effectively establish an input-output relation between input and output Stokes vectors decomposing the original Mueller matrix into three elementary matrices with well defined optical properties and parameterized by their respective physical parameters (rotation angles, depolarization factors, etc.) [Lu and Chipman, 1996a]. It is important to note that there has been attempts to generalize the framework of classical Mueller polarimetry and ellipsometry into the quantum domain [Goldberg, 2020, Rudnicki et al., 2020]. Finding the ultimate measurement sensitivity of these parameters using optimal quantum probes and measurements is of utmost importance. It is shown that NOON states and anti-coherent states can saturate the Heisenberg limit for rotation sensing [Kolenderski and Demkowicz-Dobrzanski, 2008, Goldberg and James, 2018, Martin et al., 2020, Goldberg et al., 2021b, Goldberg et al., 2023, Eriksson et al., 2023]. The problem of rotation sensing is also studied considering different polar decompositions with optical depolarization and diattenuation noise channels [Pedram et al., 2024a]. Furthermore, Fock and two-mode squeezed vacuum (TMSV) states are optimal for sensing loss channels and outperform coherent states for estimating the loss parameter in the bosonic channels, however they can't beat the shot noise limit [Adesso et al., 2009, Alipour et al., 2014, Brambilla et al., 2008, Crowley et al., 2014, Hayat et al., 1999, Heidmann et al., 1987, Ioannou et al., 2021, Jakeman and Rarity, 1986, Losero et al., 2018, Monras and Paris, 2007, Nair, 2018, Atkinson et al., 2021]. For a depolarization channel it is shown that Heisenberg limit scaling is not possible, however using correlated probes and ancilla-assisted schemes increases the estimation accuracy [Sasaki et al., 2002, Collins and Stephens, 2015, Frey et al., 2011, Hotta et al., 2005]. In general, it was argued that no parameter which is encoded on the density matrix by a non-unitary operator or a convex combination of unitary operators can be estimated beyond the shot-noise limit [Ji et al., 2008]. However, later research revealed that controlled and error-corrected metrology and environmental monitoring can be utilized to restore the Heisenberg limit for certain problems [Kessler et al., 2014, Zhou et al., 2018, Albarelli et al., 2018, Tratzmiller et al., 2020]. Recently it was demonstrated that using an entangled photonic source, one can non-destructively probe single-layer cell cultures and differentiate between different optical elements in the setup with a fewer number of projective measurements, [Zhang et al., 2024, Besaga et al., 2023]. However, quantum advantage in terms of metrology is not studied in detail these works. It has been shown theoretically and experimentally that using entangled photons one can achieve a higher precision in ellipsometric measurements [Abouraddy et al., 2002, Toussaint et al., 2004]. Additionally, ghost polarimetry using polarization entangled photons and utilizing correlations between the Stokes operators in the reference and sample beams have gained attraction in recent years because of increased sensitivity in parameter estimation, specifically for the cases in which having a few number of photons is advantageous in order not to perturb the material that is being probed [Hannonen et al., 2020, Magnitskiy et al., 2020, Magnitskiy et al., 2022, Restuccia et al., 2022a, Magnitskiy et al., 2021].

Within the framework of our quantum polarimetry approach, we endeavor to harness the unique nonlocal attributes inherent to entangled photons. Illustrated in Fig. 3.1, our approach employs two separate pathways: a channel containing the sample (s) and a reference channel (r), with each accommodating one photon and the photons in the two channels being entangled. By capitalizing on the nonlocal correlations between these photons, we aim to discern subtle polarization changes with enhanced precision. This nonlocal methodology has the potential to mitigate local noise and disturbances that traditionally challenge single-channel polarimetry methods. Through comprehensive theoretical analysis, we examine the viability of the nonlocal approach, particularly by evaluating the QFI, in comparison to the single-channel approach. Hereby, our work contributes to the understanding of fundamental nonlocal quantum phenomena in metrology and proposes a practical avenue for utilizing nonlocal quantum states in polarimetry. This avenue could potentially impact high-sensitivity measurements across scientific disciplines.

3.2 Preliminaries: Local and Nonlocal Polarimetry

We consider an entangled pair of photons, signal and idler, generated by spontaneous parametric down conversion (SPDC). They are prepared in a Bell-type entangled state in the canonical polarization basis. We assume the initial state can be ideally

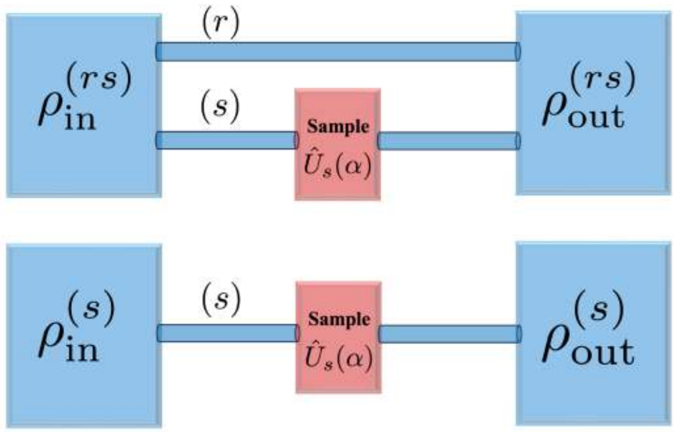

Figure 3.1: ((Top Panel) Nonlocal Quantum Polarimetry Using Entangled Photons. In this setup, a pair of photons initially prepared in a polarization-entangled state $\rho_{\text{in}}^{(rs)}$ is directed through two distinct spatial channels. One of these paths incorporates a sample denoted as (s), while the other path serves as the reference denoted as (r). The sample channel can induce changes in the polarization state of the photon, a phenomenon described by a single-parameter operation $\hat{U}_s(\alpha)$. On the contrary, the (r) channel applies an identity operation, $\hat{I}_r$, to the photon it contains. By employing quantum state tomography (QST) and conducting measurements in various polarization bases, the resulting output state $\rho_{\text{out}}^{(rs)}$ is reconstructed. (Bottom Panel) Local Quantum Polarimetry Using Single Photons. This scenario involves a single photon that is prepared in the reduced state of the two-photon entangled state, specifically $\rho_{\text{in}}^{(s)} = \text{Tr}_r(\rho_{\text{in}}^{(rs)})$. Subsequently, this photon traverses the sample channel. Employing QST allows for the reconstruction of the output state.

prepared as a pure state such that

$$|\psi_{\text{in}}\rangle = \frac{1}{\sqrt{2}}(|HV\rangle + |VH\rangle), \tag{3.1}$$

where H and V refers to horizontal and vertical polarizations, respectively. For the sake of brevity, we adopt a convenient notation $|AB\rangle = |A\rangle_r \otimes |B\rangle_s$ with $A, B \in \{H, V\}$ such that the first letter corresponds to the photon's state in the reference channel, while the second letter pertains to the sample channel's photon state.

A more explicit connection to the Bell state can be established by delving further into the polarization states. These states can be effectively expressed in terms of Fock number states, wherein the quantities n_H and n_V denote the counts of horizontally (H) and vertically (V) polarized photons. Specifically, $|H\rangle = |n_H = 1, n_V = 0\rangle \equiv |1_H\rangle$ and $|V\rangle = |n_H = 0, n_V = 1\rangle \equiv |1_V\rangle$. The introduction of a vacuum state encompassing both polarizations, denoted as $|\text{vac}\rangle := |0, 0\rangle \equiv |0\rangle$, facilitates the introduction of creation and annihilation operators corresponding to H and V polarized photons. This can be mathematically articulated as follows:

$$|n_k\rangle = \frac{(\hat{a}_k^\dagger)^{n_k}}{\sqrt{n_k!}} |0\rangle\,, \tag{3.2}$$

where $k = H, V$. The translation of polarization mode number states into spin states $|S, S_z\rangle$ is achieved through the utilization of the total spin, defined as $S = (n_H + n_V)/2$, and the $S_z = (n_H - n_V)/2$-component of spin (or magnetic quantum number). This translation assumes that the z-axis is chosen as the quantization axis. Consequently, the horizontal polarization state, $|H\rangle = |n_H = 1, n_V = 0\rangle = |S = 1/2, S_z = 1/2\rangle \equiv |\uparrow\rangle$, can be identified as the spin-up state of a spin-1/2 particle. Similarly, we can equate $|V\rangle$ with the spin-down state, $|\downarrow\rangle$. In light of this, Equation (3.1) can be interpreted as a Bell state, associated with the entanglement of two spin-1/2 particles; although the photons are not spin-1/2 particles. For transverse waves, away from radiation sources in the far field, we can thus use an effective spin-1/2 representation for the polarization states of a single photon.

In the context of a single photon polarization and spin-1/2 analogy, the utilization of polarization mode creation and annihilation operators as Schwinger boson representation of spin operators allows for the identification of generators corresponding to the SU(2) spin algebra. These generators serve as observables that capture the quantum polarization attributes of photons. Named after their resemblance to classical Stokes parameters, these observables are referred to as Stokes operators. In the context of canonical polarizations, they are expressed as follows:

$$\hat{S}_0 = \frac{1}{2}(\hat{a}_H^\dagger a_H + a_V^\dagger a_V), \tag{3.3}$$

$$\hat{S}_1 = \frac{1}{2}(\hat{a}_H^\dagger a_V + a_H a_V^\dagger), \tag{3.4}$$

$$\hat{S}_2 = -\frac{i}{2}(a_H^\dagger a_V - \hat{a}_V^\dagger a_H), \tag{3.5}$$

$$\hat{S}_3 = \frac{1}{2}(\hat{a}_H^\dagger a_H - a_V^\dagger a_V), \tag{3.6}$$

where $\hat{S} = (\hat{S}_1 \hat{S}_2 \hat{S}_3)^T$ constitutes the quantum Stokes vector. Notably, this vector commutes with $\hat{S}_0$, while its individual components adhere to the spin algebra: $[\hat{S}_i, \hat{S}_j] = i\epsilon_{ijk}\hat{S}_k$. Within the domain of a single photon state, the Stokes operators serve as comprehensive descriptors of the photon's density matrix, thus enabling quantum state tomography (QST) of the single photon state through measurement of these operators. Consequently, any alterations in quantum polarization attributes resulting from photon-sample interactions manifest as changes in the expectation values of the Stokes operators, denoted as $S_k = \mathrm{Tr}[\rho \hat{S}_k]$.

The Bell state arising from Eq. (3.1) embodies a spin triplet state $|S = 1, S_z = 0\rangle$, emerging from the amalgamation of two spin-1/2 entities. This insight prompts the proposal of extending the concept of single photon Stokes parameters to scenarios involving two or more photons, thereby encapsulating the polarization attributes of composite multiphoton systems. We remark that multiphoton nonlocal generalizations of Stokes parameters are different than generalized Stokes operators written for spin-1 atomic Bose Einstein condensate to describe their magnetization properties or for photons that can have longitudinal polarization components in near or intermediate radiation zones, where transverve wave approximation fails. Such local generalizations of Stokes operators uses generators of SU(3) algebra, introduced by Gell-Mann to explore strong interaction in particle physics [Griffiths, 2008]. In contradistinction to the "local" Stokes operators linked with individual photons, this "nonlocal" extension of Stokes parameters introduces a heightened level of complexity in terms of visualization and interpretation. Given the equivalence between Stokes parameter measurements and the direct determination of density matrices, multiphoton Stokes parameters can be equated with the process of quantum state tomography (QST) applied to a multiphoton density matrix [James et al., 2001]. Remarkably, the density matrix itself offers a means to quantify the degree of polarization. This is achieved by assessing the Q function across angular coordinates, integrating it across the entire angular domain, and subsequently gauging the deviation from the Q function of unpolarized photons [Luis, 2002]. Furthermore, the density matrix of a single photon can be decomposed using Stokes operators, which intriguingly coincide with the decomposition obtained via Pauli matrices. This property can be further generalized to encompass multiphoton scenarios.

N-photon generalized nonlocal Stokes operators are proposed by direct generalization of single photon Stokes operators [Goldberg et al., 2021a], which are equivalent to Pauli spin-1/2 operators $\hat{S}_i = \hat{\sigma}_i$ with $i = 0, 1, 2, 3$ to

$$\hat{S}_{i_1 \ldots i_N} = \hat{\sigma}_{i_1} \otimes \ldots \otimes \hat{\sigma}_{i_N}. \tag{3.7}$$

Here, $\hat{\sigma}_0 = \hat{I}$ is the identity operator, and we have $\mathrm{Tr}(\hat{\sigma}_i \sigma_j) = 2\delta_{ij}$. Simlar to the Pauli operator decomposition of single photon density matrix, the N-photon density matrix can be written as

$$\hat{\rho} = \frac{1}{2^N} \sum_{i_1=0}^{3} \ldots \sum_{i_N=0}^{3} S_{i_1 \ldots i_N} \hat{S}_{i_1 \ldots i_N}, \tag{3.8}$$

where $S_{i_1 \ldots i_N} = \mathrm{Tr}(\rho \hat{S}_{i_1 \ldots i_N})$ are the multiphoton nonlocal Stokes parameters.

In our case, we have $N = 2$ photons in an initially entangled state. One photon will interact with the sample in the s-channel while the other channel is empty and taken as the reference (r-channel). Accordingly, we determine the output state by evaluating the map

$$|\psi_{\text{out}}\rangle = \left(\hat{I}_r \otimes \hat{U}_s(\alpha)\right) |\psi_{\text{in}}\rangle. \tag{3.9}$$

In this formulation, we account for the scenario wherein the sample under consideration could either take the form of a linear polarizer (LP) or a quarter wave plate

(QWP), each characterized by a distinct angular parameter denoted as α. In the case of the LP, α signifies the transmission angle relative to the vertical axis within the laboratory frame. Conversely, for the QWP, α denotes the angle defining the orientation of the fast axis of the birefringent crystal concerning the vertical axis within the laboratory frame.

The effect of a QWP in the canonical polarization basis can be described by [Barnett, 2009]

$$\hat{U}_{\mathrm{QWP}}(\alpha) = \begin{bmatrix} \cos^2\alpha + i\sin^2\alpha & (i-1)\sin\alpha\cos\alpha \\ (i-1)\sin\alpha\cos\alpha & i\cos^2\alpha + \sin^2\alpha \end{bmatrix}, \tag{3.10}$$

while for an LP we have [Barnett, 2009]

$$\hat{U}_{\mathrm{LP}}(\alpha) = \begin{bmatrix} \sin^2\alpha & \sin\alpha\cos\alpha \\ \sin\alpha\cos\alpha & \cos^2\alpha \end{bmatrix}. \tag{3.11}$$

In the forthcoming section, our analysis is dedicated to the evaluation of the output state, which arises from a predetermined initial entangled state and distinct models characterizing the sample. The density matrix components of this output state are ascertained via QST. These elements, when combined in specific ways, give the nonlocal 2-photon Stokes parameters. Our objective is to examine the potential manifestation of a quantum advantage that may arise due to quantum nonlocality. More specifically, we endeavor to discern whether the adoption of this nonlocal quantum approach offers any discernible advantages over conventional local measurements, which are confined to single channels. After finding the output states, we evaluate the QFI to answer this question.

3.3 Evaluation of the output state

The determination of the output state follows a straightforward matrix product procedure. For the specific case of a linear polarizer (LP) sample, the outcome can be succinctly expressed as:

$$|\psi_{\mathrm{out}}\rangle = A(|HH\rangle + |VV\rangle) + C\,|HV\rangle + B\,|VH\rangle\,, \tag{3.12}$$

Here, the coefficients are assigned as $A = \sin\alpha\cos\alpha$, $B = \sin^2\alpha$, and $C = 1 - B = \cos^2\alpha$.

Discrepancies between the theoretical predictions and experimental outcomes for the output state can be attributed to a couple of distinct factors. Firstly, the experimental initial state possesses slight deviations from the ideal entangled state, necessitating its description through a density matrix ρ_{in}, accounting for these imperfections. Consequently, these deviations propagate to the output state, warranting a depiction as the density matrix ρ_{out}. Secondly, real-world sample conditions diverge from the ideal LP or QWP, introducing diattenuation and depolarization influences on the photon's polarization state. These alterations can be effectively modeled through supplementary operations alongside $\hat{U}_s(\alpha)$, formalized using Mueller matrices in accordance with the Lu-Chipman decomposition [Lu and Chipman, 1996a], extended to the quantum domain [Goldberg, 2020].

In the present analysis, the modest impact of these effects, coupled with the close proximity of theoretical and experimental outcomes, has led us to omit a detailed exploration of imperfections in the results. Nevertheless, it is noteworthy that such imperfections could potentially enrich the polarimetric analysis of an unknown sample. The constellation of parameters encompassing retardation angle, diattenuation, and depolarization characteristics can serve as distinctive signatures for materials, offering a means of characterization and classification vis-à-vis datasets from other samples.

Further comparison between the theoretical output state and experimental findings has consistently yielded nearly perfect agreement in the case of the QWP as well. An essential divergence between the LP and QWP scenarios lies in the emergence of imaginary components within the density matrix elements in the latter case.

The input state for the local, single s-channel scenario is given by the reduced state

$$\rho_{\text{in}}^{(s)} = \frac{1}{2}(|H\rangle_s \langle H|_s + |V\rangle_s \langle V|_s), \tag{3.13}$$

which is maximally mixed, unpolarized, state with $S_0 = 1/2, S_1 = S_2 = S_3 = 0$.

After the LP, the output state becomes

$$\rho_{\text{out}}^{(s)} = B\,|H\rangle_s\,\langle H|_s + C\,|V\rangle_s\,\langle V|_s + A(|H\rangle_s\,\langle V|_s + |V\rangle_s\,\langle H|_s). \tag{3.14}$$

The Stokes parameters of the output state are given by $S_0 = 1/2, S_1 = A, S_2 = 0, S_3 = B - 1/2$, which shows that LP can polarize the initially unbpolarized photon.

Following a similar procedure we find the output of the two photon entangled state after being acted upon by QWP to be

$$|\psi_{\text{out}}\rangle = \frac{(i-1)A}{\sqrt{2}}(|HH\rangle + |VV\rangle) + \frac{iC + B}{\sqrt{2}}\,|HV\rangle + \frac{C + iB}{\sqrt{2}}\,|VH\rangle\,. \tag{3.15}$$

For the case of local polarimetry, the state at the output of QWP becomes

$$\rho_{\text{out}}^{(s)} = \frac{1}{2}(|H\rangle_s\,\langle H|_s + |V\rangle_s\,\langle V|_s). \tag{3.16}$$

It is evident that the utilization of both single-channel local and two-channel non-local quantum polarimetry, encompassing the examination of local and nonlocal Stokes parameters, or equivalently, the elements of local or nonlocal states, furnishes a viable means to ascertain the unknown parameters associated with the sample, represented in this context by the angle α. However, which strategy proves more precise in this pursuit? In order to address this question rigorously, we proceed to evaluate the QFI in the subsequent section.

3.4 Comparison of the precision

QFI quantifies the maximum achievable information about a parameter using a parameterized density matrix. The Quantum Cramer-Rao bound (QCRB) establishes a lower bound on the variance of any unbiased estimator $\hat{\alpha}$ of the parameter α such that for a single repetition of the measurement of θ, the variance of the estimator is lower bounded by the reciprocal of the QFI [Sidhu and Kok, 2020b]. The mathematical expression of the QCRB for an unbiased estimator $\hat{\alpha}$ is

$$\text{Var}(\alpha) \geq \frac{1}{mF_Q}, \tag{3.17}$$

in which m is the number of observations and F_Q is the QFI. For a pure state QFI can be expressed as [Sidhu and Kok, 2020b]

$$F_Q = 4[\langle \partial_\alpha \psi | \partial_\alpha \psi \rangle - |\langle \psi | \partial_\alpha \psi \rangle|^2]. \tag{3.18}$$

For a mixed state the QFI becomes [Sidhu and Kok, 2020b]

$$\mathcal{F} = \sum_i \frac{(\partial_\alpha \lambda_i)^2}{\lambda_i} + 2 \sum_{i \neq j} \frac{(\lambda_i - \lambda_j)^2}{\lambda_i + \lambda_j} |\langle e_i | \partial_\alpha e_j \rangle|^2. \tag{3.19}$$

We aim to find the estimation precision of the parameter α using QFI for both local and non-local scenarios. For the case of the LP, the output state for the single channel has the matrix form

$$\rho_{\text{out}} = \begin{bmatrix} B & A \\ A & 1-B \end{bmatrix}, \tag{3.20}$$

whose eigenvalues are $\lambda_0 = 0$ and $\lambda_1 = 1$. The corresponding eigenvectors can be written as $e_0 = (\cos\alpha - \sin\alpha)^T$ and $e_1 = (\sin\alpha \cos\alpha)^T$. For the case of an entangled initial state and two-channel nonlocal polarimetry, the output state is a pure state as given in Eq. (3.12). Substituting them into the quantum Fisher information formula gives

$$\begin{aligned} \mathcal{F}^{\text{L}}_{\text{LP}} &= 4, \\ \mathcal{F}^{\text{NL}}_{\text{LP}} &= 8. \end{aligned} \tag{3.21}$$

Both expressions are independent of α. Hence we find $\mathcal{F}^{\text{NL}}_{\text{LP}} = 2\mathcal{F}^{\text{L}}_{\text{LP}}$. Similar calculations for local metrology for the case of QWP gives

$$\begin{aligned} \mathcal{F}^{\text{L}}_{\text{QWP}} &= 0, \\ \mathcal{F}^{\text{NL}}_{\text{QWP}} &= 8. \end{aligned} \tag{3.22}$$

It is clear that the output state for the local case is parameter independent as given in Eq. (3.16) and we can't use it to give any estimate of α. Therefore the non-local approach is far superior than the local one for the case of QWP. It is instructive to check the QFI for equally weighted superposition states of vertical and horizontal polarization modes for the two photon polarimetry scheme. Using such a state for two-photon LP and QWP settings we get

$$\begin{aligned} \mathcal{F}^{\mathrm{SP}}_{\mathrm{LP}} &= 4, \\ \mathcal{F}^{\mathrm{SP}}_{\mathrm{QWP}} &= 8 - 4\cos^2(2\alpha). \end{aligned} \tag{3.23}$$

From Eq. (3.23) we see that for local polarimetry, the QFI for the superposition state $(|H\rangle + |V\rangle)/\sqrt{2}$ for the case of LP is equivalent to that of completely mixed state given in Eq. (3.21). For the case of QWP, upon using the superposition state as a probe, one gains an overall increase in efficiency compared with the completely mixed probe states. However, we see that the QFI becomes dependent on α in this case and it takes values between 4 and 8. We see that polarimetry for QWP and LP with entangled photons not only yields a larger result for QFI, but entanglement is also necessary to gain information independent of the specific choice of α.

3.5 Quantum State Tomography

QST is the process of reconstructing a quantum state from the measurement outcomes of experiments on an ensemble of identical quantum states [James et al., 2001, Paris and Řeháček, 2004, D'Ariano et al., 2003, Altepeter et al., 2005]. Considering that the measurements are represented by the positive operator-valued measurements (POVM) $\hat{\Pi}_i = |\psi_i\rangle\langle\psi_i|$, we know that measuring $\hat{\Pi}_i$ will produce an outcome with label i whose probability is calculated using Born rule

$$p_i = \mathrm{Tr}[\hat{\rho}\hat{\Pi}_i]. \tag{3.24}$$

Experimentally, one measures the POVM, $\mathcal{N}$ times using $\mathcal{N}$ copies of the unknown state $\hat{\rho}$. The average number of coincidence counts will be given by

$$n_i = \mathcal{N}\mathrm{Tr}[\hat{\Pi}_i\hat{\rho}]. \tag{3.25}$$

Therefore in QST one approximates p_i by $f_i = n_i/\mathcal{N}$. For $\mathcal{N} \to \infty$ the probability for these measurement outcomes is given by $p_i = n_i/\mathcal{N}$. Assuming that the Hilbert space is finite dimensional and taking $\hat{E}_i$ as a set of orthonormal Hermitian basis of traceless operators, we can express the density matrix as:

$$\hat{\rho} = \frac{\hat{I}}{d} + \sum_{i=1}^{d^2-1} r_i \hat{E}_i. \tag{3.26}$$

Here, r_i are real numbers and d is the dimensionality of the Hilbert space. Substituting Eq. (3.27) in Eq. (3.24) and approximating the probabilities with frequencies we get.

$$f_i \approx \frac{\mathrm{Tr}[\hat{\Pi}_i]}{d} + \sum_{i=1}^{d^2-1} r_i \mathrm{Tr}[\hat{\Pi}_i \hat{E}_i]. \tag{3.27}$$

Assuming that $\tilde{f}_i = f_i - \mathrm{Tr}[\hat{\Pi}_i]d$ and $\tilde{\Pi}_{i,j} = \mathrm{Tr}[\hat{\Pi}_i \hat{E}_i]$ we can write this equation in a matrix form as $\tilde{\boldsymbol{f}} \approx \tilde{\boldsymbol{\Pi}}\boldsymbol{r}$. The goal is to find the vector of expansion coefficients $\boldsymbol{r}$ using $\tilde{\boldsymbol{f}}$ which is only possible if the matrix $\tilde{\boldsymbol{\Pi}}$ is invertible. This condition is satisfied for informationally complete sets of POVMs that span the space of density matrices acting on the Hilbert space.

In what follows in this section, we will present a basic review of optical polarization QST for a single and two qubit systems. In polarization QST the experimental data is a collection of coincidence counts of the photodetectors implementing a collection of projective measurements. In polarization measurements, the usual states used for projective measurements are horizontal ($|H\rangle$) and vertical ($|V\rangle$) linear polarized states, right ($|R\rangle$) and left ($|L\rangle$) circular states and diagonal ($|D\rangle$) and anti-diagonal ($|A\rangle$) polarization states. Hence, the goal is to estimate the state $\hat{\rho}$ based on the information of the coincidence counts n_i for each projective measurement $|\psi_i\rangle \langle\psi_i|$. For a single qubit Eq. (3.8) can be written as

$$\hat{\rho} = \frac{1}{2} \sum_{i=0}^{3} \frac{S_i}{S_0} \sigma_i. \tag{3.28}$$

Writing the Stokes operators in terms of the POVMs one can find their expectation values as

$$\begin{gathered} \mathcal{N} = n_H + n_V = n_D + n_A = n_R + n_L, \\ S_1 = \frac{1}{\mathcal{N}}(n_D - n_A), \\ S_2 = \frac{1}{\mathcal{N}}(n_R - n_L), \\ S_3 = \frac{1}{\mathcal{N}}(n_H - n_V). \end{gathered} \tag{3.29}$$

Upon substituting these equations into Eq. (3.28) and assuming $S_0 = 1$ (no photon loss) one can estimate the one qubit density matrix using the coincidence numbers of the six POVMs. For two qubits Eq. (3.8) can be written as

$$\hat{\rho} = \sum_{i=1}^{16} r_i \hat{\Gamma}_i, \tag{3.30}$$

in which the basis $\hat{\Gamma}_i$ are the two-qubit Stokes operators. In Eq. (3.30) $r_i = \mathrm{Tr}[\hat{\Gamma}_i \hat{\rho}]$ are the expansion coefficients of the density matrix for their respective two-qubit Stokes operators given as a 16×1 vector. The coincidence counts and the expansion coefficients are connected via

$$n_i = \mathcal{N} \sum_{i=1}^{16} (B^{-1})_{i,j} n_j. \tag{3.31}$$

The 16×16 matrix B is defined as $B_{i,j} = \langle\psi_i| \Gamma_j |\psi_i\rangle$. It is shown that the density matrix can be expanded as

$$\hat{\rho} = \frac{1}{\mathcal{N}} \sum_{i=1}^{16} \hat{M}_i n_i, \tag{3.32}$$

in which the matrix $\hat{M}_i$ are 4×4 matrices defined via

$$\hat{M}_i = \sum_{i=1}^{16} (B^{-1})_{i,j} \Gamma_j. \tag{3.33}$$

To partially mitigate the detrimental effects of experimental systematic errors on the reconstructed density matrices, one can utilize maximum likelihood estimation (MLE). In MLE, the objective is to explore the entire space of permissible, physically valid density matrices in order to identify the one that maximizes the likelihood of yielding the observed measurement outcomes. During this optimization process, to ensure that the resulting states are physical, the density matrices are written as their normalized Cholesky decomposition

$$\hat{\rho}(\vec{t}) = \frac{\hat{T}^\dagger \hat{T}}{\mathrm{Tr}[\hat{T}^\dagger \hat{T}]}. \tag{3.34}$$

By construction, Eq. (3.34) yields a positive, Hermitian and normalized density matrix. The operator $\hat{T}$ is a triangular matrix and is parametrized as

$$\hat{T}(\vec{t}) = \begin{bmatrix} t_1 & 0 & \cdots & 0 \\ t_{2^n+1} + it_{2^n+1} & t_2 & \cdots & 0 \\ \cdots & \cdots & \cdots & 0 \\ t_{4^n-1} + it_{4^n} & t_{4^n-3} + it_{4^n-2} & t_{4^n-5} + it_{4^n-4} & t_{2^n}. \end{bmatrix} \tag{3.35}$$

The distribution of coincidence numbers is of Poisson type but for large coincidence counts, due to the central limit theorem, one can approximate this using a normal distribution. For a normally distributed coincidence counts, the likelihood that the parametrized density matrix Eq. (3.34) produces the measured counts is

$$P(\vec{n}, \vec{t}) = \frac{1}{N_{norm}} \prod_i \exp\left[\frac{(\mathcal{N}\mathrm{Tr}[\hat{\Pi}_i \hat{\rho}(\vec{t})] - n_i)^2}{2\mathcal{N}\mathrm{Tr}[\hat{\Pi}_i \hat{\rho}(\vec{t})]}\right]. \tag{3.36}$$

The task is to maximize this likelihood function by finding the optimal values for the parameters in $\vec{t}$. To simplify the procedure, one can minimize the negative of the log-likelihood function instead of maximizing the likelihood. Doing so, the function that MLE minimizes becomes

$$\mathcal{L}(\vec{n}, \vec{t}) = \sum_i \exp\left[-\frac{(\mathcal{N}\mathrm{Tr}[\hat{\Pi}_i \hat{\rho}(\vec{t})] - n_i)^2}{2\mathcal{N}\mathrm{Tr}[\hat{\Pi}_i \hat{\rho}(\vec{t})]}\right]. \tag{3.37}$$

Hence, through the process of MLE quantum state tomography, due to Eq. (3.34) one is guaranteed to get a valid density matrix which minimizes the penalty function Eq. (3.37) and therefore is most likely to produce the experimentally measured coincidence counts.

3.6 Experimental Implementation

The experimental setup that we used within the reported studies is outlined in Fig. 3.2. A polarization Mach-Zehnder interferometer with two periodically-poled KTP ($KTiOPO_4$) crystals serves as the source of polarization-entangled photon pairs [Horn and Jennewein, 2019]. The wavelength-degenerate photons at 810 nm are produced through spontaneous parametric down-conversion (SPDC) in type-II phase matching configuration. At the exit of the interferometer the photons are split into two spatially

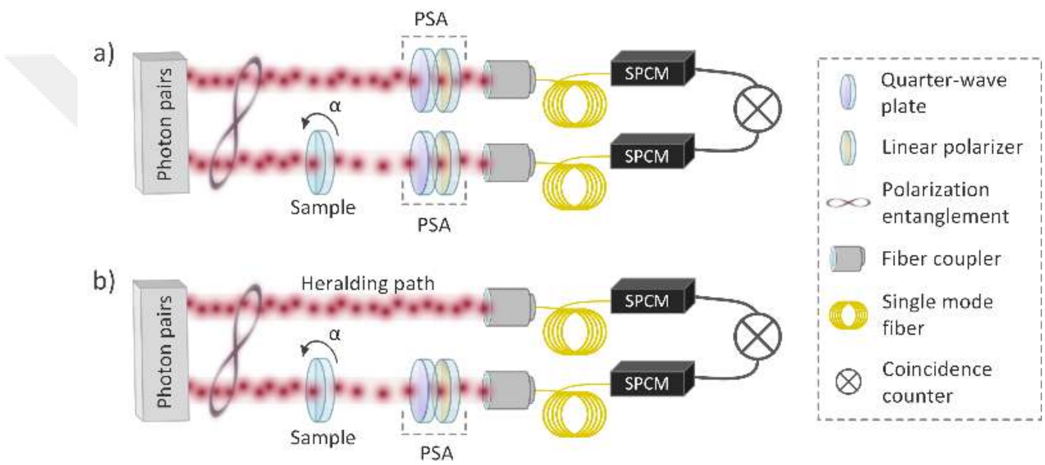

Figure 3.2: Optical arrangement used in the experiments. (a) Nonlocal quantum polarimetry using a pair of polarization-entangled photons (Bell state in the form of$1/\sqrt{2}(|HV\rangle + |VH\rangle)$. (b) Local quantum polarimetry. The partner photon from the entangled pair acts as a heralding one. PSA: polarization state analyzer; α: angle of sample's principal optical axis orientation (fast axis for quarter-wave plate, transmission axis for linear polarizer); SPCM: single photon counting module.

separated channels. In one of the channels we employ a combination of quarter- and half-wave plates to ensure the Bell state in the form of $\frac{1}{\sqrt{2}}(|HV\rangle + |VH\rangle)$. The preparation of the entangled photon pairs is not detailed in the figure.

The performance of the source is evaluated via QST [James et al., 2001] using one detector per channel. For projective polarization detection we introduce rotating QWP and LP in both channels and fiber-coupled single photon counting modules. By using a time tagging device we acquire the coincidence events which are then used for reconstructing the density matrix by the maximum likelihood method [Paris and Řeháček, 2004]. The experimentally achieved state reaches a concurrence of 0.94 and a fidelity with the designed Bell state of 0.96.

During the sample evaluation, a QWP or a LP is introduced into the sample channel at several orientations. The angles between the optical axis of the sample (fast axis of the QWP, transmission axis of the LP) and the vertical axis in the laboratory frame were 0, 45°, 90°, and a randomly generated angled of 37°. Following the concept from Fig. 3.1 we performed measurements using the one- and two-channel configurations. For the latter, the same procedure as for source performance evaluation was used, but with a sample influencing the polarization of one of the photons from the pair.

For the one-photon measurement we utilized the same source but polarization sensing was performed only in the sample channel. Taking into account that the number of coincidence events is much less than the single photon counts, the coincidence based measurement in two-channel configuration can not be directly compared with the single-photon experiment by simply using the same integration time. To overcome this issue we performed heralded single-channel measurements. For this, the QWP and LP in the reference arm were removed and the projective measurements were performed only in the sample channel. Also here, we counted the coincidence events between two channels, now the reference photon acting as a heralding one, and used these counts for one-photon density matrix reconstruction [Paris and Řeháček, 2004]. Hereby we kept the number of photons contributing to the useful signal on the same level as in the two-channel measurement mode.

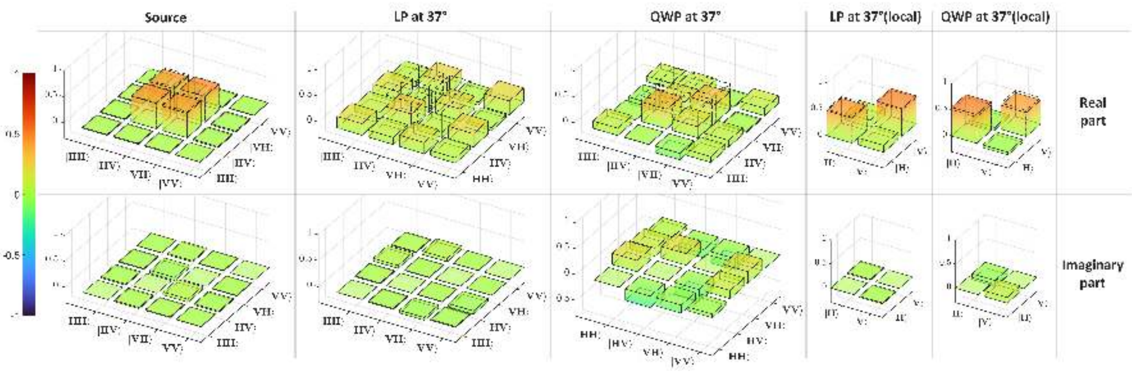

Figure 3.3: Representative density matrices of the probe state ("source"); two-photon state after the signal photon interacted with a linear polarizer (LP) and a quarter wave plate (QWP) oriented with their optical axis at 37° (averaged over 10 experimental runs); signal photon state after interaction with LP and QWP oriented at 37° (averaged over 10 experimental runs).

The representative examples of the density matrix of the two-photon state entering the experimental arrangement, and outcomes from the two- and one-channel measurements are shown in Fig. 3.3. For both modes of the experiments we measured the density matrix of the quantum state altered by the sample, each repeated 10 times.

3.7 Theoretical Analysis of the Data

In order to compare the experimental results given in Fig. 3.3 with the theoretical predictions, in Fig. 3.4 we calculated the expected output density matrices for each polarimetry task, which are shown in Fig. 3.4. We have used the open source package QuTiP for our calculations [Johansson et al., 2013].

Upon comparing Fig. 3.3 and Fig. 3.4 we see that although they are qualitatively very close, the measured and calculated density matrix differ slightly. This is expected due to several sources of error and noise including state preparation error, ambient dark noise, imperfections in the optical elements, fluctuations of the photon

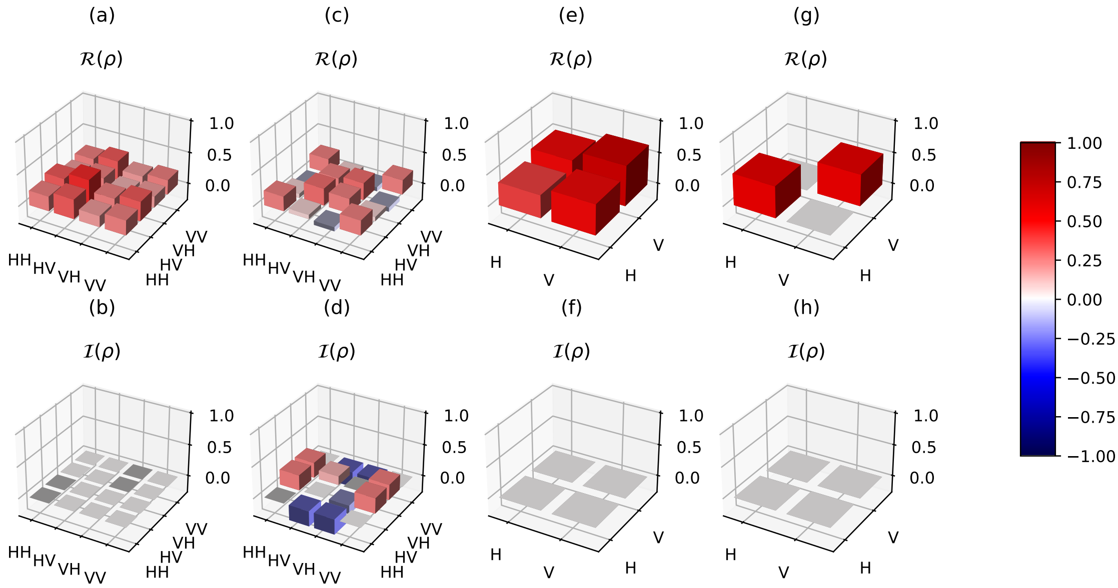

Figure 3.4: Theoretical results for the density matrix after each experiment shown as a histogram. Real (a) and imaginary (b) components of the density matrix for the non-local scheme with LP. Real (c) and imaginary (d) components of the density matrix for the non-local scheme with QWP. Real (e) and imaginary (f) components of the density matrix for the local scheme with LP. Real (g) and imaginary (h) components of the density matrix for the local scheme with QWP. Both LP and QWP are oriented at 37°.

source and errors in photon counting and post-processing. The errors are more pronounced for the local and non-local polarimetry experiments on LP. To gain a better understanding of the errors with respect to the theoretical predictions, in Fig. 3.5 the fidelity of the experimental density matrices with their theoretical counterparts are given. Here we clearly see that the aforementioned experimental data are more distant to their theoretical counterparts. The goal in these experiments is to predict the value of α which we set to be equal to 37 degrees. We consider two different estimators to find the rotation angle of the optical devices.

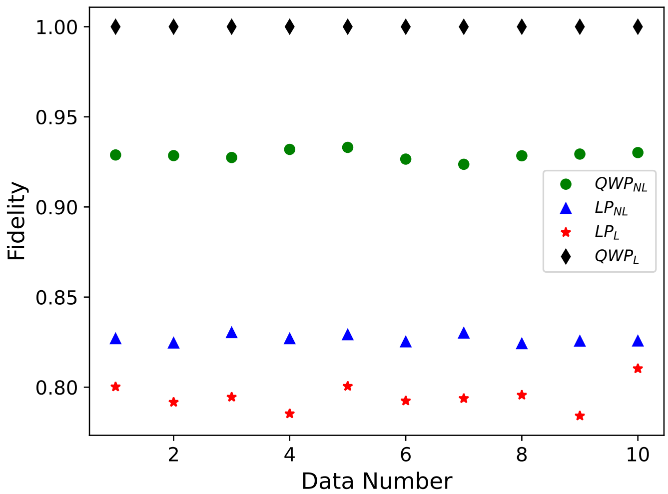

Figure 3.5: Fidelity between the tomographically reconstructed experimental density matrix and the theoretical density matrix for each experiment. Black diamonds, green circles, blue triangles and red stars represent the results for local QWP, non-local QWP, non-local LP and local LP respectively.

From Eq. (3.12), Eq. (3.14) and Eq. (3.15) we can use the following expressions as estimators for α.

$$\begin{aligned} \hat{\alpha}_1^{\mathrm{LP_{NL}}} &= \arctan\left(\sqrt{\frac{\rho_{11}}{\rho_{22}}}\right), \\ \hat{\alpha}_1^{\mathrm{QWP_{NL}}} &= \arccos\left(\sqrt{2(\rho_{33}-\rho_{44})}\right), \\ \hat{\alpha}_1^{\mathrm{LP_{L}}} &= \arctan\left(\sqrt{\frac{\rho_{11}}{\rho_{22}}}\right). \end{aligned} \tag{3.38}$$

We can also define another estimator based on the value of angle that maximizes the fidelity between the experimental density matrix and the density matrix obtained by transforming the input state (entangled state for the non-local and maximally mixed state for the local) by that angle, using the corresponding transformation matrix related to the experiment

$$\hat{\alpha}_2 = \{\alpha^* \in [0, \pi/2] : \forall \alpha \in [0, \pi/2], \text{fidelity}(\rho_{\text{exp}}, \varepsilon_{\alpha^*}(\rho_{\text{in}})) \geq \text{fidelity}(\rho_{\text{exp}}, \varepsilon_{\alpha}(\rho_{\text{in}}))\}. \tag{3.39}$$

Here, ε_α represents a transformation operator using QWP or LP acting on the initial state and giving the final state and parameterized by α. So all the estimators given in Eq. (3.38) have their counterparts in Eq. (3.39). In Fig. 3.6 the estimated angles given by these two sets of estimators are given.

Although theoretical predictions without considering any source of noise yield the correct result for the value of the angle, it is evident that the average value of the estimated angles for all polarimetric procedures and both estimators, does not equal to the real value of $\alpha = 37$. Therefore, the results suggest that the angles estimated using experimental data contain statistical bias, reports for which are available in the literature [Riberi et al., 2023, Yamamoto et al., 2022]. From Fig. 3.6(a) we see that indeed non-local polarimetry for LP using entangled photons gives a better estimate of α as compared to the local case. Also, we see that the QWP experiment has a far larger error compared with both of the LP experiments. However, even this is a considerable improvement compared to the local QWP experiment because in that case QFI is zero and no angle can be estimated. In Fig. 3.6(b) we see that applying the estimator defined by the fidelity maximization procedure, more accurate estimates for the values of α are obtained. In this estimator, unlike the one given by Eq. (3.38), the information from all of the elements of the density matrices are used and therefore generally it is expected that it will yield a better estimate. However, the effect of the noise on the estimation of the angle is highly non-trivial and comparing Fig. 3.6(a) and Fig. 3.6(b) we can see that although the accuracy of non-local polarimetry is higher than local case for the estimator $\hat{\alpha}_1$, the converse is

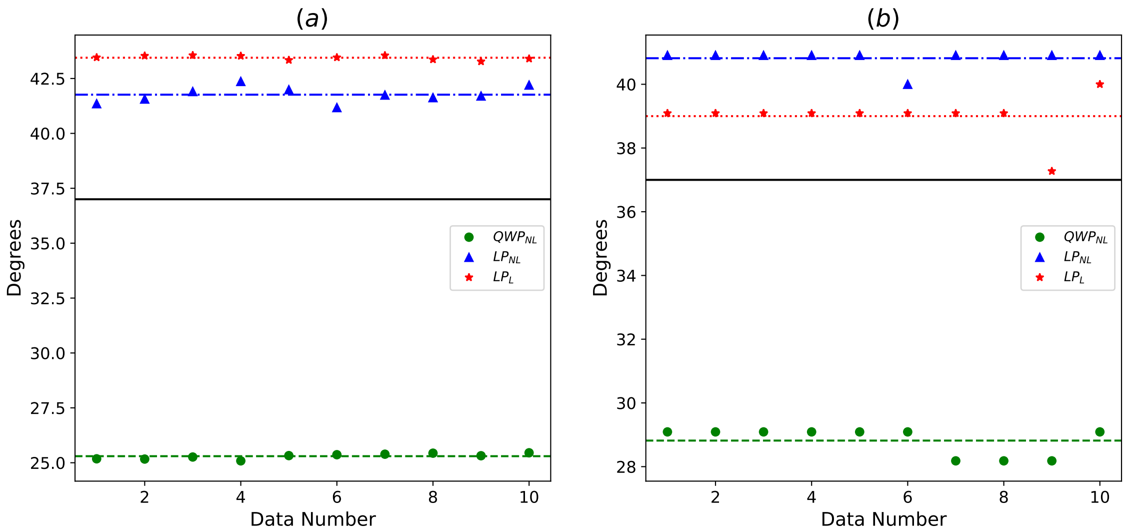

Figure 3.6: Estimated angle α for each experiment using two different estimators. (a) Estimated angles with $\hat{\alpha}_1$ using the trigonometric relations between the elements of the density matrices given in Eq. (3.38). The red stars and red dotted line are the angles estimated for local LP experiment and their average. The blue triangles and blue dot dashed line are the angles estimated for non-local LP experiment and their average. The green circles and green dashed line are the angles estimated for non-local QWP experiment and their averages. (b) Estimated angles with $\hat{\alpha}_2$ using the fidelity maximization procedure given in Eq. (3.39). The description of the data points and their averages are similar to part (a). The solid black line is the actual value of the angle at 37 degrees. The variances for the estimated angles in (a) are $\mathrm{Var}(\hat{\alpha}_1^{\mathrm{LP_{NL}}}) = 0.1202$, $\mathrm{Var}(\hat{\alpha}_1^{\mathrm{QWP_{NL}}}) = 0.0135$ and $\mathrm{Var}(\hat{\alpha}_1^{\mathrm{LP_L}}) = 0.0087$. The variances for the estimated angles in (b) are $\mathrm{Var}(\hat{\alpha}_2^{\mathrm{LP_{NL}}}) = 0.0744$, $\mathrm{Var}(\hat{\alpha}_2^{\mathrm{QWP_{NL}}}) = 0.1735$ and $\mathrm{Var}(\hat{\alpha}_2^{\mathrm{LP_L}}) = 0.4049$.

true for $\hat{\alpha}_2$. Additionally it must be stated that the estimate given in Eq. (3.38) has one advantage over Eq. (3.39) and that is the fact that one only needs two density matrix elements to come up with an angle estimate and full QST is not required.

Our results demonstrate that although one can use entanglement to enhance parameter estimation sensitivity, it is also important to consider the effect of realistic metrological experiments with various possible noise contributions on the accuracy of the estimated parameters. It is also important to design estimators which are more robust to loss of accuracy due to noise. For example, it is shown in Fig. 3.6 that $\hat{\alpha}_1$ is more susceptible to the noise-induced bias compared with $\hat{\alpha}_2$. It is worth mentioning that for biased estimators the QCRB becomes [Sidhu and Kok, 2020b]

$$\mathrm{Var}(\alpha) \geq \frac{(1+\partial_\alpha b)^2}{mF_Q}, \tag{3.40}$$

in which b is the bias of the estimator. Our results show that, taking into account the various sources of experimental noise and uncertainty, estimated values for the angle will contain bias. To investigate the validity of this assertion and get more insight, in the next section we will perform QST on a set of numerically generated data which takes into account several sources of noise.

3.8 Theoretical Model of the Experimental noise

However small it may be, no experiment is immune to noise. It is important to take into account the effects of noise on the results of the experiment, quantify it if it is possible, and take measures to mitigate such effects. In our experiment several sources of error exist that can potentially distort the data. In our theoretical analysis of the effect of noise we only consider four sources of noise, namely state preparation noise, dark counts, misalignment of measurement bases and Poisson noise in photon counting. Other possible sources of error such as imperfections of the photodetectors and other optical elements are neglected. We model the state preparation noise as

$$\hat{\rho}_{in} = q_1\hat{\rho} + (1-q_1)\hat{\rho}_r, \tag{3.41}$$

in which $\hat{\rho}$ is the desired noiseless input state, $\hat{\rho}_r$ is a an average of a number of random density matrices and $q_1 \in [0, 1]$ is a real number quantifying the amount of preparation noise. In addition to the optical signal, the background noise can also trigger the photodetectors and induce dark counts. To model this effect, we assume that the quantum state of the background noise is given by a maximally mixed state and that it also contributes to the input of the photodetectors [Czerwinski, 2022, Czerwinski, 2021].

$$\hat{\rho}' = q_2 \hat{\rho}_{out} + (1 - q_2) \frac{\hat{I}_d}{d}. \tag{3.42}$$

Here, $q_2 \in [0, 1]$ is a real number quantifying the amount of dark counts and $\hat{I}_d$ is a $d \times d$ identity matrix. $\hat{\rho}_{out}$ is the density matrix at the output of LP or QWP considering the fact that the input state is $\hat{\rho}_{in}$. During the experiments, the measurement process is also subject to noise. In our calculations we model this noise by random rotations of the projection operators. The rotation operator is given by [Lohani et al., 2020, Danaci et al., 2021, Czerwinski, 2022, Czerwinski, 2021].

$$\hat{U}(\omega_1, \omega_2, \omega_3) = \begin{bmatrix} e^{i\omega_1/2}\cos(\omega_3) & -ie^{i\omega_2/2}\sin(\omega_3) \\ -ie^{-i\omega_2/2}\sin(\omega_3) & e^{-i\omega_1/2}\cos(\omega_3), \end{bmatrix} \tag{3.43}$$

in which ω_1, ω_2, ω_3 are normally distributed parameters with zero mean and standard deviation σ. In this framework, σ determines the amount of noise due to random rotations and misalignment in the measurement bases. The rotated projection operator becomes

$$\hat{\Pi}_i' = (\hat{I} \otimes \hat{U}) \hat{\Pi}_i (\hat{I} \otimes \hat{U}^\dagger). \tag{3.44}$$

The coincidence counts, including the sources of noise, is given by

$$n_i' = \mathcal{N}_i \mathrm{Tr}[\hat{\Pi}_i' \hat{\rho}'], \tag{3.45}$$

in which $\mathcal{N}_i \in \mathrm{Pois}(\mathcal{N})$ is randomly generated using the Poisson distribution with the mean value of $\mathcal{N}$. Using Eq. (3.45) we include the effect of Poisson noise in our calculations for photon counting.

Our goal is to show that the mentioned experimental noise models can induce bias in our parameter estimation problem. We don't intend to optimize the parameters of our noise model to quantify the experimental errors more accurately. For our calculations we take $\sigma = \pi/720, \mathcal{N} = 5000$. The random density matrix in Eq. (3.41) is averaged out of 20 random density matrices. Also, to make presentation of our results simpler, we take $q_1 = q_2 = q$. The theoretical results for noisy QST for our chosen set of parameters is given in Fig. 3.7. Comparing Fig. 3.7(a) and Fig. 3.7(b) it is clear that compared to $\hat{\alpha}_1$ using $\hat{\alpha}_2$ as an estimator will result in a smaller bias. Our calculations show that for $\hat{\alpha}_1$, although there are fluctuations due to Poisson noise, the bias increases linearly with parameter q as shown in Fig. 3.7(a). For our selected set of parameters we see that in Fig. 3.7(a) that in case of using $\hat{\alpha}_1$ as the estimator $\hat{\alpha}_1^{\mathrm{LP_{NL}}}$ results in the smallest bias. However, using the estimator $\hat{\alpha}_2$, as shown in Fig. 3.7(b), $\hat{\alpha}_2^{\mathrm{LP_{L}}}$ yields the smallest value for bias. Our results clearly show that including sources of error in our calculations will induce bias in the estimated angles. Therefore, to fully utilize the metrological quantum advantage one can either try to reduce the effect of noise on the experimental results, or design estimators that are less susceptible to noise.

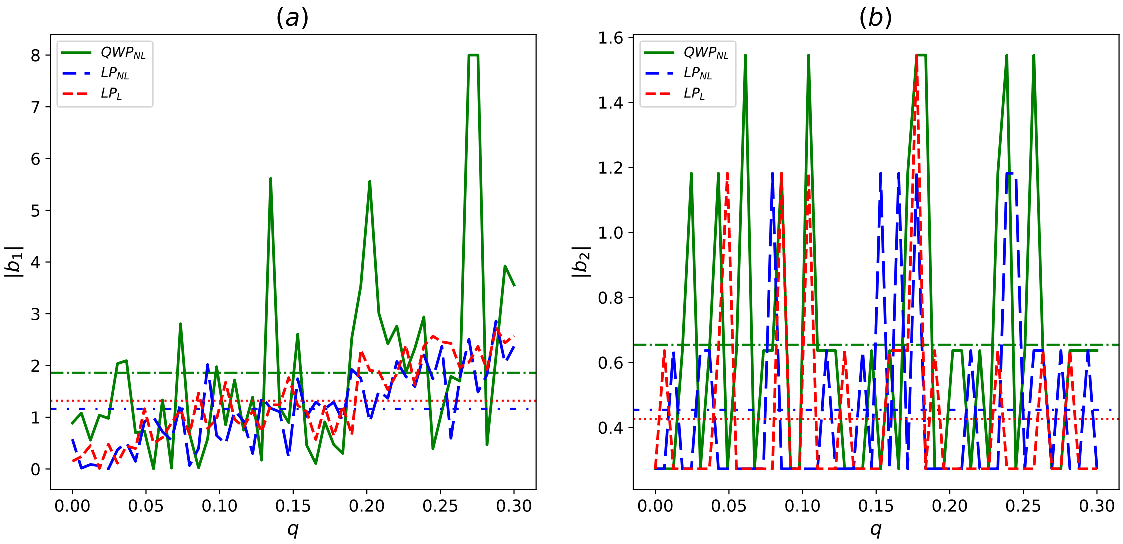

Figure 3.7: The magnitude of bias for the estimator (a) $\hat{\alpha}_1$ and $\hat{\alpha}_2$ (b) . In both (a) and (b) the solid green, long-dashed blue and the dashed red lines are $\hat{\alpha}_i^{\mathrm{QWP_{NL}}}$, $\hat{\alpha}_i^{\mathrm{LP_{NL}}}$ and $\hat{\alpha}_i^{\mathrm{LP_L}}$ respectively. The expected values for magnitude of bias are shown by the dash-dotted green line for $\hat{\alpha}_i^{\mathrm{QWP_{NL}}}$, loosely dash-dotted blue line for $\hat{\alpha}_i^{\mathrm{LP_{NL}}}$, and dooted red line for $\hat{\alpha}_i^{\mathrm{LP_L}}$.

Chapter 4

QUANTUM ESTIMATION OF THE STOKES VECTOR ROTATION FOR A GENERAL POLARIMETRIC TRANSFORMATION

4.1 Introduction: Quantum Polarimetry of Biological Tissues

Polarization is a property of a propagating electromagnetic wave which quantifies the direction of the oscillations of the electric field. This property of the electromagnetic waves is exploited in a diverse set of technological applications in materials science [Nesse and Nesse, 2004, Kaminsky et al., 2004, Theeten and Aspnes, 1981, Losurdo et al., 2009, Andreou and Kalayjian, 2002], astronomy [Tinbergen, 1996, Snik and Keller, 2013], medical sciences [He et al., 2021b, Vitkin et al., 2015b, Ghosh and Vitkin, 2011, Ramella-Roman et al., 2020, Gramatikov, 2014], and quantum information [Kok et al., 2007]. Interaction with a medium can alter the polarization state of light. A simple framework for calculating the transformation of polarized light by different optical elements is Jones matrix calculus [Hecht, 2017]. Here, the polarized light is modeled using a 2×1 vector and the optical elements causing the polarized light to undergo linear transformations is modeled by 2×2 matrices. However, Jones calculus is only applicable for fully polarized states. A more general framework is the Mueller matrix calculus, which can be used to model partially polarized states and depolarizing transformations as well [Hecht, 2017]. In Mueller calculus the polarization states are represented by the Stokes vectors which are 4×1 vectors and optical elements are modeled using 4×4 Mueller matrices.

Optical polarimetry is a field of study and a set of techniques concerning measurement and interpretation of the polarization information. Studying the polarization of light before and after it interacts (transmission, reflection, or scattering) with a medium, one can infer several optical and geometric properties of the sample. Based on the optical properties of the material under study different polarimetry techniques might be used, such as transmission polarimetry or ellipsometry. Mueller polarimeters comprehensively measure the change of polarization state of light providing 16 elements of the Mueller matrix of a sample [Azzam, 2016]. The non-invasive nature and high precision of polarimetry makes it suitable for studying sensitive samples. Ellipsometry is widely used for many applications including measurement of the refractive index and thickness of thin films [Theeten and Aspnes, 1981]. Polarimetry techniques can also be used to measure the polarization parameters of the biological samples. For instance, the thickness of the retinal nerve fiber layer (RNFL) can be used to diagnose glaucoma [Gramatikov, 2014, Bueno, 2000, Knighton et al., 2002, Benoit et al., 2001, Huang and Knighton, 2003]. The basic principle is that, RNFL is birefringent, therefore it can be modeled by a linear retarder which rotates the Stokes vector of the incoming probe state. Estimation of this rotation angle yields an estimate of the thickness of the RNFL [Knighton et al., 2002, Benoit et al., 2001, Huang and Knighton, 2003].

With growing interest in quantum metrology, there have been attempts to utilize quantum resources for precise measurement of physical parameters. Estimation of rotation angles is also of a great interest in quantum communication for studies in alignment of the reference frames of the communicating parties[Peres and Scudo, 2001a, Peres and Scudo, 2001b, Rezazadeh et al., 2017, Bagan et al., 2001, Chiribella et al., 2004, Kolenderski and Demkowicz-Dobrzanski, 2008, Safranek et al., 2015, Koochakie et al., 2021]. Interestingly, there is a straightforward link between classical polarization optics and quantum mechanics of two level systems [Aiello et al., 2007]. Other than rotation sensing, there are also attempts to utilize quantum resources for specific polarimetric tasks [Yoon et al., 2020, Rudnicki et al., 2020, Jarzyna, 2021]. Furthermore, quantum correlations of the probe state have been utilized to enhance the measurement precision in polarimetry tasks [Hannonen et al., 2020, Magnitskiy et al., 2020, Magnitskiy et al., 2022, Restuccia et al., 2022b, Vega et al., 2021, Pedram et al., 2024b]. Goldberg et al. [Goldberg, 2020, Goldberg et al., 2021a, Goldberg, 2021, Goldberg, 2022a] have studied changes in quantum polarization and have consolidated a quantum mechanical framework for polarimetry.

Several works have been carried out investigating the ultimate sensitivity limit and possible improvement for measurement of the optical properties of samples. It is shown that the NOON states and Kings of Quantumness (anticoherent states) yield Heisenberg limit (HL) scaling for rotation sensing [Chryssomalakos and Hernández-Coronado, 2017, Bouchard et al., 2017, Kolenderski and Demkowicz-Dobrzanski, 2008, Goldberg and James, 2018, Martin et al., 2020, Goldberg et al., 2021b, Eriksson et al., 2023]. For measurement of optical losses in a bosonic channel it is shown that Fock and two-mode squeezed vacuum (TMSV) states are optimal, however their error scaling doesn't surpass the standard quantum limit (SQL) [Adesso et al., 2009, Alipour et al., 2014, Brambilla et al., 2008, Crowley et al., 2014, Hayat et al., 1999, Heidmann et al., 1987, Ioannou et al., 2021, Jakeman and Rarity, 1986, Losero et al., 2018, Monras and Paris, 2007, Nair, 2018, Atkinson et al., 2021]. Studies have shown that for sensing the depolarization parameter HL scaling is not possible. However, using correlated probes and ancilla-assisted schemes increases the estimation accuracy [Sasaki et al., 2002, Collins and Stephens, 2015, Frey et al., 2011, Hotta et al., 2005]. In general, it was argued that no parameter which is encoded on the density matrix by a non-unitary operator or a convex combination of unitary operators can be estimated beyond shot noise limit [Ji et al., 2008]. At the same time, subsequent studies demonstrated that employing controlled and error-corrected methodologies in metrology and environmental monitoring could potentially reinstate the HL in specific cases [Kessler et al., 2014, Zhou et al., 2018, Albarelli et al., 2018, Tratzmiller et al., 2020].

Based on the framework developed in [Goldberg, 2020] and inspired by the studies in vision and applications of metrology in biological systems [He et al., 2021b, Vitkin et al., 2015b, Ghosh and Vitkin, 2011, Ramella-Roman et al., 2020, Gramatikov, 2014, Bueno, 2000, Knighton et al., 2002, Benoit et al., 2001, Huang and Knighton, 2003, Taylor and Bowen, 2016, Pedram et al., 2022], we aim to assess the feasibility of using quantum polarimetry for estimation of rotation angle due to a birefringent medium, modeled by a linear retarder, in presence of diattenuation and depolarization. Studies on biological tissues have shown that, although the polar decomposition of Mueller matrix [Lu and Chipman, 1996b] in tissue polarimetry can yield reliable polarization properties in classical regime, this decomposition does not correspond to the underlying physical reality [Vitkin et al., 2015b, Ghosh et al., 2009, Gao, 2021]. Furthermore, experimental evidence suggests that optical quantum entanglement can survive while photons are being transmitted through highly scattering biological tissues [Shi et al., 2016, Huang and Zeng, 2020, Lum et al., 2021, Mamani et al., 2018]. Therefore, it is crucial to investigate the precision limits in quantum polarimetry considering non-commutativity of the elementary components of the Mueller matrix, which implies considering different composition orders of the quantum polarization channels.

This chapter is organized as follows. In Section 4.2 we introduce concepts in quantum polarimetry such as Stokes operators and their transformations due to polarization channels. In Section 4.3 we present a brief explanation on Majorana representation of quantum polarization states and quantum concepts in optical polarization and introduce Kings of Quantumness and the concept of anticoherence. In Section 4.4 the results of our calculations for QFI using NOON, Kings of Quantumness [Chryssomalakos and Hernández-Coronado, 2017, Bouchard et al., 2017, Kolenderski and Demkowicz-Dobrzanski, 2008, Goldberg and James, 2018, Martin et al., 2020, Goldberg et al., 2021b, Eriksson et al., 2023] and coherent states as probe states are given and in Section 4.5 a possible experimental implementation is discussed and finally.

4.2 Quantum Description of Polarized Light and Polarization Transformations

In a quantum optical setting, each polarization mode can be thought of as a harmonic oscillator. One can write a general pure state of light by acting the creation operators of the horizontal and vertical polarization modes on the vacuum state.

$$
\begin{aligned}
|\Psi\rangle &= \sum_{n_1,n_2} c_{n_1,n_2} |n_1, n_2\rangle\,, \\
|n_1, n_2\rangle &\equiv \frac{\hat{a}^{\dagger n_1} \hat{b}^{\dagger n_2}}{\sqrt{n_1! n_2!}} |0, 0\rangle\,.
\end{aligned}
\tag{4.1}
$$

We take $\hat{a}$ and $\hat{b}$ to be the annihilation operators of the horizontal and vertical polarization modes respectively. These operators satisfy the bosonic commutation relations.

$$
[\hat{a}_i, \hat{a}_j^\dagger] = \delta_{ij}, \quad [\hat{a}_i, \hat{a}_j] = [\hat{a}_i^\dagger, \hat{a}_j^\dagger] = 0, \quad \hat{a}_i \in \{\hat{a}, \hat{b}\}. \tag{4.2}
$$

Using the field operators of the horizontal and vertical polarization modes we can define the Stokes operators as

$$
\begin{aligned}
\hat{S}_0 &= \left(\hat{a}^\dagger \hat{a} + \hat{b}^\dagger \hat{b}\right)/2, \quad \hat{S}_1 = \left(\hat{a}^\dagger \hat{b} + \hat{b}^\dagger \hat{a}\right)/2, \\
\hat{S}_2 &= -\mathrm{i}\left(\hat{a}^\dagger \hat{b} - \hat{b}^\dagger \hat{a}\right)/2, \quad \hat{S}_3 = \left(\hat{a}^\dagger \hat{a} - \hat{b}^\dagger \hat{b}\right)/2.
\end{aligned}
\tag{4.3}
$$

The Stokes operators are quantum generalizations of the Stokes parameters, which are promoted to an operator status. These operators obey the following $\mathfrak{su}(2)$ algebraic relations,

$$
\begin{aligned}
\left[\hat{S}_i, \hat{S}_j\right] &= \mathrm{i} \sum_{k=1}^{3} \epsilon_{ijk} \hat{S}_k, \\
\hat{S}_1^2 + \hat{S}_2^2 + \hat{S}_3^2 &= \hat{S}_0\left(\hat{S}_0 + 1\right).
\end{aligned}
\tag{4.4}
$$

Similar to the classical case, one can use the Stokes operators to define a semiclassical degree of polarization (DOP) [Goldberg et al., 2021a]:

$$
\mathbb{P}_{sc} = \frac{|\langle \hat{\mathbf{S}} \rangle|}{\langle \hat{S}_0 \rangle} = \frac{\sqrt{\langle \hat{S}_1 \rangle^2 + \langle \hat{S}_2 \rangle^2 + \langle \hat{S}_3 \rangle^2}}{\langle \hat{S}_0 \rangle}\,. \tag{4.5}
$$

Here, $\langle \hat{S}_i \rangle = \mathrm{Tr}[\hat{\rho}\hat{S}_i]$ denotes the expectation value of the operator $\hat{S}_i$ and $\hat{\mathbf{S}}$ is the normalized Stokes vector. However, in general for quantum states, this definition for the DOP fails to capture their polarization behavior and one needs to take into account so called "hidden polarization" or higher order polarization to which higher moments of the Stokes operators contribute [Klyshko, 1992, Alodjants and Arakelian, 1999, Luis, 2002, Klimov et al., 2005, Luis, 2007b, Klimov et al., 2010, Björk et al., 2010, Luis, 2007a, Iskhakov et al., 2011, Nogueira et al., 2013, Kothe et al., 2013, Sánchez-Soto et al., 2013]. In quantum mechanics, a general transformation of an operator is described by a completely positive trace preserving (CPTP) dynamical map which is also dubbed as a quantum channel. Kraus' theorem states that any quantum channel can be described by a set of Kraus operators $\{K_l\}$ such that,

$$\hat{S}_\mu \to \sum_l \hat{K}_l^\dagger \hat{S}_\mu \hat{K}_l. \tag{4.6}$$

For the expectation values of the Stokes operators to transform according to the classical Mueller description, the following condition must be satisfied:

$$\langle S_\mu \rangle \to \sum_{\nu=0}^{3} M_{\mu\nu} \langle S_\nu \rangle. \tag{4.7}$$

For both Eq. (4.6) and Eq. (4.7) to hold, we can impose the condition that the Stokes operators should transform in the same way as the Stokes parameters [Goldberg, 2020], thus

$$\sum_l \hat{K}_l^\dagger \hat{S}_\mu \hat{K}_l = \sum_\nu M_{\mu\nu} \hat{S}_\nu. \tag{4.8}$$

It has also been shown that if the Mueller matrix is not singular, one can decompose it into a product of three elementary matrix factors with well-defined polarimetric properties, a retarder, a diattenuator, and a depolarizer [Lu and Chipman, 1996b], using the standard Lu-Chipman decomposition as

$$M = M_d M_R M_D. \tag{4.9}$$

Here, M_D, M_R and M_d are the elementary Mueller matrices for the diattenuation, retardation and depolarization components respectively. Firstly, it must be noted that this decomposition is made solely for interpreting the polarimetric data and extracting physical parameters more conveniently by capturing the effective polarization transformation and doesn't necessarily describe the actual physical underlying process. This is specially the case for biological tissues for which the depolarization, diattenuation and retardation effects are likely to occur simultaneously [Vitkin et al., 2015b, Ghosh et al., 2009, Gao, 2021]. Secondly, due to the fact that in general the matrix product is non-commutative, the decomposition order given in Eq. (4.9) is not the only decomposition that one can make out of the original Mueller matrix. Based on the optical characteristics of the sample, there exist a multitude of ways to break down the total Mueller matrix into a combination of the elementary ones, of which Eq. (4.9) is only a special case [Vitkin et al., 2015b, Lu and Chipman, 1996b, Ghosh et al., 2009, Gao, 2021, Morio and Goudail, 2004, Gil et al., 2013, Ossikovski et al., 2007, Ossikovski, 2012, Ortega-Quijano and Arce-Diego, 2011, Ossikovski et al., 2008]. Based on Eq. (4.8) we can describe the quantum mechanical polarization channels as [Goldberg, 2020]

$$\varepsilon(\hat{\rho}) = \varepsilon_d \circ \varepsilon_R \circ \varepsilon_D(\hat{\rho}), \tag{4.10}$$

in which ε_D, ε_R and ε_d are the diattenuator, retarder and depolarizer channels, respectively. A schematic representation of this channel is given in Fig. 4.1(a). The retarder channel rotates the Stokes vector which also acts as a unitary rotation on the density matrix [Goldberg and James, 2018, Goldberg, 2020, Goldberg, 2021, Goldberg, 2022a]:

$$\varepsilon_R(\hat{\rho}) = \hat{R}(\theta, \mathbf{n})\hat{\rho}\hat{R}^\dagger(\theta, \mathbf{n}). \tag{4.11}$$

Here, the operator $\hat{R}$ is given by

$$\hat{R}(\theta, \mathbf{n}) = \exp(i\theta\hat{\mathbf{S}}.\mathbf{n}), \tag{4.12}$$

in which $\mathbf{n} = (\Theta, \Phi)$ is the rotation axis with and θ is the angle of rotation. In composite, anisotropic media such as biological tissues, retardation phenomena may arise from various factors such as reflection, refraction at interfaces, or propagation

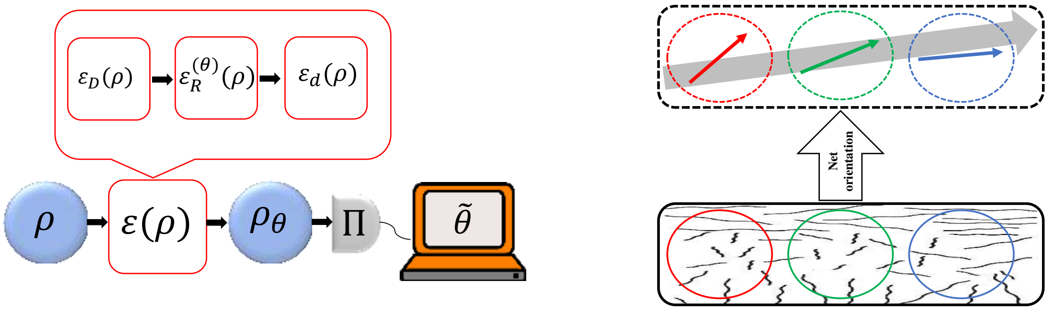

(a) (b)

Figure 4.1: (a) A schematic representation of the general polarization channel. In this figure the order of the action of the diattunator, retarder and depolarizer channels follows the standard Lu-Chipman form. (b) Distribution of fibers in an inhomogeneous biological sample and overall rotation axis experienced by the probe. The large gray arrow represents the net rotation axis for the entire sample and the smaller colored arrows in dashed circles represents the local net rotation axis for the respective fiber distribution at each specific subsection of the sample.

through the medium. Notably, these materials harbor distributed fibers, such as collagen fibers, exhibiting non-uniform distribution throughout the sample. While initial models often assumed uniformity in the refractive index difference between ordinary and extraordinary axes, and the uniform direction of the extraordinary axis across the sample, recent investigations have begun to challenge this simplification [Vitkin et al., 2015b]. The orientation of the retarder axis aligns with the prevailing direction of these fibers within a specific volume of the sample [Vitkin et al., 2015b]. However, during local probing of the sample, fiber orientations may locally fluctuate across different subsections, as illustrated in Fig. 4.1(b). Moreover, reconstructing three-dimensional images from various sections to ascertain fiber direction introduces inherent noise susceptibility, leading to inevitable uncertainties in inferred orientations [Jones, 2003, Bancelin et al., 2014, Menzel et al., 2017, Schmitz et al., 2020, Chang et al., 2023]. Consequently, among the retarder's three parameters, two primarily dictate the resultant fiber orientation—thus determining the rotation axis, albeit subject to uncertainty arising from the aforementioned factors—while the remaining parameter quantifies the degree of rotation, facilitating estimation of sample thickness. Our focus lies solely on accurately estimating the rotation angle.

The diattenuator channel can be modeled by a sequential application of rotation operators in an enlarged Hilbert space containing two ancillary modes and tracing out the ancillary modes. It is given by [Goldberg, 2020, Goldberg, 2021, Goldberg, 2022a]

$$\varepsilon_D(\hat{\rho}) = \mathrm{Tr}_{v_1,v_2}[\hat{U}_D(\hat{\rho} \otimes |\mathrm{vac}\rangle_{v_1,v_2\,v_1,v_2}\langle\mathrm{vac}|)\hat{U}_D^{\dagger}], \tag{4.13}$$

in which v_1 and v_2 are the ancillary modes and the operator $\hat{U}_D$ is

$$\begin{aligned} \hat{U}_D = \hat{R}^{\dagger}_{a,b}(0,\beta,\gamma)\hat{R}_{b,v_2}(0,-2\cos^{-1}(0,\sqrt{r},0)) \\ \hat{R}_{a,v_1}(0,-2\cos^{-1}(0,\sqrt{q},0))\hat{R}_{a,b}(0,\beta,\gamma). \end{aligned} \tag{4.14}$$

Here, $\hat{R}_{a,b}$ denotes a rotation operator between modes a and b parametrized by the Euler angles $(0,\beta,\gamma)$. $\hat{R}_{a,v_1}$ and $\hat{R}_{b,v_2}$ are rotations between modes a and v_1 and b and v_2 correspondingly with their respective attenuation parameters q and r. For the case of depolarization, one can give a classical-like decomposition of a state into a convex combination of the completely polarized state and the isotropic state [Goldberg, 2020].

$$\varepsilon_d^{(c)}(\hat{\rho}) = p\hat{\rho}_{pol} + (1-p)\sum_N p_N \frac{\hat{\mathcal{I}}_N}{N+1}, \tag{4.15}$$

in which p is the depolarization parameter and p_N is the weight factor in each photon number subspace. However, this decomposition doesn't always work for the case of quantum states and also, such a convex combination can only describe single photon states and classical states undergoing isotropic depolarization [Goldberg, 2022a, Goldberg, 2022b, Goldberg, 2021]. We can construct a quantum depolarization channel by a convex combination of different rotation operators [Goldberg, 2021, Goldberg, 2022a].

$$\varepsilon_d^{(r)}(\hat{\rho}) = \sum_{i=1}^{n} P(i)\hat{R}_i\hat{\rho}\hat{R}_i^{\dagger}. \tag{4.16}$$

In Eq. (4.16), $P(i)$ is the probability for the rotation operator $\hat{R}_i$ and the sum of all the probabilities must add up to one. Depolarization can be caused by the interaction of light with an ensemble of atoms due to random rotations induced by the interaction on the photonic state [Klimov et al., 2006, Klimov et al., 2008, Rivas and Luis, 2013]. The channel given in Eq. (4.16) is a simple model for such a physical process [Goldberg, 2021]. However, there are also models for depolarization of quantum states based on master equations [Klimov et al., 2006, Klimov et al., 2008, Rivas and Luis, 2013], two of which are presented in Eq. (4.17) and Eq. (4.18).

$$\mathcal{L}_d^{(i)}(\hat{\rho}) = \frac{d\hat{\rho}}{dt} = \nu_i(\mathcal{D}(\hat{S}_1)\hat{\rho} + \mathcal{D}(\hat{S}_2)\hat{\rho} + \mathcal{D}(\hat{S}_3)\hat{\rho}), \tag{4.17}$$

$$\mathcal{L}_d^{(a)}(\hat{\rho}) = \frac{d\hat{\rho}}{dt} = \nu_{a_0}\mathcal{D}(\hat{S}_0)\hat{\rho} + \nu_a(\mathcal{D}(\hat{S}_2)\hat{\rho} + \mathcal{D}(\hat{S}_3)\hat{\rho}). \tag{4.18}$$

In Eq. (4.17) and Eq. (4.18), the expression $\mathcal{D}(\hat{A})\hat{\rho} \equiv 2\hat{A}\hat{\rho}\hat{A}^\dagger - \hat{A}^\dagger\hat{A}\hat{\rho} - \hat{\rho}\hat{A}^\dagger\hat{A}$ denotes the dissipator superoperator with the jump operator $\hat{A}$, while $\mathcal{L}_d^{(i)}$ and $\mathcal{L}_d^{(a)}$ represent the Lindblad generators governing their respective Markovian depolarization dynamics. Consequently, we establish a connection between these generators and their associated channels as $\varepsilon_{d_t}^{(x)}(\hat{\rho}) = \exp(\mathcal{L}_d^{(x)}t)\hat{\rho}(0)$, where $x = i, a$. It is important to differentiate between the two depolarization master equations: in Eq. (4.18), unlike Eq. (4.17), the depolarization rates along the three axes $\hat{S}_1$, $\hat{S}_2$ and $\hat{S}_3$ are not equal. Moreover, it's worth noting that the dissipator $\mathcal{L}(\hat{S}_0)$ in Eq. (4.18) holds no relevance for depolarization dynamics. Accordingly, the master equations described in Eq. (4.17) and Eq. (4.18) are commonly referred to as the isotropic and anisotropic depolarization channels, respectively. The master equation in Eq. (4.17) is also recognized as the $\mathfrak{su}(2)$-invariant depolarization in literature [Rivas and Luis, 2013].

While the isotropic depolarization, as delineated by the Markovian master equation in Eq. (4.17), exhibits a more intricate dynamic behavior compared to the semi-classical phenomenological channel outlined in Eq. (4.16) [Denis and Martin, 2022], it inherently assumes that the probability distribution governing the rotation vector (encompassing both rotation direction and angle) is solely contingent upon the magnitude of said vector. Consequently, transformations with non-negligible probability primarily involve small magnitudes of the rotation vector, hence implying small rotation angles. Consequently, the isotropic depolarization channel can be conceptualized as a composite of numerous small rotation operators. On the other hand, the dynamics governing anisotropic depolarization are derived within the weak coupling limit, thereby implying small rotation angles, and are subject to the rotating wave approximation and Markovianity assumption [Klimov et al., 2006, Klimov et al., 2008]. A thorough examination of isotropic and anisotropic depolarization dynamics concerning spin states is undertaken in [Denis and Martin, 2022].

4.3 Majorana Constellations and Quantumness of Polarization States

A quantum state describing a particle with angular momentum or spin S is in a $(2S+1)$-dimensional Hilbert space $\mathcal{H}_S$. For spin S, we label $2S+1$ levels as $m = -S, ..., S$. $\mathcal{H}_S$ is spanned by the set of basis $|S, m\rangle$, which is usually called the angular momentum basis or Dicke basis. One should note that for spin S the space of states is $\mathcal{H}_S \in \mathbb{C}^{2S+1}$ but for angular momentum the space of bound states is the infinite sum of such spaces for every possible value that S can take, $\mathcal{H} = \bigoplus_S \mathcal{H}_S$ [Bengtsson and Zyczkowski, 2006]. Additionally, $\mathcal{H}_S$ is the carrier of the irreducible representation (irrep) of spin S of $\mathfrak{su}(2)$, and therefore any two states in $\mathcal{H}_S$ which only differ by an $\mathfrak{su}(2)$ rotation are physically equivalent. An arbitrary pure state describing such a system can be written as

$$|\Psi\rangle = \sum_{m=-S}^{S} c_S \, |S, m\rangle \, . \tag{4.19}$$

Using a method called the Majorana spin representation, one can construct an arbitrary pure state with angular momentum S as a superposition of $2S$ spin-1/2 systems. Note that although the Hilbert space of S spin-1/2 systems $\mathcal{H} \in \mathbb{C}^{2^S}$ is of dimension 2^S, its symmetric subspace, is of dimension $2S+1$ [Bengtsson and Zyczkowski, 2006, Giraud et al., 2015]. Majorana showed that there exists a bijection between the pure spin state given in Eq. (4.19) and roots of the polynomial $M(z)$, which is called the Majorana polynomial [Majorana, 1932, Bengtsson and

Zyczkowski, 2006].

$$M(z) = \sum_{k}^{2S} c_k \binom{2S}{k}^{1/2} z^{2S-k}. \tag{4.20}$$

The roots ξ_k of $M(z)$ in turn, have bijective correspondence to the points on $\mathcal{S}^2$. Therefore, one can uniquely represent the angular momentum state $|\psi\rangle$ in Eq. (4.19) on the surface of the extended complex plane (Riemann sphere), up to the action of $\mathfrak{su}(2)$ rotations [Bengtsson and Zyczkowski, 2006]. One can accomplish this task by the stereographic projection

$$\tan^{-1}(\frac{\theta_k}{2})e^{i\phi_k} = \xi_k, \tag{4.21}$$

in which θ_k and ϕ_k are the polar and azimuthal coordinates for a point on the sphere. Within the symmetric subspace of the Hilbert space that we mentioned earlier, using Majorana representation one can decompose the angular momentum state in Eq. (4.19) as a single product of individual spin-1/2 systems.

$$|\Psi\rangle = \bigotimes_{k=1}^{2S} |\psi_k\rangle\,, \quad |\psi_k\rangle = \cos\frac{\theta_k}{2}\,|0\rangle + e^{i\phi_k}\sin\frac{\theta_k}{2}\,|1\rangle\,. \tag{4.22}$$

Schwinger showed that commutation relations of an angular momentum operator can be reduced to those of a two-dimensional harmonic oscillator and using a transformation one can map quantum mechanical spins onto bosonic fields [Schwinger, 1977]. This method is called Schwinger boson representation, which is a special case of Jordan-Schwinger map. Upon application of this method the Schwinger boson representation of the angular momentum operators takes the form given in Eq. (4.3) for the Stokes operators. In light of this transformation, we can express the quantum polarization states expressed using Fock basis in Eq. (4.1) using Dicke (angular momentum) basis. The optical state can be thought of as a collection of spin-1/2 states with $n_1 = S + m$ particles in spin-up and $n_2 = S - m$ particles in spin-down states. It should be noted that, by construction, unlike the usual angular momentum addition rules, combining the mentioned spin up and down states will result in a symmetric state with $n_1 + n_2 = 2S$ spin-1/2 particles with total spin S. The polarization state in Dicke basis is given by

$$|n_1, n_2\rangle \equiv |S, m\rangle = \frac{\hat{a}^{\dagger(S+m)}\hat{b}^{\dagger(S-m)}}{\sqrt{(S+m)!(S-m)!}} |0, 0\rangle \,. \tag{4.23}$$

Due to the isomorphism that is established by Schwinger boson representation between spin systems and two-mode bosonic systems, one can use Majorana's method to represent any pure polarization state with $n = 2S$ photons as a collection of points on the surface of a Riemann sphere (Poincare sphere within the context of polarization optics).

$$\begin{aligned} |\Psi\rangle &= \frac{1}{\mathcal{N}_n(U)} \prod_{k=1}^{n} \hat{a}^\dagger_{u_k} |0, 0\rangle \,, \\ \hat{a}^\dagger_{u_k} &= \cos(\frac{\theta_k}{2})\hat{a}^\dagger + e^{i\phi_k} \sin(\frac{\theta_k}{2})\hat{b}^\dagger. \end{aligned} \tag{4.24}$$

In Eq. (4.24), $\mathcal{N}_n(U)$ is the normalization factor which is a function of $U \equiv \{u_1, ..., u_{2S}\}$ and $u_k = (\theta_k, \phi_k)$ are the coordinates of the points on the Poincare sphere, which are called the constellations of the state. The normalization factor is given by [Liu and Fu, 2016, Lee, 1988]

$$\begin{aligned} \mathcal{N}_n(U) &= \left[\frac{(n+1)!}{2^n} \sum_{k=0}^{[n/2]} \frac{D^n_k}{(2k+1)!!} \right]^{\frac{1}{2}} , \\ D^n_k &\equiv \sum_{i_1=1}^{n} \sum_{j_1>i_1}^{n} ... \sum_{i_k>i_{k-1}}^{n*} \sum_{j_k>i_k}^{n*} (u_{i_1}.u_{j_1})...(u_{i_k}.u_{j_k}). \end{aligned} \tag{4.25}$$

In Eq. (4.25), in the first line, $[\bullet]$ at the upper limit of the sum signifies the floor function and in the second line, $*$ indicates a restriction on the summations such that the values that the indices take in each term must all be different.

The methodology described so far, explains how to represent a general pure polarization state as a constellation of points on the surface of a sphere and its connection to the original method by Majorana developed for quantum angular momentum states. However, it is constructive to briefly describe another approach based on coherent states to make connections between the constellations, quasi-probability distribution and different notions of quantumness of polarization states. It is convenient to express the Bloch coherent (also known as spin coherent, atomic coherent and $\mathfrak{su}(2)$ coherent) state using Dicke basis.

$$|z\rangle = \hat{D}(\theta,\phi)\,|S,-S\rangle = \frac{1}{(1+|z|^2)^S}\sum_{-S}^{S}\binom{2S}{S+m}^{\frac{1}{2}} z^{S+m}\,|S,m\rangle\,. \tag{4.26}$$

In Eq. (4.26), $\hat{D}$ is the displacement operator on $\mathcal{S}^2$. Any pure state in Dicke basis can be written as Eq. (4.19). The stellar function (also known as Fock-Bargmann representation) of the state for $\mathcal{H}_S$ is defined using the overlap between the state Eq. (4.19) and the Bloch coherent state [Bargmann, 1961, Gazeau, 2009].

$$F(z) = (1+|z|^2)^S\,\langle\Psi^*|z\rangle = \sum_{m=-S}^{S} c_S\binom{2S}{S+m}^{\frac{1}{2}} z^{S+m}. \tag{4.27}$$

In Eq. (4.27) we used the following notation.

$$\langle\Psi| = \sum_{m=-S}^{S} c_S\,\langle S,m|\,;\quad |\Psi^*\rangle = \sum_{m=-S}^{S} c_S^*\,|S,m\rangle\,;\quad \langle\Psi^*| = \sum_{m=-S}^{S} c_S\,|S,m\rangle\,. \tag{4.28}$$

It is worth mentioning that the stellar function can also be defined in $\mathcal{H}_\infty$ (continuous-variable quantum systems) using the canonical coherent states [Gazeau, 2009, Goldberg et al., 2020]. $F(z)$ is a holomorphic function which provides an analytic representation of a quantum state. The transformation in Eq. (4.27) defines the Bargmann-Segal transform on the spin coherent states which maps a quantum state to the space of holomorphic functions, called the Segal–Bargmann space [Bargmann, 1961, Goldberg et al., 2020, Hall, 1994, Gazeau, 2009]. The Bargmann representation is directly related to the Husimi Q-function, which is a quasi-probability distribution on the phase space. For the case of a pure state $\hat{\rho} = |\Psi\rangle\langle\Psi|$ and this relationship becomes

$$Q(z) = \langle z|\hat{\rho}|z\rangle = (1+|z|^2)^S|F(z^*)|^2. \tag{4.29}$$

Husimi function (unlike Wigner function) is non-negative definite and is bounded by $0 \leq Q(z) \leq 1/\pi$. It is evident that the zeros of the Husimi Q-function are the complex conjugates of the zeros of the stellar function. The Q function also has a geometric interpretation on the manifold of quantum states. The Fubini-Study distance between states $|\Psi\rangle$ and $|z\rangle$ is related to the Q function by $\mathbb{D}_{FS} =$

arccos$\sqrt{Q(z)}$. Using Husimi Q-function one can define Wehrl entropy on the sphere ($\mathcal{H}_S$) as

$$S_W(\hat{\rho}) = -\frac{2S+1}{4\pi}\int_{\mathcal{S}^2} dzQ(z)\text{ln}Q(z). \tag{4.30}$$

Unlike Von-Neumann entropy, Wehrl entropy doesn't vanish for pure states and is always positive. It can be interpreted as an information measure for a joint noisy measurement of position and momentum of the quantum system. Lieb and Solovej proved that Wehrl entropy on $\mathcal{H}_S$ is lower bounded by

$$S_W(\hat{\rho}) \geq \frac{2S}{2S+1}, \tag{4.31}$$

and the lower bound is attained only for the Bloch coherent states for which the Majorana constellations are concentrated at a single point on the Poincare sphere [Lieb and Solovej, 2014, Goldberg et al., 2020]. The more spread out the points are on the sphere, the larger the value of the Wehrl entropy becomes. It is also proven that canonical coherent states minimize Wehrl entropy on the space of states defined on $\mathcal{H}_\infty$ [Lieb, 1978]. Since the coherent states are known to be the most classical-like states, one can interpret the Wehrl entropy as a measure of non-classicality such that the larger the value for $S_W(\hat{\rho})$ is, more "distant" the state becomes from the Bloch coherent states. In this sense, the states that maximize the Wehrl entropy, for which the Majorana constellations are distributed such that the points are as far away as possible from each other on the unit sphere, are the most quantum ones. For these states the Majorana points are distributed symmetrically on the Poincare sphere. To obtain these maximally non-classical states, for each S, one must solve an optimization problem. However, the problem of optimizing the value of $S_W(\hat{\rho})$ based on the positions of the Majorana points on $\mathcal{S}^2$ is extremely challenging, especially for larger values of S [Lee, 1988, Schupp, 1999]. These states are obtained for a limited set of values of S, not by full-scale optimization, but by selecting a set of candidates for the optimal states based on the geometry of the constellations and checking if the selected states result in a local maxima for $S_W(\hat{\rho})$ [Baecklund and Bengtsson, 2014, Baecklund, 2013]. We must make it clear that maximization of Wehrl entropy is not the only criterion for finding the "maximally quantum" states in the literature. Depending on the problem under investigation, there are various procedures to find such states. Application of different extremum principles result in a different set of maximally quantum states for discrete variable systems, as opposed to the continuous variable case [Goldberg et al., 2020]. The important theme underlying the methodology for finding such states is that all of these methods are based on identifying an suitable functional of quantum states and finding the maximally quantum states by optimizing that functional. For a more detailed explanation of such procedures the readers can refer to [Goldberg et al., 2020, Giraud et al., 2010, Aulbach et al., 2010, Baguette et al., 2014, Hübener et al., 2009].

One can verify that in the case of mentioned maximally quantum states, due to the fact that the constellations are symmetrically distributed on $\mathcal{S}^2$, the polarization measure defined in Eq. (4.5) vanishes. Although these states are classically unpolarized, they contain hidden polarization which can be understood as a manifestation of the higher moments of the Stokes operators [Goldberg et al., 2021a, Luis, 2002, Hübener et al., 2009, Sánchez-Soto et al., 2013]. One can expand a general polarization state in terms of irreducible tensors as

$$\hat{\rho} = \sum_{K=0}^{2S} \sum_{q=-K}^{K} \rho_{Kq} \hat{T}_{Kq}^{(S)}. \tag{4.32}$$

In Eq. (4.32), $\hat{T}_{Kq}^{(S)}$ are the irreducible tensors defined as [Goldberg et al., 2021a, Goldberg et al., 2020]

$$\hat{T}_{Kq}^{(S)} = \sqrt{\frac{2K+1}{2S+1}} \sum_{m,m'=-S}^{S} C_{Sm,Kq}^{Sm'} \left|S, m'\right\rangle\langle S, m| \,, \tag{4.33}$$

in which $C_{Sm,Kq}^{Sm'}$ are the Clebsch–Gordan coefficients that couple a spin S and a spin K ($0 \leq K \leq 2S$) to a total spin S. The tensors form an orthonormal basis $\mathrm{Tr}[\hat{T}_{Kq}^{(S)}(\hat{T}_{K'q'}^{(S')})^{\dagger}] = \delta_{SS'}\delta_{KK'}\delta_{qq'}$ and are covariant under $\mathfrak{su}(2)$ transformations. The expansion coefficients $\rho_{Kq} = \mathrm{Tr}(\hat{\rho}\hat{T}_{Kq}^{\dagger})$ are known as the state multipoles. Complete characterization of the state requires knowledge of all of these multipoles. One can use these multipoles to expand the Q function as [Goldberg et al., 2021a, Goldberg et al., 2020]

$$Q(z) = \sum_{K=0}^{2S} Q^{(K)}, \tag{4.34}$$

where $Q^{(K)}$ is the K^{th} multipole of the Q function and contains information of the K^{th} moment of the Stokes operators. It can be expressed as [Goldberg et al., 2021a, Goldberg et al., 2020]

$$\begin{aligned} Q^{(K)} &= \sqrt{\frac{4\pi}{2S+1}} \sum_{q=-K}^{K} C^{SS}_{SS,K0} \rho_{Kq} Y^{*}_{Kq}, \\ C^{SS}_{SS,K0} &= \frac{\sqrt{2S+1}(2S)!}{\sqrt{(2S-K)!(2S+1+K)!}}, \end{aligned} \tag{4.35}$$

in which Y^{*}_{Kq} are the spherical harmonics and in the second line of Eq. (4.35) the analytical form for the Clebsch–Gordan coefficient $C^{SS}_{SS,K0}$ is given. Since it is calculated using all of the state multipoles, the Husimi Q function (and therefore the Wehrl entropy), contains complete information of the state. One can utilize the information encoded in the Q function to define a distance based polarization measure which takes into account the contributions from all of the multipoles [Luis, 2002]

$$\mathbb{P}_q = 1 - \frac{1}{4\pi}\Sigma, \quad \Sigma = \frac{1}{\int d\Omega [Q(\theta,\phi)]^2}. \tag{4.36}$$

In Eq. (4.36), the DOP of a state is defined as the distance between the Q function of that state and the Q function for the maximally unpolarized state ($Q_{\text{unpol}} = 1/4\pi$). The DOP defined in Eq. (4.36) is more suitable for quantum states of light compared to Eq. (4.5) because, as explained previously, the higher order multipoles play a more significant role in the polarization behavior of the quantum states. However, in most of the cases, one can gain substantial amount of information on polarization characteristics of the state only considering a finite number of its multipoles. A useful quantity which encodes the polarization information of a quantum state up to its M^{th} order is the M^{th} order cumulative multipolar distribution defined below [Goldberg et al., 2021a, Sánchez-Soto et al., 2013, Goldberg et al., 2020].

$$\mathcal{A}_M = \sum_{K=1}^{M} \sum_{q=-K}^{K} |\rho_{Kq}|^2. \tag{4.37}$$

$\mathfrak{su}(2)$ coherent states maximize $\mathcal{A}_M$ for all orders M. The states that minimize $\mathcal{A}_M$ are called Kings of Quantumness (anticoherent states). A state is called M-anticoherent if for all $t \leq M$ and unit vectors $\mathbf{n}$ the moments of the Stokes vector are isotropic $\langle(\hat{\mathbf{S}}.\mathbf{n})^t\rangle = c_t$ and independent of $\mathbf{n}$. It is shown that the states with the anticoherence order of 2 and higher are optimal for estimating all three rotation parameters [Chryssomalakos and Hernández-Coronado, 2017, Bouchard et al., 2017, Kolenderski and Demkowicz-Dobrzanski, 2008, Goldberg and James, 2018, Martin et al., 2020, Goldberg et al., 2021b, Eriksson et al., 2023].

4.4 Results

In this section we numerically calculate the QFI for the rotation angle θ in order to determine its ultimate measurement precision. In all of our calculations the rotation angle to be estimated is $\theta = \pi/10$, which falls into the range of small angles for which the Kings of Quantumness yield optimal sensitivity [Martin et al., 2020] for every value of S considered in this study. The probe states that have been considered for this task are the coherent state, NOON states and Kings of Quantumness. For estimation of small rotation angles, coherent state saturates SQL, NOON state saturates HL as long as the rotation axis is not orthogonal to $(\Theta, \Phi) = (0, 0)$ axis (maximum sensitivity occurs for $(\Theta, \Phi) = (0, 0)$ axis), and anticoherent states saturate HL for all rotation axes [Goldberg and James, 2018]. Because of the dependence of the precision of NOON state on the rotation axis, the optimal strategy is to align the sample such that $(\Theta, \Phi) = (0, 0)$ axis corresponds to the net orientation direction of the fibers. However, as explained earlier, in realistic cases there will be an uncertainty in the direction of this axis. The Kings of Quantumness utilized in our calculations are taken from [Martin et al., 2020]. For all optical modes, the cut-off dimension for Hilbert space is taken to be 12. In our calculations we have used the open source QuTiP [Johansson et al., 2012a, Johansson et al., 2013] and QuanEstimation [Zhang et al., 2022b] packages for Python. As a reference, our numerical results for the QFI in case of no depolarization and diattenuation is presented in Fig. 4.2.

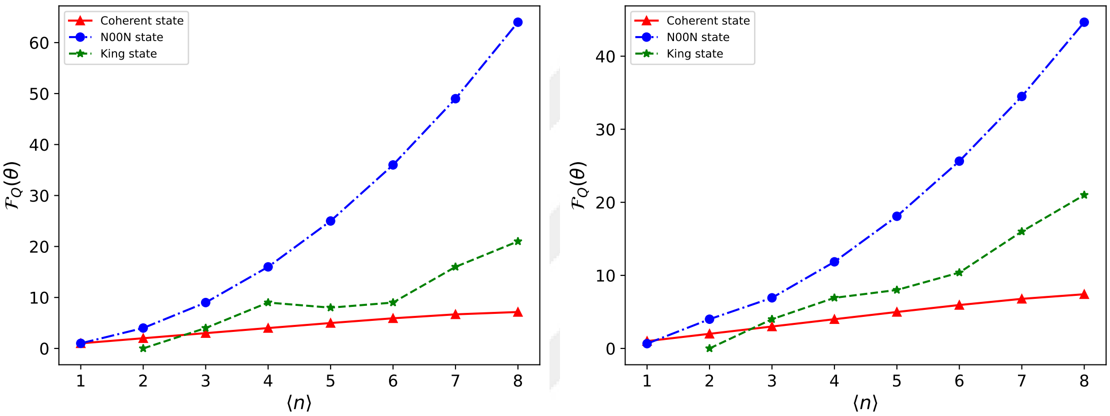

(a) (b)

Figure 4.2: QFI for rotation angle (no depolarization and diattenuation) vs average photon number. Calculations are for coherent state (solid line with triangular data points in red), NOON state (dash dotted line with circular data points in blue) and Kings of Quantumness (dashed green line with star datapoints) for (a) $(\Theta, \Phi, \theta) = (0, 0, \pi/10)$ (b) $(\Theta, \Phi, \theta) = (\pi/5, 0, \pi/10)$

.

In Fig. 4.2(a) we consider a perfect alignment of the optimal axis for the NOON state ($(\Theta, \Phi) = (0, 0)$) and the retarder axis and in Fig. 4.2(b) we consider an uncertainty in the retarder axis which creates a misalignment between the two directions. Comparing Fig. 4.2(a) and Fig. 4.2(b) we see that, as expected, the QFI for NOON state reduces when the rotation axis is not aligned along its optimal axis, although it scales quadratically with the average photon number in both cases. QFI for coherent state scales linearly with $\langle n \rangle$ regardless of the rotation direction. The Kings of Quantumness (referred to as the King state in the figures) result in a larger value for QFI compared to the coherent state except for $S = 1$ ($\langle n \rangle = 2$) which corresponds to the bi-photon state (which is 1-anticoherent). For both of the rotation axes, NOON state achieves a higher sensitivity than the Kings of Quantumness. In Fig. 4.2(a) we observe non-monotonicity in QFI for Kings of Quantumness at $S = 5/2$ ($\langle n \rangle = 5$). This is not surprising if we consider the fact that optimal rotation sensors must be 2-anticoherent but for $S = 5/2$ the state is only 1-anticoherent [Martin et al., 2020]. However, in Fig. 4.2(b) the QFI for Kings of quantumness is monotonic with $\langle n \rangle$ and the precision limits for θ are slightly different as compared to Fig. 4.2(a). It is instructive to assess the performance of these states by considering the effect of each of the noise channels on the estimation precision of the rotation angle. Therefore, in Section 4.4.1 we will study the effect of the depolarization channel on the QFI for the rotation angle and in Section 4.4.2 the joint effect of depolarization and diattenuation is considered. In both of these cases the ordering of the implementation of the channels is also considered. Based on the polarimetric studies in biological tissues [Jones, 2003, Bancelin et al., 2014, Menzel et al., 2017, Schmitz et al., 2020, Chang et al., 2023], in all subsequent calculations we will take the retarder axis to be $(\Theta, \Phi) = (\pi/5, 0)$ with a misalignment of $\pi/5$ with the optimal axis for the NOON state. Using the terminology common in the classical polarimetry, we will call $\varepsilon_{\text{for}}(\hat{\rho}) = \varepsilon_d \circ \varepsilon_R \circ \varepsilon_D(\hat{\rho})$ as the "forward" decomposition and $\varepsilon_{\text{rev}}(\hat{\rho}) = \varepsilon_D \circ \varepsilon_R \circ \varepsilon_d(\hat{\rho})$ as the "reverse" decomposition.

4.4.1 Noisy Rotation Sensing with Depolarization

In this section we calculate the QFI for the rotation angle induced by the retarder, in both forward and reverse processes without considering the effect of diattenuation, focusing only on depolarization. We have considered 3 depolarization channels, namely the isotropic, anisotropic and using convex combination of rotations. Since in the master equation for the anisotropic depolarization Eq. (4.18), the dissipator $\mathcal{D}(\hat{S}_0)$ is irrelevant for depolarization [Rivas and Luis, 2013], we set $\nu_{a_0} = 0$ for the master equation. For implementing the depolarization channel based on convex combination of rotations we have assumed a range of equally spaced n_r rotation angles between η_{min} and η_{max} with rotation probabilities in Eq. (4.16) given by a normal distribution with mean at zero rotation angle. One can choose which rotation angles to include and their probabilities by changing the range of angles considered and the standard deviation σ_r for the normal distribution respectively. To make sure that no rotation axis or decomposition order is preferred, we took an average of the results given by all 6 permutations of the convex combination of n_r rotations using three rotation operators $\hat{R}_1 = \exp(-i\phi\hat{S}_1)$, $\hat{R}_2 = \exp(-i\phi\hat{S}_2)$ and $\hat{R}_3 = \exp(-i\phi\hat{S}_3)$. We stress that our choice of depolarization channel, although is physically motivated, is only a specific one among an infinite number of choices that are possible based on Eq. (4.16). For all depolarization channels we considered low and high depolarization regimes in our calculations. The results for isotropic, anisotropic and random rotation depolarization channels are presented in Fig. 4.3, Fig. 4.4 and Fig. 4.5 respectively.

It is clear that for all of the considered cases, introducing depolarization greatly reduces the measurement sensitivity of the retardation angle. Reduction in QFI is more dramatic for larger depolarization values. Additionally for all depolarization channels there is no difference in terms of metrological power between forward and reverse decomposition for coherent state. The isotropic depolarization channel is $\mathfrak{su}(2)$-invariant and as discussed in the derivation of master equation Eq. (4.17) in [Rivas and Luis, 2013] different ordering of rotation and depolarization channels

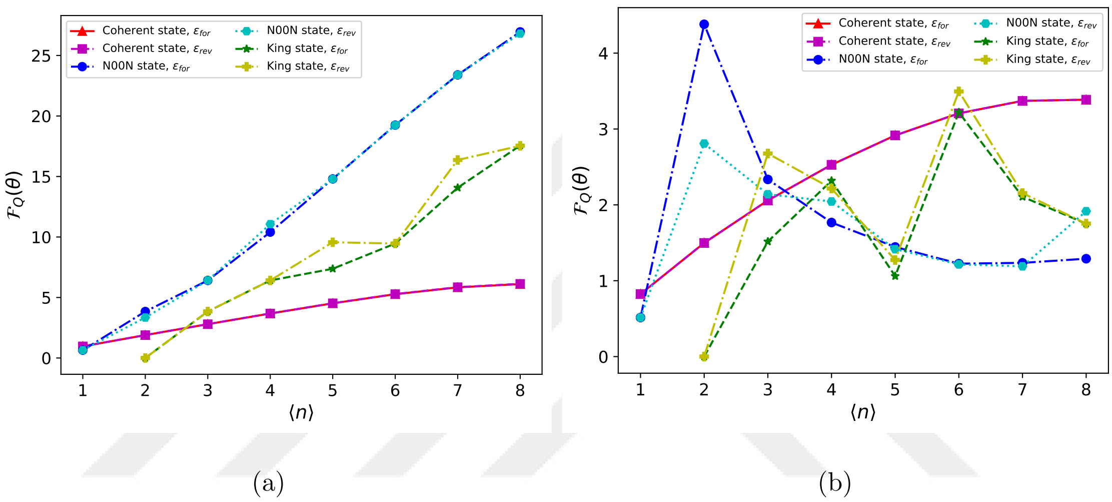

(a) (b)

Figure 4.3: QFI for rotation angle in presence of isotropic depolarization noise vs average photon number. Calculations are for coherent state in forward (solid line with triangular data points in red) and reverse (dashed line with square data points in magenta) processes, NOON state in forward (dash dotted line with circular data points in blue) and reverse (dotted line with triangular data points in cyan) processes and Kings of Quantumness in forward (dashed green line with star datapoints) and reverse (dash-dotted yellow line with plus shaped datapoints) processes for (a) $\nu_i t = 0.003$ (b) $\nu_i t = 0.03$.

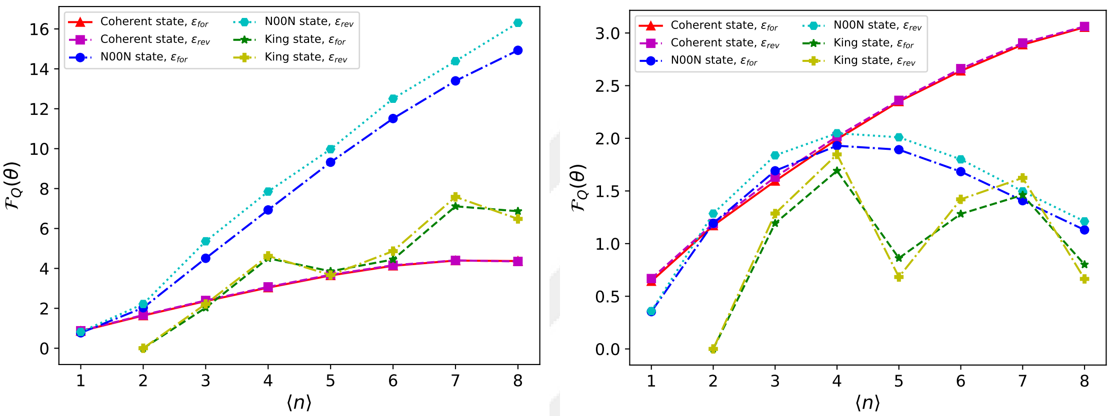

(a) (b)

Figure 4.4: QFI for rotation angle in presence of anisotropic depolarization noise vs average photon number. Calculations are for coherent state in forward (solid line with triangular data points in red) and reverse (dashed line with square data points in magenta) processes, NOON state in forward (dash dotted line with circular data points in blue) and reverse (dotted line with triangular data points in cyan) processes and Kings of Quantumness in forward (dashed green line with star datapoints) and reverse (dash-dotted yellow line with plus shaped datapoints) processes for (a) $\nu_a t = 0.05$ (b) $\nu_a t = 0.15$.

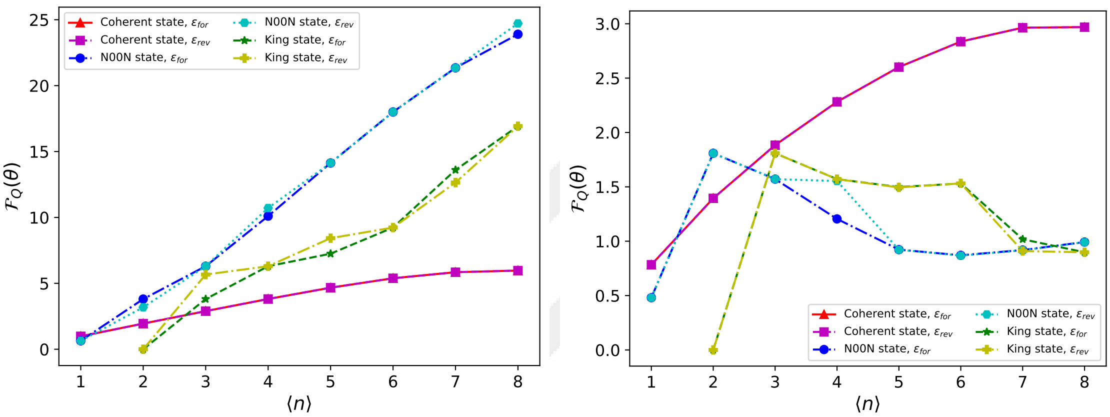

(a) (b)

Figure 4.5: QFI for rotation angle in presence depolarization noise based on convex combination of rotations vs average photon number. Calculations are for coherent state in forward (solid line with triangular data points in red) and reverse (dashed line with square data points in magenta) processes, NOON state in forward (dash dotted line with circular data points in blue) and reverse (dotted line with triangular data points in cyan) processes and Kings of Quantumness in forward (dashed green line with star data points) and reverse (dash-dotted yellow line with plus shaped datapoints) processes for (a) $[\eta_{min}, \eta_{max}] = [-\pi/8, \pi/8]$, $\sigma_r = \pi/32$, $n_r = 6$ (b) $[\eta_{min}, \eta_{max}] = [-\pi, \pi]$, $\sigma_r = \pi/8$, $n_r = 20$.

should yield the same result. Additionally, as explained earlier, the depolarization channel based on convex combinations of rotations is chosen such that the effects of decomposition order and choice of rotation axis for depolarization is minimized. However, from Fig. 4.3 and Fig. 4.5 we see that there are differences between forward and reverse decomposition for NOON state and Kings of Quantumness, the difference being larger for higher depolarization. These differences can be present due to a few reasons. First of all, due to numerical nature of our study, the results inevitably contain numerical errors. Also, from the explicit relation given for ν_{iso} in [Rivas and Luis, 2013] we see that for larger values of ν_{iso} either the time derivative of the probability distribution for the rotation vectors comprising the depolarization channel or the amplitude of the rotation vectors must be large. The latter condition weakens the $\mathfrak{su}(2)$-invariance condition because for perfect $\mathfrak{su}(2)$-invariance to hold the rotations must be infinitesimally small.

Interestingly, in Fig. 4.4(a) we see that for the anisotropic depolarization channel, the metrological performance for the NOON state and Kings of Quantumness is slightly better for the case of reverse decomposition. Inspecting Fig. 4.4(b) we see that this advantage still holds for a larger amount of depolarization. It is also clear from our results that for all depolarization channels considered, NOON state and Kings of Quantumness lose their metrological power faster when depolarization is applied, compared with the coherent state. This confirms the common understanding that quantum states are more susceptible to noise compared to the classical states. Needless to say that for stronger depolarization than what we considered in this study, the coherent state results in a larger QFI than the quantum probe states for all average photon numbers. Another general feature underlying all depolarization channels is that the QFI vs $\langle n \rangle$ is no longer monotonic for all states except the coherent state, specially for large depolarization. This might be rather surprising considering the fact that usually the QFI scales monotonically with the number of resources. However, as discussed in [Rivas and Luis, 2013] and [Denis and Martin, 2022], different state multipoles have different decay rates and states with a larger S values experience a larger decay.

4.4.2 Noisy Rotation Sensing with Depolarization and Diattenuation

Finally, we calculate the QFI for the rotation angle vs the average photon number of the probe states considering both depolarization and diattenuation channels in forward and reverse decomposition channels. The results are shown in Fig. 4.6. We have only included the results for the weak depolarization case for each depolarization channel considered in Section 4.4.1 to see wether the quantum advantage present in this regime still persists after implementation of the new loss channel. The parameters of rotation are identical with the ones chosen in the previous subsection and diattenuation parameters are $q = r = 0.9$. The general behavior of the QFI with

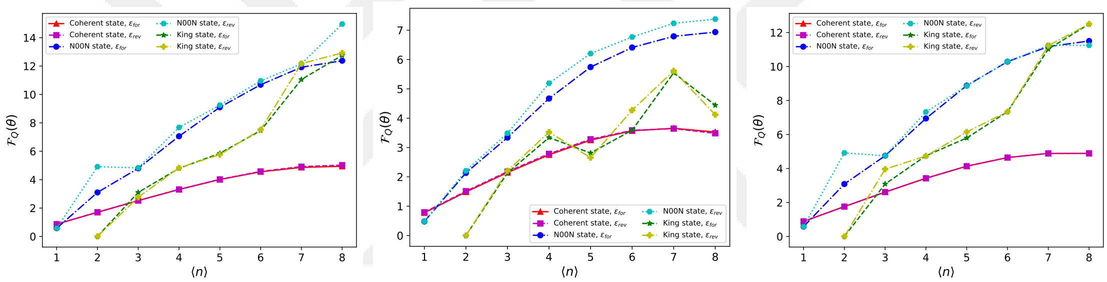

(a) (b) (c)

Figure 4.6: QFI for rotation angle in presence of depolarization and diattenuaion noise vs average photon number. Calculations are for coherent state in forward (solid line with triangular data points in red) and reverse (dashed line with square data points in magenta) processes, NOON state in forward (dash dotted line with circular data points in blue) and reverse (dotted line with triangular data points in cyan) processes and Kings of Quantumness in forward (dashed green line with star datapoints) and reverse (dash-dotted yellow line with plus shaped datapoints) processes for $q = r = 0.9$ and (a) isotropic depolarization with $\nu_i t = 0.003$ (b) anisotropic depolarization with $\nu_a t = 0.05$ (c) depolarization based on convex combination of rotations with $[\eta_{min}, \eta_{max}] = [-\pi/8, \pi/8]$, $\sigma_r = \pi/32$, $n_r = 6$.

the number of photons is similar to the case where diattenuation is not considered. However, as expected, for all cases it is evident that due to implementation of the diattenuation channel the QFI for each $\langle n\rangle$ shrinks even further. Comparing Fig. 4.6 with the results given in the previous subsection it is clear that the diattenuation channel diminishes the metrological power of the NOON state more than it does for Kings of Quantumness. Furthermore, the relative advantage of the NOON state in reverse decomposition as compared with the forward decomposition still remains after inclusion of diattenuation. From Fig. 4.6(a) and Fig. 4.6(c) it is clear that for larger photon numbers Kings of Quantumness surpass the NOON state in terms of precision and from Fig. 4.6(b) we see that for Kings of Quantumness at $\langle n\rangle = 5$ (which corresponds to a 1-anticoherent state) the QFI is smaller than that of the coherent state.

4.5 Experimental Implementation of NOON State Polarimetry

In addition to theoretical investigations [Belsley and Matthews, 2022], several recent experimental examples of applications of NOON states, for instance, for scattering-based probing of delicate samples like an atomic spin ensemble [Wolfgramm et al., 2013b] and highly sensitive measurement of protein concentration via the refractive index change [Peng and Zhao, 2023], support the motivation of our study. Aiming at experimental validation of the theoretical findings described in the previous sections and at testing the feasibility to enhance the polarimetric sensing accuracy in presence of depolarization and diattenuation channels, we conceive a series of measurements. Here, we follow the previous works on realization and characterization of the two-photon and higher-order NOON states [Yurke et al., 1986, Kuzmich and Mandel, 1998, Sanaka et al., 2004, Israel et al., 2012, Israel et al., 2014b].

Experimentally a NOON state can be both prepared and detected by exploiting the Hong-Ou-Mandel (HOM) effect [Hong et al., 1987]. Alternatively, in case of a two-photon NOON state, the preparation can be realized by the spontaneous parametric down-conversion (SPDC) process. Under conditions of type-II phase matching, a correlated pair of the vertically (V) and horizontally (H) polarized photons $|HV\rangle|HV\rangle$ is generated by SPDC. This state can be regarded as a NOON state of the form $i/\sqrt{2}(|2_L, 0_R\rangle + |2_R, 0_L\rangle)$, where L and R stand for the left- and right-circular polarizations, respectively [Adamson et al., 2007, Wolfgramm et al., 2010]. The projection of this state to the (H,V) basis can be obtained by a quarter-wave plate (QWP), oriented with its fast axis at 45° to the incoming polarization orientations. Such a strategy is followed in Fig 4.7, where a possible optical arrangement for test experiments is represented.

After the two-photon NOON state is prepared, it is split by a polarizing beam splitter into two paths. One of them is regarded as reference channel, and the other is used for introducing the object under study. The two beams are then merged with a non-polarizing beam splitter. At both outputs of the latter a polarization state analyzer consisting of a QWP and a linear polarizer (LP) is implemented to perform projective measurements with the help of single photon detectors. The coincidences between the two channels for state reconstruction via the quantum state tomography [James et al., 2001, Adamson et al., 2007] or HOM interference visibility measurements are counted with the time tagging device.

In order to check the feasibility of the method for practical applications like for the already mentioned eye retina diagnostics, first technical samples of controllable thickness and retardance should be used. For the first case, a possible option would be a series of transparent homogeneous thin films of different thicknesses. For the second case, the retardance estimation under minimal impacts of diattenuation and depolarization, fixed (QWP, half-wave plate) and variable (Soleil-Babinet compensator) retarders at different orientations (angle α) of their optical axis can be used. It is expected that successful demonstration of such experiments with technical samples could be later directly translated for method feasibility checks with biological specimen probing.

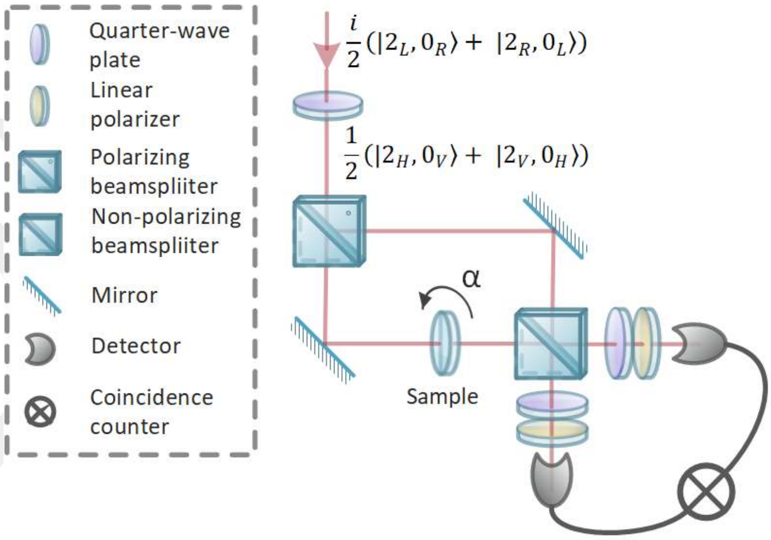

Figure 4.7: A possible optical arrangement for test experiments on polarimetric accuracy enhancement with NOON states. A state $i/\sqrt{2}(|2_L, 0_R\rangle + |2_R, 0_L\rangle)$ is generated within an SPDC event of type-II phase matching (not depicted). This state is translated into $1/\sqrt{2}(|2_H, 0_V\rangle + |0_V, 2_H\rangle)$ by a quarter-wave plate and enters a Mach-Zehnder interferometer with a sample in one of the channels. The Hong-Ou-Mandel interference at the last non-polarizing beamsplitter takes place. Coincidence counts between the two outputs of the beamsplitter are measured.

Chapter 5

ENVIRONMENT-ASSISTED MODULATION OF HEAT FLUX IN A BIO-INSPIRED SYSTEM BASED ON COLLISION MODEL

5.1 Introduction: Photosynthetic Energy Transport and Quantum Mechanics

Photosynthesis is the natural photochemical process of converting the energy of light into chemical energy, which can be used by an organism itself. Most plants, algae, and cyanobacteria are known to perform photosynthesis. Since its discovery almost three centuries ago, it has been a topic of continuous research. In the initial stage of this process, the energy from light is absorbed by the light harvesting antenna complex (a network of chromophores), and the excitation energy is transferred to the reaction center. Antenna complexes are very diverse in their structure, and we can classify the photosynthetic organisms based on the structure of their antennas. One of the remarkable features of photosynthesis, which also has attracted the attention of the physics community, is its high energy transfer efficiency during this stage [Blankenship, 2014].

There has been many theoretical and experimental attempts to uncover the underlying physical mechanism responsible for such an efficient energy transfer in the biological light harvesting systems. Specifically, the role of quantum mechanics in excitation energy transfer has been a topic of active debate within the scientific community. The subject of considerable fraction of these studies is the Fenna-Matthews-Olson (FMO) complex, which is a pigment-protein complex found in green sulfur bacteria and is responsible for funneling the exciton energy collected by the chlorosome antenna to the reaction center.

One of the processes using which the photosynthetic light harvesting systems are thought to transfer the solar energy is called electronic (or excitation) energy transfer (EET), resonance energy transfer (RET), fluorescence resonance energy transfer, or Förster resonance energy transfer (FRET). In this process the photoexcitation induces an oscillating dipole in the excited (donor) molecule. A molecule nearby (acceptor) can feel the oscillating electric field associated with the donor molecule's oscillating dipole, which in turn induces a dipole in the acceptor molecule. Once the donor molecule relaxes to its ground state, the excess energy gets transferred to the acceptor incoherently via emission of a virtual photon. In short, the FRET theory is the application of the Fermi Golden rule to the molecular systems in which the donor is in its excited state and the acceptor in its ground state. The earliest experimental observations of this process were done in 1922 by Frank et al. and Carlo [Franck, 1922, Carlo, 1922, Cario and Franck, 1922]. The role of dipole-dipole interactions in this form of energy transfer was first put forward by F. Perrin and J. Perrin [Perrin, 1927, Perrin, 1932]. In his seminal work, Förster found that the energy transfer through this nonradiative dipole-dipole coupling depends on spectral overlap and intermolecular distance of the molecules [Förster, 1946, Förster, 1948, Förster, 1959, Şener et al.,]. An early example of Föster's theory in light harvesting systems is the study on electronic excitation transfer of photosynthetic purple bacteria by Duysens in 1951 [Duysens, 1951].

It is worth mentioning that Förster's theory doesn't give an accurate description of the energy transfer process when the chromophores are packed tightly and are very close to each other, because in this case the inter-chromophore coupling becomes strong and the inter-chromophore orbital overlap is no longer negligible. Under these conditions the excitation is delocalized (shared) between the molecules. The methodology used in the theoretical simulation of photosynthetic energy transfer depends on the strength of inter-chromophore interactions and chromophore-environment interaction. In the cases where the inter-chromophore coupling is weak (strong) compared with the chromophore-environment coupling, the excitation transfer dynamics is well described by Förster (Redfield) theory [YAN, 2002, Ishizaki and Fleming, 2009a] in which the energy spread is incoherent (coherent). For the intermediate coupling regime, the interplay between coherent and incoherent energy transform modes becomes highly nontrivial. Several theoretical approaches, including modified Redfield theory, generalized Markovian master equation, hierarchical equations of motion and other methods have been used to model the energy transfer in the intermediate coupling regime [Kenkre and Knox, 1974, Leegwater, 1996, Kakitani et al., 1999, Kimura et al., 2000, Ishizaki and Fleming, 2009b, Kimura and Kakitani, 2007, Kimura, 2009, Jang, 2011, Jang, 2009, Hossein-Nejad et al., 2012].

One of the earliest theoretical studies on the coherent energy transfer contribution in photosynthetic complexes was carried out by Leegwater using a phenomenological model to distinguish between the coherent and incoherent dynamics [Leegwater, 1996]. Subsequently, Schulten et al. suggested that coherence increases the FRET rates in light harvesting purple bacterias by causing a spectral shift and improving resonance between the bacteriochlorophyll (BChl) clusters [Hu et al., 1997]. In the following years quantum coherence contributions in photosynthetic energy transfer became a topic of considerable interest within quantum physics and quantum chemistry community, a trend that continues to this day. A significant body of scientific work investigate the possibility of quantum coherence at the physiological conditions and link between the coherence in light harvesting complexes and their energy transfer efficiency.

Comprehensive critical reviews on energy transfer in these complexes and possible coherence effects in photosynthesis are available in the literature [Chenu and Scholes, 2015, Curutchet and Mennucci, 2017, MAN, 2020, TAO, 2020]. Experimental studies by Savikhin et al. [SAV, 1997] on the FMO complex using fluorescence anisotropy claimed the existence of quantum beating in its exciton levels. Later, using two-dimensional time-resolved spectroscopy experiments, Fleming et al. reported the existence of long-lived oscillatory patterns at cryogenic temperatures in FMO [Engel et al., 2007] and LH2 [Calhoun et al., 2009] complexes which were attributed to the dynamic electronic coherence in these structures. In the subsequent experimental works it was argued that the dynamical effects of coherence also manifest in room temperature and might play a role in the energy transfer process [Collini et al., 2010, Panitchayangkoon et al., 2010, Panitchayangkoon et al., 2011]. Particularly, Engel's work [Engel et al., 2007] attracted the attention of the quantum information community because it was claimed that using this coherence, the photosynthetic organism might perform a Grover search algorithm in order to find the optimal pathway for energy transfer. This work caused a paradigm shift in the study of energy transport in the light harvesting complexes and a significant number of papers that have been published ever since, focus on studying dynamical coherence in several models and making connections between coherence and spatial domain energy transfer. Several mechanisms have been proposed to explain how quantum coherence alone or coherent dynamics alongside with environmental noise, aids the light harvesting complex in energy transfer [Mohseni et al., 2008, Rebentrost et al., 2009, Plenio and Huelga, 2008, Olaya-Castro et al., 2008].

In recent years, several theoretical and experimental works have been published which dispute the significance of the coherent energy transport in biological light harvesting complexes [Duan et al., 2017, Harush and Dubi, 2021, Wilkins and Dattani, 2015, Kassal et al., 2013, Cao et al., 2020]. In the light of these developments, environmental noise tunes the spectral properties of the biological light harvesting complex, which can be thought of as an enhanced thermalization device, in a way to boost its transport efficiency. This phenomena is typically called noise assisted transport (NAT) or environment assisted quantum transport (ENAQT). In recent years an experimental verification of the constructive role of the environmental noise on the energy transport properties of light harvesting complexes, based on superconducting qubits is demonstrated by Potočnik et al. [Potočnik et al., 2018]. In this work the energy transport properties a network of 3 superconducting qubits, which simulate the chromophores chlorophyll molecules, is studied upon excitation with both coherent and incoherent light. It is found that introducing noise to system can have positive effect on the energy transmission.

These studies are of great importance because understanding the physical mechanism responsible for biological photosynthetic light harvesting systems and their limitations might lead the way in order to design biomimetic devices with comparable or even greater efficiency than their biological counterparts. Bio-inspired designs based on photosynthetic complexes have proven to be promising and efficient and are currently a subject of an active and diverse research effort encompassing quantum optics [Kozyrev, 2019, Mattiotti et al., 2021], quantum thermodynamics [Scully et al., 2011, Killoran et al., 2015, Chen et al., 2017], and energy transport and conversion [Ringsmuth et al., 2012, Sarovar and Whaley, 2013, Romero et al., 2017, Rupp and Gruber, 2019].

In the past decade, quantum collision models, a.k.a repeated interaction schemes, have gained popularity in order to model open quantum system dynamics [Scarani et al., 2002, Ciccarello, , Ciccarello et al., 2013, Lorenzo et al., 2017b, Lorenzo et al., 2017a, CIC, 2022, Arısoy et al., 2019, Çakmak et al., 2017, Çakmak et al., 2019, Campbell et al., 2019]. In collision models, the bath is modeled as a collection of identical ancillae with which an open system interacts one at a time. Collision models can simulate any Markovian open system dynamics [Cattaneo et al., 2021] but they are also particularly insightful for studies on non-Markovian open system dynamics and open quantum systems with correlations between system and environment. Recently, there have been attempts to utilize the repeated interaction scheme to study the transport phenomena in light harvesting complexes. Chisholm et al., using a stochastic collision model, studied the transport phenomena in a quantum network model of the FMO complex, investigating the Markovian and non-Markovian effects [Chisholm et al., 2021]. Gallina et al. have simulated the dephasing assisted transport of a four-site network based on a collision model using the IBM Qiskit QASM simulator [Gallina et al., 2022].

Inspired by the experimental setup given in [Potočnik et al., 2018] for simulating the energy transport in biological light harvesting complexes using superconducting qubits, we use a quantum collision model to investigate the heat transport in a similar network of qubits whose role is to transfer energy from a hot bath to a cold bath. The goal is to study the effect of interaction between the system and a hierarchically structured environment (HSE), on the steady state heat flux. Collision models have proven to be effective in thermodynamic analysis of a network of qubits between two thermal baths [Tian et al., 2021], a qubit coupled to a structured environment [Li and Li, 2021] and a system of qubits interacting with a thermal and a coherent thermal bath [Yu et al., 2021]. Also, coupling with an HSE is shown to have a profound effect on coherent exciton transfer [Levi et al., 2016]. However, to the best of our knowledge modulation of heat flow between two thermal baths using an auxiliary HSE has not been investigated. Such an auxiliary HSE in a natural system could be envisioned as a background matrix molecules supporting a system of energy transfer molecules. Therefore our work utilizes the concepts and methods of the mentioned works to explore the thermodynamic behavior of an open quantum system in a complex environment.

The remainder of this work is organized as follows. In section 5.2 we describe the components of our model, namely the system, the HSE, the heat baths and their interaction. Next, we describe the repeated interaction framework and quantify the heat flux. In section 5.3 first we show the effect of the system-environment and inter-environment interactions on enhancement of the transient and steady-state heat flux and provide with a possible explanation for this behavior. We then continue to analyze the effect of coherence in the HSE on the steady-state heat flux.

5.2 The Collision Model

We consider a system made out of three qubits, namely S_1, S_2 and S_3, arranged on a line. S_1 and S_3 interact with a set of ancillary qubits representing the hot and cold thermal baths (temperatures T_h and T_c), respectively, which we refer as R_n^h and R_n^c. Each system qubit interacts with its nearest neighbor, In addition, we have a HSE, which is composed of a qubit A, with which S_2 directly interacts, and a set of ancillary qubits B_n interacting with qubit A. Our main goal is to study the effect of the HSE interacting locally with S_2, and also the effect of the coherence in B_n qubits, on energy transfer from the hot bath to the cold bath. We setup our model in the described fashion in order to mimic a similar model considered in [Potočnik et al., 2018], which presents an experimental investigation of the light harvesting complexes. A schematic representation of our model is given in Fig. 5.1.

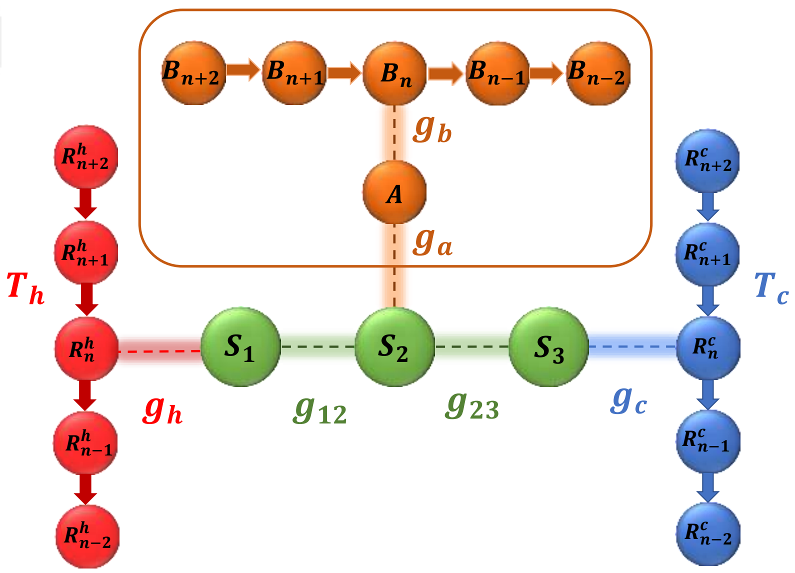

Figure 5.1: A schematic representation of the model. The system qubits, denoted by S_1, S_2 and S_3, are interacting with each other and the qubits from the cold bath, hot bath and the hierarchical environment.

The initial states of the hot bath qubits are taken to be the thermal state of their Hamiltonian at temperature T_h, while the initial states of the system qubits, qubit A and the cold bath qubits are assumed to be the thermal states of their corresponding free Hamiltonian at temperature T_c. The initial state for qubits B_n is taken to be

$$\rho_B = p\,|\psi\rangle\,\langle\psi| + (1-p)\rho_B^{th} \tag{5.1}$$

where $p \in [0,1]$ and ρ_B^{th} is the thermal state of the qubit at temperature T_c. The state $|\psi\rangle$ is defined as

$$|\psi\rangle = \frac{1}{Z_e}(e^{-\frac{1}{4}\omega_e\beta_c}\,|0\rangle + e^{\frac{1}{4}\omega_e\beta_c}\,|1\rangle), \tag{5.2}$$

where $Z_e = \mathrm{Tr}[exp(-\beta_c\hat{H}_e^0)]$ is the partition function and β_c is the inverse temperature. The form of density matrix given by Equation (5.1) assures that the diagonal elements of ρ_B and ρ_B^{th} are identical but the diagonals are non-zero for $p \neq 0$. Hence, p is the parameter which controls the amount of coherence in the HSE. The free Hamiltonians for the qubits are all of the form $\hat{H}_i^0 = \omega_i/2\hat{\sigma}_z^i$ for $i = 1,2,3,h,c,e$ in which ω_i and $\hat{\sigma}_z^i$ are the corresponding transition frequencies and Pauli z operators. The system Hamiltonian is given by the sum of free and interaction Hamiltonians of the system qubits as

$$\hat{H}_{\text{sys}} = H_{\text{sys}}^0 + H_{\text{sys}}^I = \sum_i \frac{\omega_i}{2}\hat{\sigma}_z^i + \sum_{i<j} g_{ij}(\hat{\sigma}_+^i\hat{\sigma}_-^j + \hat{\sigma}_-^i\hat{\sigma}_+^j), \tag{5.3}$$

in which $\hat{\sigma}_+$ and $\hat{\sigma}_-$ are the raising and lowering operators. We model the the interaction Hamiltonian between the system and both thermal baths as an energy preserving dipole-dipole interaction

$$\hat{H}_h^I = g_h(\hat{\sigma}_+^1\hat{\sigma}_-^h + \hat{\sigma}_-^1\hat{\sigma}_+^h) \tag{5.4}$$

$$\hat{H}_c^I = g_c(\hat{\sigma}_+^3\hat{\sigma}_-^c + \hat{\sigma}_-^3\hat{\sigma}_+^c). \tag{5.5}$$

The interaction between qubits A and S_2 is described by a purely dephasing interaction given in the following form

$$\hat{H}_{SA}^I = g_a\hat{\sigma}_z^2\hat{\sigma}_z^A. \tag{5.6}$$

We particularly consider a different interaction Hamiltonian at this stage. The reason behind this is to make sure that we do not inject coherence into the system qubits. As stated earlier, our aim is to investigate the effect of the coherence contained in the HSE. Finally, the interaction Hamiltonian between the qubits that belong in HSE is also chosen to be a dipole-dipole interaction

$$\hat{H}^{I}_{AB} = g_b(\hat{\sigma}^{A}_{+}\hat{\sigma}^{B}_{-} + \hat{\sigma}^{B}_{-}\hat{\sigma}^{A}_{+}) \tag{5.7}$$

Considering all the interaction times of collisions to be equal to $t_c = 0.01$, using $U_i = exp(-iH^{I}_{i}t_c/\hbar)$ we can calculate the corresponding time evolution operator for each Hamiltonian interaction. As a standard procedure in collision models, each collision is described by brief unitary couplings between the elements of the model. Therefore, we consider gt_c to be smaller than 1. The repeated interaction scheme we considered is made out of the following steps:

1. R^{h}_{n} interacts with S_1
2. S_1 interacts with S_2
3. S_2 interacts with A
4. A interacts with B_n
5. S_2 interacts with S_3
6. S_3 interacts with R^{c}_{n}

After each set of collisions, the qubits for the hot bath R^{h}_{n}, cold bath R^{c}_{n} and B_n are traced out and are replaced with fresh ones, R^{h}_{n+1}, R^{c}_{n+1} and B_{n+1}, in their corresponding initial states. We emphasize that qubit A is not reset to its initial state; it plays a role as an interface between a larger background (B_n qubits) and the qubits forming the energy transport medium (S_1, S_2, S_3). It is important to note that the qubits A and B_n qubits form an HSE to the transport medium qubits. Our collision model reflects a hierarchical coupling between the transport system and this auxiliary environment. Based on this scheme, the thermal energy transferred to the cold bath from the system at each collision step n can be written as

$$\Delta Q_n = Tr[\hat{H}_c(\tilde{\rho}_c^n - \rho_c^n)], \tag{5.8}$$

in which ρ_c^n and $\tilde{\rho}_c^n$ are the density matrices for the cold bath qubit before and after the collision, respectively. Based on this definition, the heat current can be defined as

$$J_n := \frac{\Delta Q_n}{t_c} = \frac{1}{t_c} Tr[\hat{H}_c(\tilde{\rho}_c^n - \rho_c^n)]. \tag{5.9}$$

These sets of collisions repeat until the energy transport per collision reaches a steady state. Hence, the steady state heat flux becomes

$$J_{ss} = \lim_{n\to\infty} \frac{1}{t_c} Tr[\hat{H}_c(\tilde{\rho}_c^n - \rho_c^n)]. \tag{5.10}$$

5.3 Results

In this section, we study the effects of g_a, g_b and p, on the heat flux transported to the cold bath. We assume each qubit has the same transition frequency ω_0 and use as our time-energy scaling parameter so that we use scaled and dimensionless parameters, where $\omega_0 = 1$. In all our calculations, the system–bath interaction couplings are taken to be $g_c = g_h = 7.5$ and the collision time is $t_c = 0.01$.

5.3.1 *Effect of the System-HSE and Inter-HSE Couplings*

Using the framework laid out in Section 5.2 we can quantify the amount of energy transferred from the hot bath to the cold bath with and without the system–HSE interaction. For the network of qubits demonstrated in Fig. 5.1, the results are shown in Fig. 5.2. It is evident from Figure Fig. 5.2 that coupling with HSE enhances transient and steady-state heat transfer in both of the coupling regimes that is considered. A qualitative reason for one of the mechanisms responsible for this behavior can be given based on the energy level diagram of the system Hamiltonian, as given in Fig. 5.3.

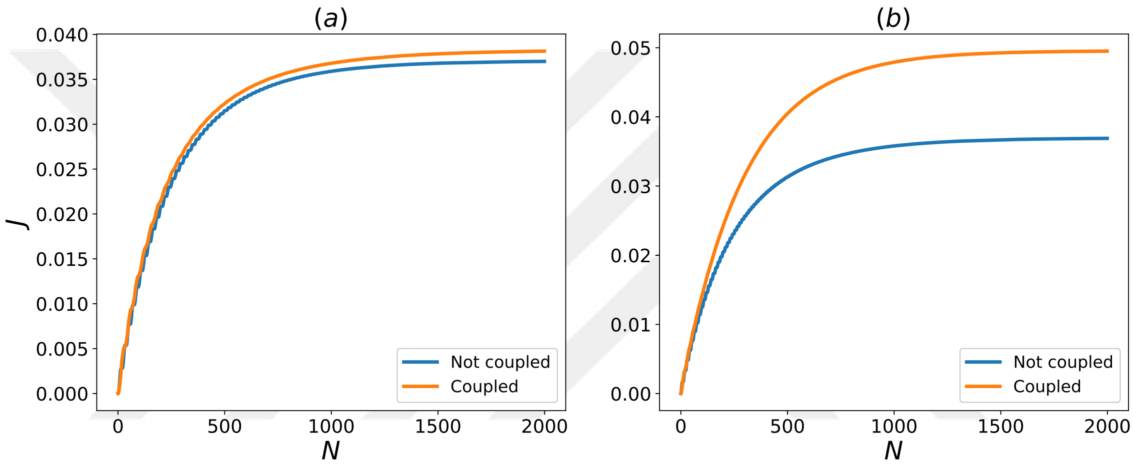

Figure 5.2: Heat flux to the cold bath, J, with and without interaction with the HSE for different coupling constants. The HSE are assumed to be in thermal state ($p = 0$) and for blue curves we have $g_a = 0$. The remaining couplings are (**a**) $g_{12} = 30$, $g_{23} = 15$ and for the orange curve $g_a = 20$, $g_b = 40$ (**b**) $g_{12} = 50$, $g_{23} = 25$ and for the orange curve $g_a = 40$, $g_b = 30$.

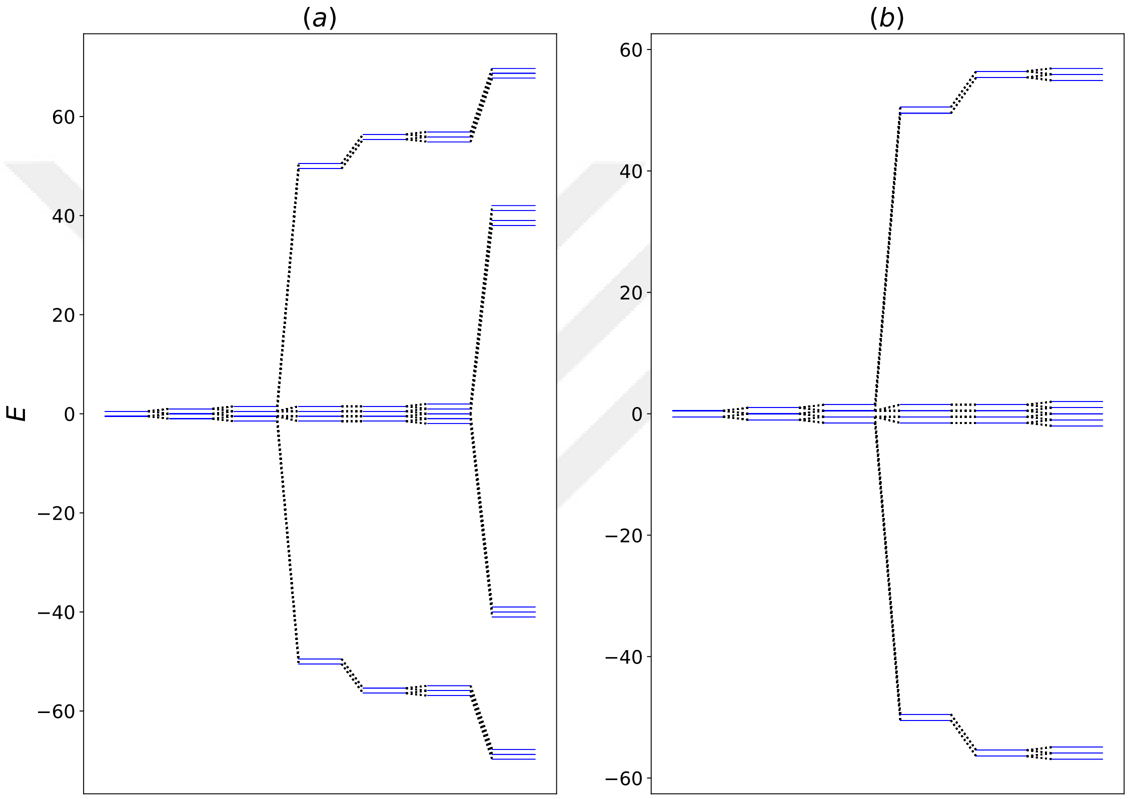

Figure 5.3: Energy level diagram for the system with and without interaction with the HSE. The interaction couplings of the system are $g_{12} = 50$ and $g_{23} = 20$. The system-HSE interaction is (**a**) $g_a = 40$ (**b**) $g_a = 0$.

From Fig. 5.3, we can observe that the interaction between system and the HSE modulates the energy levels of the system. The changes in the energy levels decreases the transition energy between certain eigenstates, which, therefore, makes these transitions more accessible to the hot thermal bath. As a result, the net thermal energy transfer increases upon interacting with the HSE. It is worth mentioning that due to the form of the interaction Hamiltonian H_{SA}^{I} given in Equation (5.6), there is no energy transfer between qubits A and S_2, and the system qubits only transport the energy between the hot and the cold bath. In Figure 5.4 the steady-state heat flux as a function of g_a and g_b is shown when the B_n qubits are fully thermal.

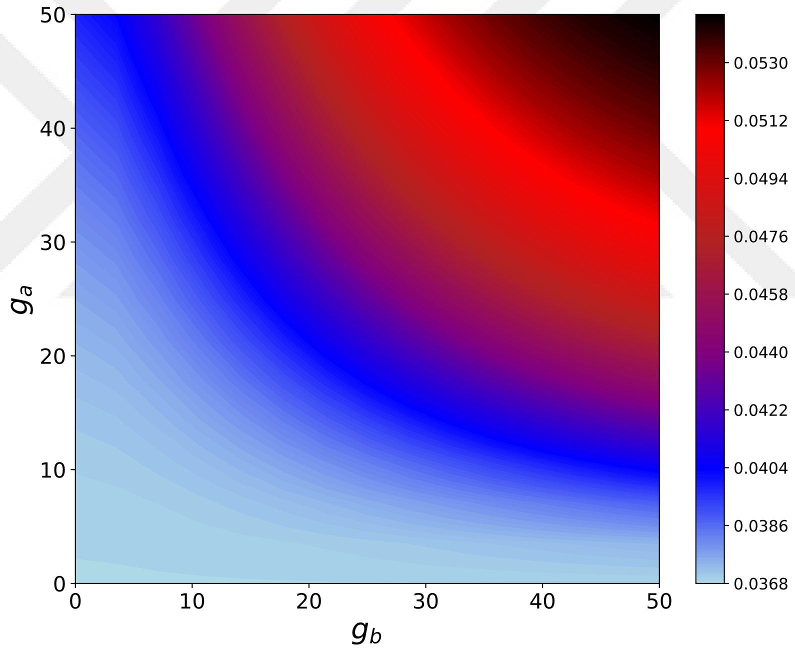

Figure 5.4: Contour plots for the steady state heat flux J_{ss} vs. system-HSE and inter-HSE couplings g_a and g_b considering no coherence in HSE ($p = 0$). The inter-system couplings are $g_{12} = 50$ and $g_{23} = 25$.

An increase in g_a and g_b overall, results in an enhancement of J_{ss}. However, for a fixed g_a (g_b), this enhancement is more pronounced for larger values of g_a (g_b). Therefore, we see that coupling with the HSE has a positive effect on the steady-state heat current, regardless of the initial coherence of the HSE qubits.

5.3.2 Effect of Coherence within the HSE

Presently, we turn our attention to the effect of coherence within HSE on the steady-state heat transfer. For this aim, in Fig. 5.5, we present the dependence of J_{ss} to different values of p and g_a.

The results indicate that there is a negligible change in J_{ss} for increased values of coherence, especially for a smaller g_a. However, for larger values of g_a, it is clear that there is a noteworthy enhancement of J_{ss} for a larger g_b, as indicated in Fig. 5.5b, and a considerable non-monotonic change in J_{ss} for a smaller g_b, as shown in Fig. 5.5a.

In Fig. 5.6, the values of J_{ss} by changes in the coherence parameter p and g_b is shown. There is a limited gain in J_{ss} for an increased p, especially for smaller values of g_b. This gain is more significant for larger values of g_b. As the comparison between Fig. 5.6a,b indicates, this effect is more pronounced for a larger g_a coupling.

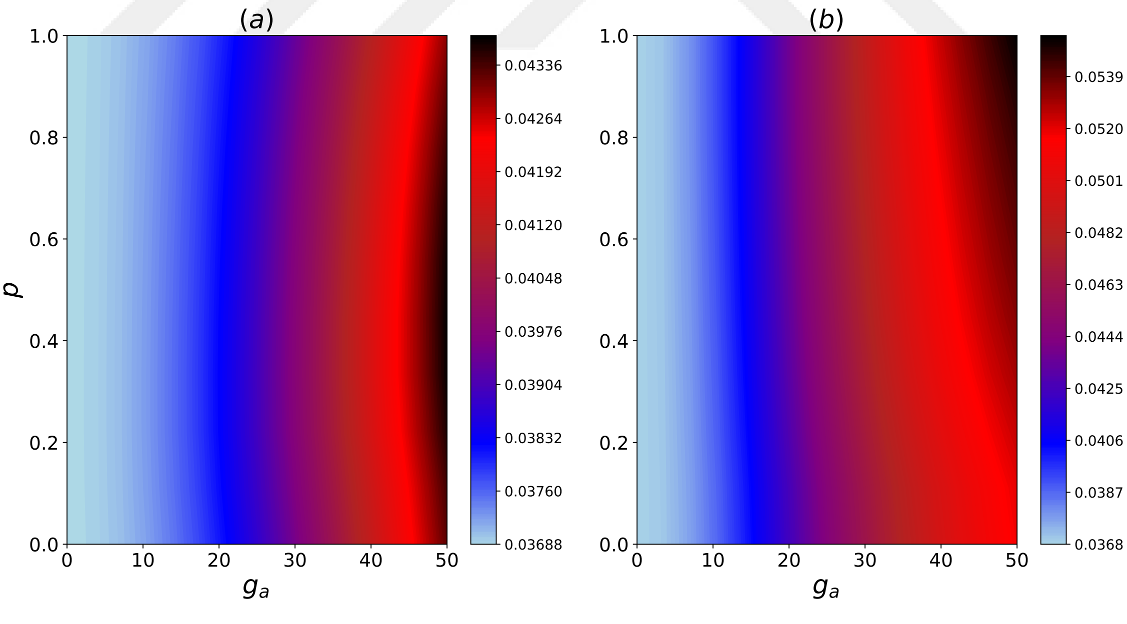

Figure 5.5: Contour plots for the steady state heat flux, J_{ss} vs. system-HSE coupling, g_a, and coherence in the HSE, p. The couplings are (**a**) $g_{12} = 50$, $g_{23} = 25$, $g_b = 10$ (**b**) $g_{12} = 50$, $g_{23} = 25$, $g_b = 30$.

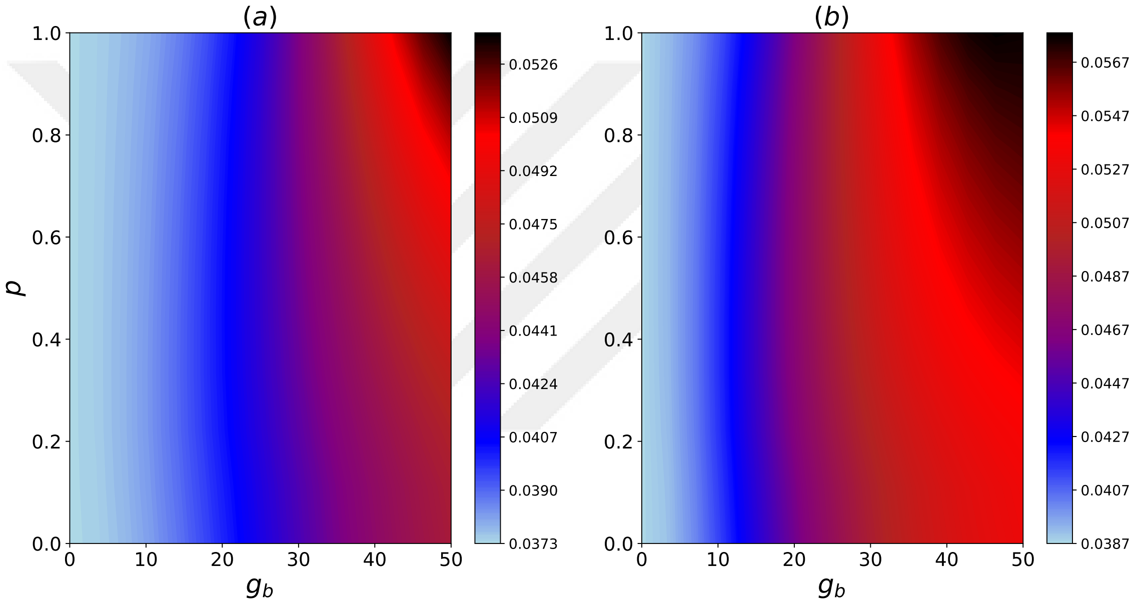

Figure 5.6: Contour plots for the steady state heat flux, J_{ss}, vs inter-HSE coupling, g_b, and coherence in the HSE, p. The couplings are (**a**) $g_{12} = 50$, $g_{23} = 25$, $g_a = 20$ (**b**) $g_{12} = 50$, $g_{23} = 25$, $g_a = 40$.

Chapter 6

A QUANTUM OTTO ENGINE WITH SHORTCUTS TO THERMALIZATION AND ADIABATICITY

6.1 Introduction: Quantum Heat Engines and Their Counterdiabatic Control

Enhancing the performance of heat engines has been a long-standing objective in the field of thermodynamic cycle investigations. The pinnacle of these endeavors is reflected in Carnot's second law of thermodynamics, which establishes an upper limit on the efficiency of heat engines [Carnot et al.,]. This limit can, in principle, be attained through a Carnot cycle, comprising reversible processes. However, while the Carnot engine achieves this limit, it is unable to generate any power due to the quasi-static nature of its processes. Practical heat engine cycles such as Otto, Diesel, or Stirling face the challenge of balancing efficiency and power, necessitating real-world engines to complete a cycle within a finite time, albeit with lower efficiency. Of particular significance is the efficiency at maximum power, which was studied by Curzon and Ahlborn in their seminal paper [Curzon and Ahlborn, 1975].
Currently, there is ongoing research in quantum heat engines and refrigerators [Kosloff and Levy, 2014, Kosloff and Rezek, 2017, Tuncer and Müstecaplıoğlu, 2020, Kurizki and Kofman, 2022, Deffner and Campbell, 2019]. Since the pioneering work by Scovil and Schulz-DuBois [Scovil and Schulz-DuBois, 1959], quantum heat engines have been extensively studied theoretically [Alicki, 1979, Kosloff, 1984, Geva and Kosloff, 1992, Geva and Kosloff, 1996, Feldmann et al., 1996, Scully, 2002, Humphrey et al., 2002, Scully et al., 2003, Feldmann and Kosloff, 2003, Kieu, 2004, Feldmann and Kosloff, 2004, Quan et al., 2005, Rezek and Kosloff, 2006, Quan et al., 2007, Allahverdyan et al., 2008, Abah et al., 2012, Gelbwaser-Klimovsky and Kur-

izki, 2014, Hardal and Müstecaplıoğlu, 2015, Newman et al., 2017, Turkpence et al., 2017, Agarwalla et al., 2017, Hardal et al., 2017, Niedenzu et al., 2018, Insinga et al., 2018, Naseem and Özgür E. Müstecaplıoğlu, 2019, Köse et al., 2019, Singh and Müstecaplıoğlu, 2020, Raja et al., 2021, B.S et al., 2022, Pozas-Kerstjens et al., 2018, Li et al., 2022], and successful experimental demonstrations have been recently reported [Zou et al., 2017, Klatzow et al., 2019, Peterson et al., 2019, Bouton et al., 2021, Sheng et al., 2021, Lisboa et al., 2022, Zhang et al., 2022a, Reyes-Ayala et al., 2023]. Despite these theoretical and experimental developments, it is still an open question whether the quantum advantage can lead to Carnot efficiency or better at finite power [Roßnagel et al., 2014, Campisi and Fazio, 2016, Kim et al., 2022]. It is, therefore, crucial to study the potential and limitations of quantum thermal devices and investigate methods to boost their finite-time performance.

A specific type of control techniques which are collectively known as shortcuts to adiabaticity (STA) have gained a particular interest in the study of quantum heat engines. The central idea in STA is to design protocols to drive the system by emulating its adiabatic dynamics in finite time [Torrontegui et al., 2013, Guéry-Odelin et al., 2019]. Since its foundation [Demirplak and Rice, 2003, Demirplak and Rice, 2005, Berry, 2009, Chen et al., 2010] different approaches have been developed to engineer STA, such as using dynamical invariants, [Chen et al., 2010, Chen et al., 2011], inversion of scaling laws [del Campo, 2011, Campo and Boshier, 2012] and the fast-forward technique [Masuda and Nakamura, 2010, Masuda and Nakamura, 2011, Torrontegui et al., 2012]. In recent years, successful experimental realizations of STA have been reported in the literature [Vepsäläinen et al., 2019, Vepsäläinen and Paraoanu, 2020, Zhou et al., 2020, Yin et al., 2022].

STA has been extensively explored as a means to enhance the performance of quantum refrigerators [Funo et al., 2019, Abah et al., 2020] and boost the power output of QHO [Campo et al., 2014, Abah and Lutz, 2018, Abah and Paternostro, 2019, Beau et al., 2016] and spin chain [Çakmak and Müstecaplıoğlu, 2019, Hartmann et al., 2020, Çakmak, 2021] based quantum heat engines by emulating adiabatic strokes within finite time frames. Previous studies in these domains have commonly assumed a rapid thermalization step. However, with the growing interest in the application of STA to open quantum systems, recent research has increasingly focused on the possibility of achieving swift thermalization using various techniques [Dann et al., 2018, Dann et al., 2019, Villazon et al., 2019, Alipour et al., 2020, Dupays et al., 2020, Pancotti et al., 2020, Suri et al., 2018, Dann and Kosloff, 2020]. These approaches are often referred to as fast thermalization, shortcuts to thermalization (STT) or shortcuts to equilibrium (STE). Since quantum heat engines contain thermalization branches, study of these techniques is of paramount importance in order to optimize the power and efficiency of these devices [Villazon et al., 2019, Pancotti et al., 2020, Suri et al., 2018, Dann and Kosloff, 2020, del Campo et al., 2018].

Motivated by these advancements, we conduct an analysis of the energy dynamics, power output, and efficiency characteristics of an Otto cycle utilizing a QHO as its working medium within a finite time frame. To achieve this, we employ shortcuts to adiabaticity (STA) during the expansion and compression strokes, while implementing STE during the hot isochoric strokes, resulting in what we refer to as an STÆ engine. In our investigation, we compare the thermodynamic performance metrics of this engine with an uncontrolled non-adiabatic quantum Otto (UNA engine) and a quantum Otto engine in which only the adiabatic strokes are accelerated using CD-driving (STA engine).

For a comprehensive evaluation of the thermodynamic performance within controlled dynamics, it is essential to meticulously account for the energetic expenses associated with the implementation of the control protocols [Çakmak and Müstecaplıoğlu, 2019, Abah and Lutz, 2018, Abah and Paternostro, 2019, Hartmann et al., 2020]. In this regard, we adopt a widely employed cost measure to quantify the energetic requirements of the STA protocol during the adiabatic strokes. Additionally, we introduce a novel cost measure based on the dissipative work performed by the environment [Alipour et al., 2022] specifically for STE protocol. This approach allows for an accurate evaluation of energy-related aspects when both STA and STE protocols are implemented.

Initially, we conduct a thermodynamic analysis of the three engines (UNA, STA, and STÆ) by considering a single cycle following the preparation phase. Subsequently, we extend our examination to their respective limit cycles. Our findings clearly demonstrate that the STÆ engine, incorporating both shortcuts to adiabaticity (STA) and shortcuts to equilibrium (STE) protocols, attains superior power output and efficiency when compared to the STA-only engine and the UNA engine.

This manuscript is organised as follows. In Section 6.2 we briefly introduce the quantum Otto cycle. In Section 6.3 the scheme for STA using counterdiabatic driving is introduced. In Section 6.4 the protocol for the fast driving of the Otto cycle towards thermalization is introduced. In Section 6.5 we describe the quantum Otto engine for which both STA and STE is used and in Section 6.6 we present our results.

6.2 Quantum Harmonic Otto Cycle

We study a finite-time quantum Otto cycle and consider the working medium to be a harmonic oscillator with a time dependent frequency. The Hamiltonian for a QHO is

$$\hat{H}_0 = \hat{p}^2/2m + m\omega_t^2\hat{x}^2/2 \tag{6.1}$$

in which $\hat{x}$ and $\hat{p}$ are the position and momentum operators respectively and ω_t is the time-dependent frequency and m is the mass of the oscillator. As shown in Fig. 6.1, the cycle consists of the following strokes.

(1) Adiabatic compression ($1 \to 2$): Unitary evolution for a duration of τ_{12} while the frequency increases from ω_c to ω_h.

(2) Hot isochore ($2 \to 3$): Heat transfer from the hot bath to the system for a duration of τ_{23} as the system equilibrates with the bath at temperature T_h at fixed frequency.

(3) Adiabatic expansion ($3 \to 4$): Unitary evolution for a duration of τ_{34} while the frequency decreases from ω_h to ω_c.

(4) Cold isochore ($4 \to 1$): Heat transfer from the system to the cold bath for a duration of τ_{41} as the system equilibrates with the bath at temperature T_c at fixed frequency.

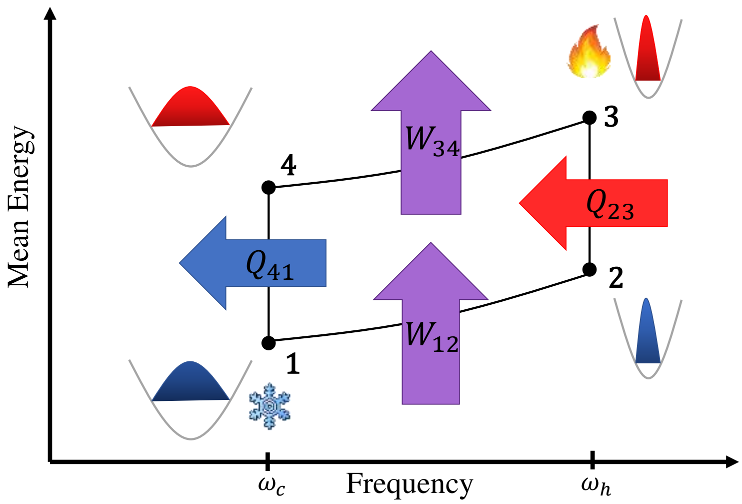

Figure 6.1: Schematic representation of a quantum Otto cycle composed of adiabatic compression ($1 \to 2$), isochoric hot thermalization ($2 \to 3$), adiabatic expansion ($3 \to 4$) and isochoric cold thermalization ($4 \to 1$) strokes.

During the adiabatic steps the system is decoupled from the heat baths, and the frequency is varied over time, at a rate bounded by the adiabatic theorem [Berry, 2009], so that the populations of the drifting energy levels remain unchanged. The resulting isentropic evolution is more restrictive than the classical adiabaticity condition of constant entropy. This is due to the fact that in a quantum adiabatic evolution, the adiabatic condition implies that the distribution of the populations must remain unchanged. However, in a classical adiabatic process the entropy is unchanged [Quan et al., 2007].

Mathematical formulations of the adiabatic time evolution for an isolated quantum system employ a time-scale separation between fast and slow degrees of freedom, yielding product states as solutions. For the compression and expansion strokes of the QHO Otto engine, this condition implies that the system will always remain in an instantaneous eigenstate of the time-dependent Hamiltonian. The unitary time evolution of such a process, which ideally takes infinite time, can be solved exactly and has zero entropy production. The average work and heat exchange values during the cycle is given by [Deffner and Lutz, 2008, Deffner et al., 2010],

$$\begin{aligned}
\langle W_{12}\rangle &= \frac{\hbar}{2}(\omega_h Q_{12}^* - \omega_c)\coth(\frac{\beta_c\hbar\omega_c}{2}) && (6.2)\\
\langle Q_{23}\rangle &= \frac{\hbar\omega_h}{2}\left[\coth(\frac{\beta_h\hbar\omega_h}{2}) - Q_{12}^*\coth(\frac{\beta_c\hbar\omega_c}{2})\right] && (6.3)\\
\langle W_{34}\rangle &= \frac{\hbar}{2}(\omega_c Q_{34}^* - \omega_h)\coth(\frac{\beta_h\hbar\omega_h}{2}) && (6.4)\\
\langle Q_{41}\rangle &= \frac{\hbar\omega_c}{2}\left[\coth(\frac{\beta_c\hbar\omega_c}{2}) - Q_{34}^*\coth(\frac{\beta_h\hbar\omega_h}{2})\right] && (6.5)
\end{aligned}$$

where W refers to the work input and Q refers to the heat input to the engine during the indicated strokes. β_c and β_h are the inverse temperatures for the cold and hot bath respectively. The terms Q_{12}^* and Q_{34}^* are the adiabaticity parameters and their values depend on the driving scheme [Abah and Lutz, 2018]. We are employing a sign convention in which all the incoming fluxes (heat and work) are taken to be positive [Singh et al., 2022, Singh and Müstecaplıoğlu, 2020].

In order to study the finite-time Otto cycle, we need to consider the time evolution along each stroke separately. The unitary evolution of the adiabatic strokes is governed by

$$\partial_t\hat{\rho} = -\frac{i}{\hbar}[\hat{H}_0, \hat{\rho}], \tag{6.6}$$

where $\hat{\rho}$ is the system's density matrix. For the duration of the isochoric strokes, a Markovian open system dynamics given by a Gorini–Kossakowski–Sudarshan–Lindblad

(GKLS) master equation governs the system's dynamics,

$$\partial_t \hat{\rho} = -\frac{i}{\hbar}[\hat{H}_0, \hat{\rho}] + \mathcal{D}(\hat{\rho}), \tag{6.7}$$

in which $\mathcal{D}(\hat{\rho})$ is the dissipation superoperator which must conform to Lindblad's form for a Markovian evolution

$$\mathcal{D}(\hat{\rho}) = k_{\uparrow}(\hat{a}^{\dagger}\hat{\rho}\hat{a} - \frac{1}{2}\{\hat{a}\hat{a}^{\dagger}, \hat{\rho}\}) + k_{\downarrow}(\hat{a}\hat{\rho}\hat{a}^{\dagger} - \frac{1}{2}\{\hat{a}^{\dagger}\hat{a}, \hat{\rho}\}). \tag{6.8}$$

The $k_{\uparrow}$ and $k_{\downarrow}$ are called heat conductance rates and the heat conductivity (heat transport rate) is defined as $\Gamma \equiv k_{\downarrow} - k_{\uparrow}$ [Kosloff and Rezek, 2017]. Note that, heat transport is not the only source of irreversibility in a quantum heat engine. Non-commutativity of the Hamiltonians at different times results in an additional dissipation channel, dubbed "quantum friction" [Kosloff and Feldmann, 2002].

Thermalization times are often neglected in the analyses of quantum heat engines, since they are assumed to be much shorter than the compression and expansion times. [Roßnagel et al., 2014, Abah and Lutz, 2018, Abah and Paternostro, 2019, Çakmak and Müstecaplıoğlu, 2019, Beau et al., 2016]. However, this assumption requires heat transport rates to be large, a circumstance for which it is shown that the optimal power production happens when the cycle times are vanishingly small [Feldmann et al., 1996, Rezek and Kosloff, 2006, Kosloff and Rezek, 2017].

Another line of reasoning to justify small thermalization times in the isochoric process is that, for the frequency to stay constant (hence, the Hamiltonian to be static), the duration of the system-bath interaction must be shorter than the duration of the isentropic process. Meanwhile, assuming that there exists a considerable energy exchange between the system and the bath or that the system equilibrates to the temperature of the bath, controlling the interaction time is equivalent to adjusting the system-bath coupling. However, a large system-bath coupling also implies a large heat transport rate. Additionally, in a thermalization map, which follows a GKLS type master equation, there is an implicit assumption that the thermalization time (which scales proportional to the inverse of the system-bath interaction energy), is longer than the relaxation dynamics of the bath and the unperturbed dynamics of the system [Alicki, 1979]. Therefore, for a realistic and consistent thermodynamic analysis of a quantum heat engine in its full generality, it is important to take into account the effect of thermalization times without imposing additional assumptions.

In order to see the effect of the duration of isochoric strokes, we take the total cycle time to be $\tau_{tot} = \tau_{12} + \tau_{23} + \tau_{34} + \tau_{41}$. We assume that $\tau_{adi} = \tau_{12} = \tau_{34}$ and $\tau_{iso} = \tau_{23} = \tau_{41}$. The engine power can be expressed as,

$$P = -\frac{\langle W_{12}\rangle + \langle W_{34}\rangle}{\tau_{\text{tot}}} \tag{6.9}$$

in which $\tau_{tot} = 2\tau_{adi} + 2\tau_{iso}$. For an ideal engine, efficiency becomes

$$\eta = -\frac{\langle W_{12}\rangle + \langle W_{34}\rangle}{\langle Q_{23}\rangle}. \tag{6.10}$$

Due to the fact that the ideal adiabatic and isochoric strokes are quasi-static, upon implementing a full cycle in finite time, the state the working medium of the engine doesn't precisely return to the initial state from which the cycle started. Therefore, for a complete study of a finite time quantum heat engine a limit cycle analysis has to be taken into account and the thermodynamic behavior of the engine in this mode of operation needs to be addressed [Kosloff and Rezek, 2017, Insinga et al., 2018, Feldmann and Kosloff, 2004].

Existence of a limit cycle for a quantum heat engine can be argued in very general terms. A general quantum process is described by a completely positive trace preserving (CPTP) map. The quantum channel for the entire cycle is a composition of four CPTP maps,

$$\varepsilon(\hat{\rho}) = \varepsilon_{4\to1} \circ \varepsilon_{3\to4} \circ \varepsilon_{2\to3} \circ \varepsilon_{1\to2}(\hat{\rho}) \tag{6.11}$$

which makes itself CPTP. Due to the Brouwer fixed-point theorem, every such channel should have at least one density operator fixed point ρ^* such that [Watrous, 2018]

$$\varepsilon(\hat{\rho}^*) = \hat{\rho}^*. \tag{6.12}$$

Lindblad showed that relative entropy (KL-divergence) between a state and a reference state is contractive under CPTP maps [Lindblad, 1975]. Later, Petz proved that a variety of metrics (including the Bures metric) are monotone (contractive) under CPTP maps [Petz, 1996]. These theorems can be expressed mathematically as

$$D_{\mathrm{KL}}(\varepsilon(\hat{\rho})||\varepsilon(\hat{\rho}_{\mathrm{ref}})) \leq D_{\mathrm{KL}}(\hat{\rho}||\hat{\rho}_{\mathrm{ref}}), \tag{6.13}$$

$$D(\varepsilon(\hat{\rho}), \varepsilon(\hat{\rho}_{\mathrm{ref}})) \leq D(\hat{\rho}, \hat{\rho}_{\mathrm{ref}}) \tag{6.14}$$

Here, D_{KL} is the relative entropy (which is not a metric but a divergence function) and D is a metric on the statistical manifold of the density operators. According to these theorems, the two states become less and less distinguishable upon successive application of the map ε. If the fixed point of the CPTP map is unique, the density operator will monotonically approach the steady-state via the dynamical map [Frigerio, 1977, Frigerio, 1978]. In this case, if we take $\hat{\rho}_{\mathrm{ref}} = \hat{\rho}^*$, Eq. (6.12) and Eq. (6.13) imply that upon successive application of the quantum channel, the system monotonically approaches the fixed point.

6.3 STA by CD-driving

In $1 \to 2$ and $3 \to 4$ the quantum system is isolated and work is performed by changing the frequency between ω_c and ω_h, which are fixed as design parameters. We now consider a counter-diabatic drive on the system by means of a control Hamiltonian added to $\hat{H}_0$, i.e.,

$$\hat{H}_{CD}(t) = \hat{H}_0(t) + \hat{H}_1(t) \tag{6.15}$$

such that the resulting dynamics given by

$$\partial_t \hat{\rho} = -\frac{i}{\hbar}[\hat{H}_{CD}, \hat{\rho}] \tag{6.16}$$

is identical to the adiabatic evolution under $\hat{H}_0$ alone. For a closed system, the general form of $\hat{H}_1$ reads [Berry, 2009]

$$\hat{H}_1(t) = i\hbar \sum_n (|\partial_t n\rangle \langle n| - \langle n| \partial_t n |n\rangle \langle n|) \tag{6.17}$$

where $|n\rangle$ is the n-th eigenstate of $\hat{H}_0(t)$. This STA protocol requires that $\langle \hat{H}_1(0)\rangle = \langle \hat{H}_1(\tau)\rangle = 0$. Hence, the frequency satisfies the following initial and final conditions.

$$\begin{aligned} \omega_t(0) = \omega_i, \quad \dot{\omega}_t(0) = 0, \quad \ddot{\omega}_t(0) = 0, \\ \omega_t(\tau) = \omega_f, \quad \dot{\omega}_t(\tau) = 0, \quad \ddot{\omega}_t(\tau) = 0. \end{aligned} \tag{6.18}$$

An interpolating ansatz which satisfies the mentioned boundary conditions is [Deffner et al., 2014],

$$\omega_t = \omega_i + (\omega_f - \omega_i)[10s^3 - 15s^4 + 6s^5] \tag{6.19}$$

in which $s = t/\tau_{adi}$. For a time-dependent QHO, $\hat{H}_1$ in Eq.(6.17) can be expressed as [Muga et al., 2010]

$$\hat{H}_1 = -\frac{\dot{\omega}_t}{4\omega_t}(\hat{x}\hat{p} + \hat{p}\hat{x}). \tag{6.20}$$

The total Hamiltonian governing the time evolution of the STA controlled QHO becomes

$$\hat{H}_{CD} = \frac{\hat{p}^2}{2m} + \frac{m\omega_t^2 \hat{x}^2}{2} - \frac{\dot{\omega}_t}{4\omega_t}(\hat{x}\hat{p} + \hat{p}\hat{x}). \tag{6.21}$$

Hence, for a time dependent QHO, the total Hamiltonian is quadratic in $\hat{x}$ and $\hat{p}$ and can be considered a generalized QHO [Mishima and Izumida, 2017],

$$\hat{H}_{CD} = \hbar\Omega_t(\hat{b}_t^\dagger \hat{b}_t + 1/2), \tag{6.22}$$

with an effective frequency Ω_t and the ladder operator $\hat{b}_t$ given by

$$\Omega_t = \omega_t \sqrt{1 - \dot{\omega}_t^2/4\omega_t^4}; \tag{6.23}$$

$$\hat{b}_t = \sqrt{\frac{m\Omega_t}{2\hbar}}(\zeta_t \hat{x} + \frac{i\hat{p}}{m\Omega_t}). \tag{6.24}$$

The work done during this process is given by

$$W = \int_0^{\tau_{adi}} \mathrm{Tr}(\dot{\hat{H}}_0(t)\hat{\rho}(t))dt \tag{6.25}$$

The expectation value of the CD driving is defined as [Abah and Lutz, 2018],

$$\left\langle \hat{H}_1(t) \right\rangle = \left\langle \hat{H}_{CD}(t) \right\rangle - \left\langle \hat{H}_0(t) \right\rangle = \frac{\omega_t}{\omega_i} \left\langle \hat{H}_0(0) \right\rangle \left(\frac{\omega_t}{\Omega_t} - 1 \right). \tag{6.26}$$

In order to obtain an accurate thermodynamic description of this controlled process, one should also keep track of the energy cost of CD-driving. The energetic cost of CD driving can be given as the time average of $\left\langle \hat{H}_1(t) \right\rangle$ [Abah and Lutz, 2018].

$$C_{\mathrm{STA}} = \frac{1}{\tau_{adi}} \int_0^{\tau_{\mathrm{adi}}} \left\langle \hat{H}_1(t) \right\rangle dt. \tag{6.27}$$

6.4 STE by CD-driving

In the previous section we briefly explained superadiabatic control protocol of an isolated quantum system which will be used to accelerate the unitary compression and expansion strokes of our quantum Otto engine. However, to be able to accelerate thermalization processes in quantum heat engines, one must implement a similar protocol for an open system. Such control methods are of utmost importance for designing quantum thermal devices within the context of finite time thermodynamics. In this section we will briefly explain a fast thermalization protocol for a driven open QHO which is presented in [Alipour et al., 2020, Dupays et al., 2020]. For open quantum systems, eigenvalues of the density matrix are time dependent. The time evolution of the density matrix can be written in terms of changes in its eigenprojectors and changes in the eigenvalues. Such a trajectory map can be written as

$$\dot{\hat{\rho}} = -\frac{i}{\hbar}[\hat{H}_{CD}, \hat{\rho}] + \sum_n \partial_t \lambda_n(t) \left| n_t \right\rangle \left\langle n_t \right| . \tag{6.28}$$

It is known that (after a modification to make it norm preserving) we can cast Eq. (6.28) into a Lindblad-like form [Alipour et al., 2020],

$$\partial_t\tilde{\rho} = \sum_{mn} \gamma_{mn}(\tilde{L}_{mn}\tilde{\rho}\tilde{L}_{mn}^{\dagger} - \frac{1}{2}\{\tilde{L}_{mn}^{\dagger}\tilde{L}_{mn}, \tilde{\rho}\}), \tag{6.29}$$

in which $\tilde{L}_{mn}$ and γ_{mn} are the jump operators and the dissipation rates in the Lindblad-like master equation for a unitarily equivalent trajectory $\tilde{\rho}$. In [Alipour et al., 2020] it is shown that, using the CD-driven STE framework, one can achieve the fast thermalization of a time-dependent QHO from an initial to a final thermal state. For an open and time-dependent QHO, we can write the trajectory map for the unitary transformed density matrix $\tilde{\rho} = \hat{U}_x\hat{\rho}\hat{U}_x^{\dagger}$ with $\hat{U}_x = \exp(im\alpha_t\hat{x}^2/2\hbar)$ as [Alipour et al., 2020],

$$\partial_t\tilde{\rho} = \frac{-i}{\hbar}\left[\frac{\hat{p}^2}{2m} + \frac{1}{2}m\tilde{\omega}_{CD}^2\hat{x}^2, \tilde{\rho}\right] - \gamma_t\left[\hat{x}, [\hat{x}, \tilde{\rho}]\right], \tag{6.30}$$

in which $\tilde{\omega}_{CD}$ is the effective frequency and γ_t is the effective dissipation rate. Such a procedure for shortcut to thermalization can be implemented by modulation of the driving frequency and the dephasing strength [Alipour et al., 2020, Dupays et al., 2020]. For Eq. (6.30) we have [Alipour et al., 2020],

$$\begin{aligned}
\omega_{CD}^2 &= \omega_t^2 - \alpha_t^2 - \dot{\alpha}_t; && (6.31)\\
\gamma_t &= \frac{m\omega_t}{\hbar}\frac{\dot{u}_t}{(1-u_t)^2}; && (6.32)\\
u_t &= e^{-\beta_t\hbar\omega_t}; && (6.33)\\
\alpha_t &= \zeta_t - \dot{\omega}/2\omega_t; && (6.34)\\
\zeta_t &= -\frac{\dot{\omega}}{2\omega_t} + \frac{\dot{u}_t}{1-u_t^2}. && (6.35)
\end{aligned}$$

Here, β_t is the inverse temperature at time t. Similar to the STA case, shortcut to equilibrium is achieved for a general setup by requesting ω_t to follow Eq. (6.19) (with $s = t/\tau_{iso}$) and β_t to conform to the ansatz [Alipour et al., 2020],

$$\beta_t = \beta_i + (\beta_f - \beta_i)[10s^3 - 15s^4 + 6s^5], \tag{6.36}$$

in which $s = t/\tau_{iso}$. For this protocol, an entropy based definition for the infinitesimal thermal energy and work can be calculated as given in [Alipour et al., 2022].

$$đ\mathcal{Q} = đQ - đW_{CD} = \text{Tr}\left[\tilde{\mathcal{D}}_{CD}(\tilde{\rho})\hat{H}_0\right] dt; \tag{6.37}$$

$$đ\mathcal{W} = đW + đW_{CD} = \text{Tr}\left[\tilde{\rho}\left(\dot{\hat{H}}_0 - i\left[\hat{H}_0, \tilde{H}_{CD}\right]\right)\right] dt \tag{6.38}$$

in which $\tilde{H}_{CD}$ is the transformed CD Hamiltonian governing the coherent evolution and $\tilde{\mathcal{D}}_{CD} = -\gamma_t\left[\hat{x}, [\hat{x}, \tilde{\rho}]\right]$ is the transformed dissipator contributing to the coherent and incoherent evolution in Eq. (6.30) respectively. $đW_{CD} = -i\text{Tr}[[\hat{H}, \tilde{H}_{CD}]\tilde{\rho}]dt$ is the dissipative work, due to the CD evolution along the state trajectory. $đ\mathcal{Q}$ and $đ\mathcal{W}$ are heat and work calculated in the instantaneous eigenbasis of $\tilde{\rho}$. In Eq. (6.37) and Eq. (6.38), $đQ$ and $đW$ signify the infinitesimal changes in the conventional definitions of heat $Q = \text{Tr}[\dot{\hat{\rho}}\hat{H}_0]$ and work $W = \text{Tr}[\hat{\rho}\dot{\hat{H}}_0]$, resulting from Spohn separation [Spohn, 2008], in which the coherent (dissipative) changes of the internal energy due to the master equation is phenomenologically labelled as work (heat).

However, it is argued in [Alipour et al., 2022] that for a general evolution of an open quantum system, the contribution of changes in the internal energy which one can label as heat must also coincide with the contribution associated with changes in the entropy. In general, Spohn seperation doesn't necessarily respect this condition. As a resolution to this issue, the contribution to the changes in the internal energy associated with changes in the eigenvalues of the density matrix is called heat and the contribution associated with the changes in the eigenprojectors is called work. For the CD-driven harmonic oscillator driven to thermalization, these contributions take the form given in Eq. (6.37) and Eq. (6.38) as discussed in [Alipour et al., 2022]. Therefore, for the driven system described in this section, the actual values for heat ($\mathcal{Q}$) and work ($\mathcal{W}$) during the process can be found by integrating Eq. (6.37) and Eq. (6.38) throughout the trajectory. $đW_{CD}$ quantifies the environment-induced dissipative work (positive or negative) due to CD driving of the open quantum system evolving for a time dt. More specifically, it is argued that for a system initialized in an equilibrium state and whose dynamics has a unique equilibrium steady state, the amount of $đW_{CD}$ quantifies the energetic cost associated with the difference between the real trajectory and the quasistatic one [Alipour et al., 2022]. Therefore, the magnitude of the dissipative work at each infinitesimal time step can be associated with the control cost for its corresponding infinitesimal evolution along the trajectory. Since during an isochoric process the Hamiltonian is static ($\dot{\hat{H}}_0 = 0$) we can define the integral of the absolute value of $đW_{CD}$ through the state trajectory during this process as the total cost function

$$C_{\text{STE}} = \int_0^{\tau_{\text{iso}}} \left| \text{Tr}[[\hat{H}_0, \tilde{H}_{CD}]\tilde{\rho}] \right| dt. \tag{6.39}$$

This cost is not defined operationally but based on the arguments that are given, any driving protocol must expend at least the amount of energy given in Eq. (6.39) to drive the system for the duration of the isochore. Therefore it can be thought of as a lower bound on any operational cost that one can define for such a process.

6.5 *Otto engine with CD driven STA and STE*

Using the frameworks explained in the previous sections, we propose a CD driven Otto engine with a QHO as a working medium. In Fig. 6.1 we boost the engine using CD driven STA protocols for expansion and compression and using a CD driven STE protocol for the hot isochore. The cold isochore is modeled by a Markovian master equation and no control Hamiltonian is applied during this step.

Adiabatic evolution implies $\beta_f \omega_f = \beta_i \omega_i$. Hence, after an adiabatic driving for the compression (expansion) stroke, the evolution of the system leads to a density matrix whose statistical distance is close to the thermal density matrix at $\omega_2 = \omega_h$ and $T_2 = (\omega_h/\omega_c) \times T_c$ ($\omega_4 = \omega_c$ and $T_4 = (\omega_c/\omega_h) \times T_c$). We can quantify this statistical distance using fidelity. Also, due to the fact that for an isochoric process the frequency must be kept constant, we will use $\omega_t = \omega_h$ throughout the CD-driven hot isochoric stroke, which means that in order to achieve STE we will only consider modulation of the dephasing strength.

We distinguish between the thermodynamic efficiency (η^{th}) of the control engine, which doesn't take into account the control costs and is given by an expression similar to Eq. (6.10), and the operational efficiency (η^{op}) which considers the energetic costs. The operational efficiency for the CD-driven Otto engine can be calculated taking into account the costs for STA and STE protocols.

$$\eta^{op} = -\frac{W_{12} + W_{34}}{\mathcal{Q}_{23} + C_{adi}^{1\to 2} + C_{iso}^{2\to 3} + C_{adi}^{3\to 4}}. \tag{6.40}$$

In Eq. (6.40), W_{12} and W_{34} are calculated using Eq. (6.25) and $\mathcal{Q}_{23}$ is calculated by integrating Eq. (6.37). $C_{adi}^{1\to 2}$, $C_{iso}^{2\to 3}$ and $C_{adi}^{3\to 4}$ are the driving costs for the compression, cold isochore and expansion strokes and are defined in the previous sections. Power output is calculated using a similar expression given in Eq. (6.9) by substituting W_{12} and W_{34} into the equation.

6.6 Results

In this section, we compare UNA, STA, and STÆ Otto engines in terms of power and efficiency. To this end, we choose $\omega_c = \omega_1 = \omega_4 = 1$ and $\omega_h = \omega_2 = \omega_3 = 2.5$. We assume the durations of the two adiabatic strokes to be identical (τ_{adi}), and similarly for the two isochores (τ_{iso}). We vary τ_{adi} and τ_{iso} independently between 0.7 and 7.5. The temperatures for the cold and hot bath are taken to be $T_c = T_1 = 1$ and $T_h = T_3 = 10$, respectively. We further assume that the heat conductivities for the hot and cold isochores are equal, i.e., $\Gamma_h = \Gamma_c = 0.22$. All numerical values are given in appropriate units (energy in units of $\hbar\omega_c$, temperature in units of $\hbar\omega_c/k_B$, etc.). The parameter ranges were chosen such that all relevant operational regimes were accessible in the analysis. Throughout this section, all the calculated efficiencies are operational except when it is directly stated otherwise. For convenience we drop the "op" superscript for the operational efficiency. We have used the open source package QuTiP for our calculations [Johansson et al., 2012b].

Fig. 6.2 compares both the power output of the three engines (top panel) and their efficiencies (bottom panel) as a function of the stroke durations, for a single

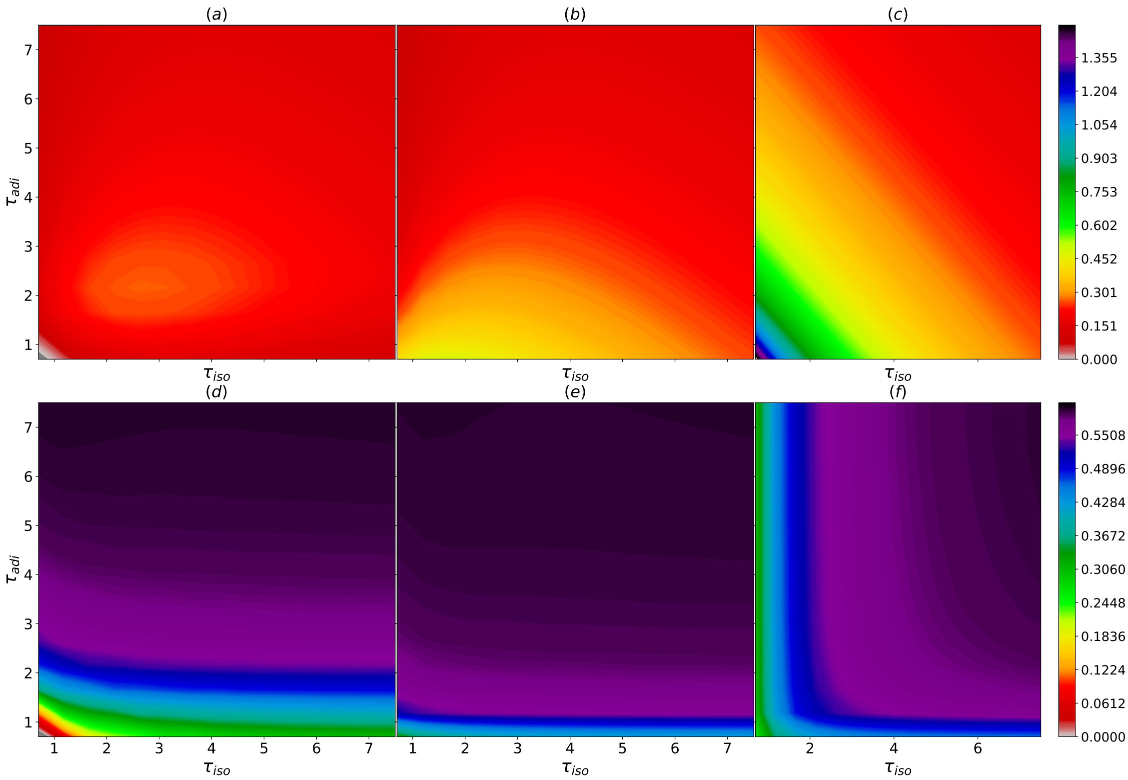

Figure 6.2: Power and efficiency of the Otto engine as a function of the duration of the isochoric and adiabatic branches. Top row: Power vs τ_{adi} and τ_{iso} for the (a) UNA engine; (b) STA engine; (c) STÆ engine. Bottom row: Efficiency vs τ_{adi} and τ_{iso} for the (d) UNA engine; (e) STA engine; (f) STÆ engine. Negative power and efficiency results for the finite time Otto engine are greyed out.

cycle of operation starting from the thermal state (ω_c, T_c) which is indicated as "1" in Fig. 6.1. It is evident from Fig. 6.2(a) that for small values of τ_{adi} and τ_{iso} the UNA engine results in a negative power output and hence, does not behave as a proper heat engine. However, in STA Fig. 6.2(b) and STÆ Fig. 6.2(c) engines, a positive power output is produced even for small stroke times. It should be noted that we have not considered stroke times smaller than 0.7 because for the parameter regime that we chose, this results in trap inversion (with an infinite STA driving cost). The maximum power output of the STÆ and STA engines occur for the smallest stroke times however for the uncontrolled engine maximum power occurs for an intermediate time $\tau_{adi} = \tau_{iso} \approx 2.3$, after which the power output declines. The figures demonstrate that the maximum power is larger for STÆ engine than the STA-only engine, which itself yields higher power than the finite-time engine with no CD-driving. When cycle time is dominated by either isochoric or adiabatic processes the power output of the uncontrolled engine is low and, as expected, the STA engine yields higher a power output when the cycle time is dominated by the isochoric processes. However, STÆ engine outputs a relatively large values for power whether the contribution of the isochoric processes is larger for the cycle time than the adiabatic ones or vice-versa. For large values of the cycle time, the difference between the power outputs of the three engines become negligible as expected. Fig. 6.2(d) shows that in the parameter regime that we have considered, the UNA engine yields a negative value for efficiency as the cycle time becomes very small. Hence, it doesn't act as a proper heat engine. Comparing Fig. 6.2(d), Fig. 6.2(e) and Fig. 6.2(f) we see that for small values of τ_{adi}, the efficiency is comparatively small for all three engines. However, STA and STÆ engines give larger values for the efficiency, the former displaying a superior performance. For cycle times dominated by τ_{adi} and short durations of the isochoric branches, the STÆ engine performs poorly as compared with the UNA and STA engines. As τ_{adi} and τ_{iso} become larger, the difference between the values of the efficiency of the three engines diminish. To see finer details of the performance metrics of the three engines for a subset of the cycle times considered in Fig. 6.2, in Fig. 6.3 efficiency and power of the engines are presented for $\tau_{adi} = \tau_{iso} = \tau$. In Fig. 6.3(a) we see a dramatic difference between the power output of the STÆ engine with the other two engines considered in this study specially for short cycle times. This figure shows a clear advantage of using CD-driving for thermalization and adiabaticity to enhance the power output. From Fig. 6.3(b) it is clear that for equal time allocated to isochoric and adiabatic branches, the largest to smallest efficiencies are obtained for the STA engine, the STÆ engine and the UNA engine, respectively for smaller cycle times. For the intermediate cycle times efficiency of the UNA engine exceeds that of STÆ. For larger cycle times the

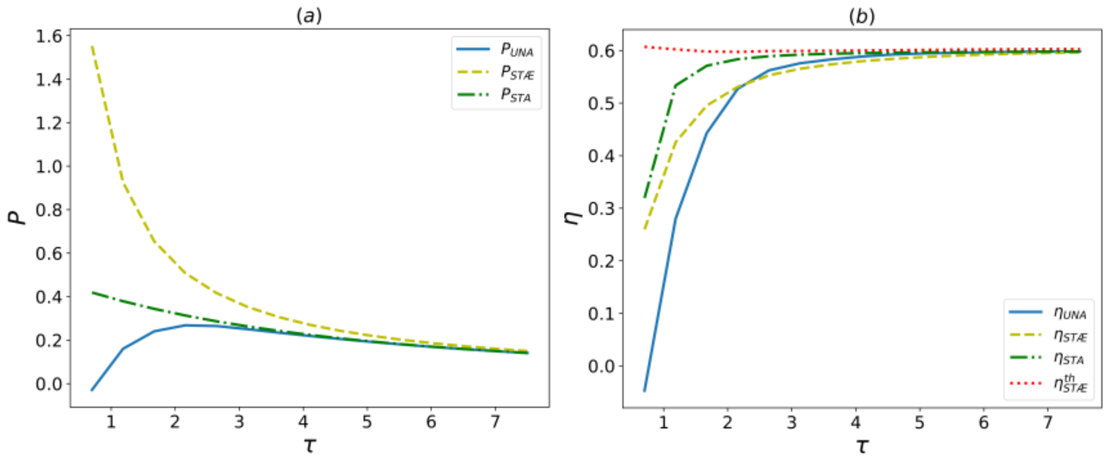

Figure 6.3: Power and efficiency characteristics of the controlled and uncontrolled finite time Otto engines for an equally allocated time for their isochoric and adiabatic branches, $\tau_{iso} = \tau_{adi} = \tau$. (a) Power vs τ: UNA engine (solid blue), STA engine (green dash-dotted), STÆ engine (yellow dashed). (b) Efficiency vs τ: UNA engine (solid blue), STA engine (green dash-dotted), operational efficiency (yellow dashed) and thermodynamic efficiency (red dotted) of the STÆ engine.

efficiency of the three engines approach the ideal value of $1 - \omega_c/\omega_h = 0.6$. Also, for the entirely of cycle times, the efficiency of all three engines is below the Carnot efficiency $1 - T_c/T_h = 0.9$ and Curzon-Ahlborn (CA) efficiency $1 - \sqrt{T_c/T_h} \approx 0.68$. Note that without considering the costs, the thermodynamic efficiency of the STÆ engine equals the ideal value.

In Fig. 6.4 we can see the control costs for the STÆ engine. As expected, Fig. 6.4(a) and Fig. 6.4(c) show that the energetic cost for CD-driving for adiabaticity decreases for longer τ_{adi}, whereas in Fig. 6.4(b) we can see that the cost for driving the system to thermalization shrinks as we increase τ_{iso}. Comparison between the costs for the controlled strokes in the STÆ engine reveal that the maximum of the energetic control costs in increasing order are for the compression, expansion and thermalizaion strokes. Moreover, the expansion stage has more populations in excited levels as it starts after the heating stroke, in contrast to compression stage where the populations are less as it follows the cooling stroke. Accordingly, more energy needs to be spent by the external agent to control and stop the transitions during accelerated adiabatic transformation in the expansion stroke, a fact which was also stated in earlier studies [Li et al., 2021]. Next, we move on to the performance metrics of the engines in their respective limit cycles. Our numerical calculations show that all three engines reach a limit cycle throughout the cycle times that we have considered in this study. One has to note that in the limit cycle the state of the working medium at the end of each stroke do not necessarily coincide with the ones given in the ideal Otto engine as represented by Fig. 6.1, unless the times allocated for each stroke are very large. Calculating the fidelity of the state of the working medium and the final state after each repetition of the cycle, we see observed that 7 cycles are enough to converge to the limit cycle of the engines for all the cycle times. In Fig. 6.5 the results for the power and efficiency of the engines are shown.

From Fig. 6.5(a) we can observe that the UNA engine yields a negative power output for a considerably large subset of allocated times for the adiabatic and isochoric strokes. Comparing Fig. 6.5(a) and Fig. 6.2(a), we see that the uncontrolled engine is much more unreliable in its limit cycle than when we only consider one

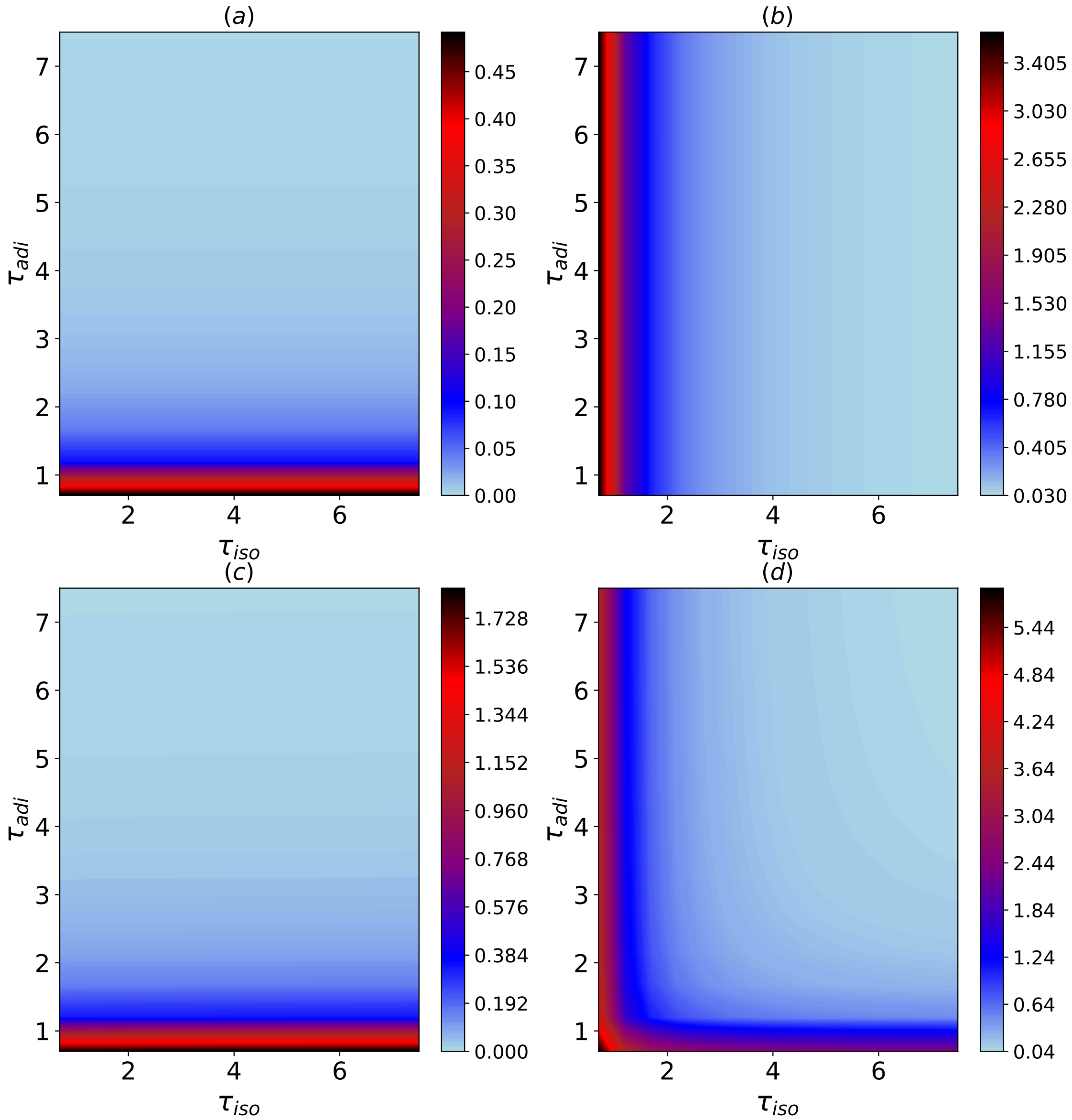

Figure 6.4: Cost of the STA and STE driving for one cycle of the STÆ engine vs τ_{adi} and τ_{iso}. (a) Cost of the STA driving for adiabatic compression; (b) cost of the STE driving for hot isochore; (c) cost of the STA driving for adiabatic expansion; (d) total costs for one cycle.

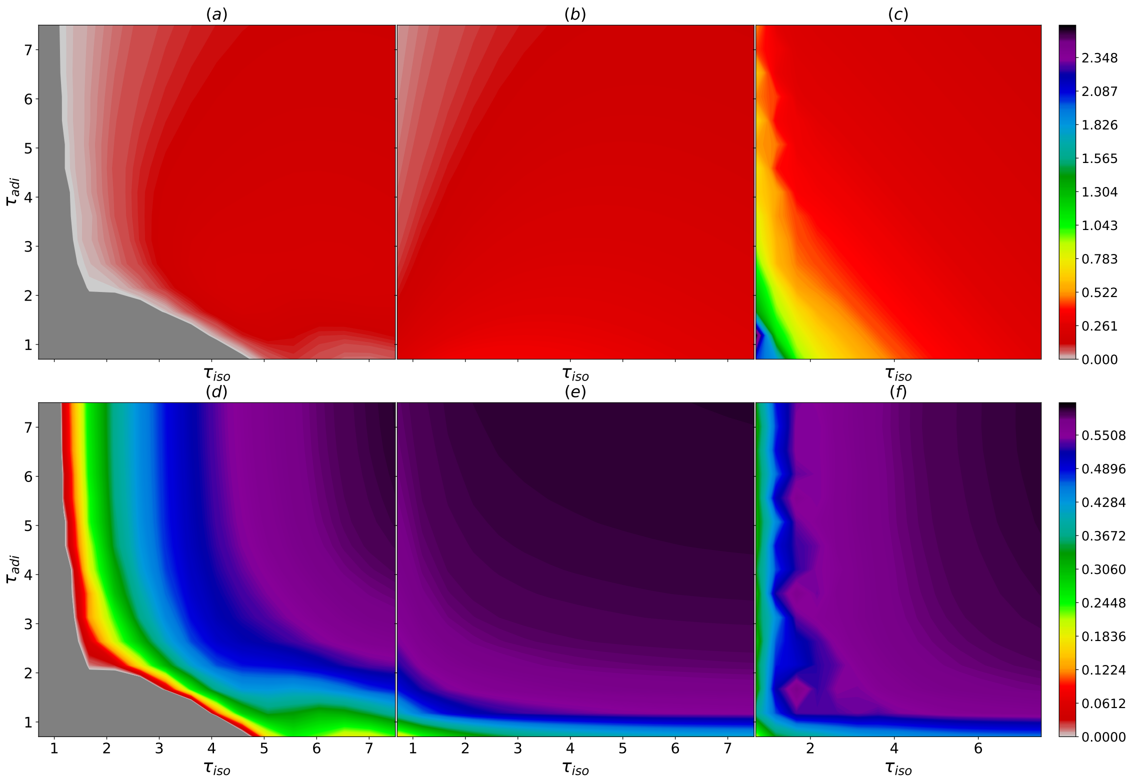

Figure 6.5: Power and efficiency of the Otto engine at its limit cycle as a function of the duration of the isochoric and adiabatic branches. Top row: Limit cycle power vs τ_{adi} and τ_{iso} for the (a) UNA engine; (b) STA engine; (c) STÆ engine. Bottom row: Limit cycle efficiency vs τ_{adi} and τ_{iso} for the (d) UNA engine; (e) STA engine; (f) STÆ engine. Negative power and efficiency results for the finite time Otto engine are greyed out.

cycle of operation. In comparison, Fig. 6.5(b) and Fig. 6.5(c) give a positive power output in their limit cycles for all τ_{adi} and τ_{iso}. Moreover, in Fig. 6.5(a) we see that in its limit cycle, the UNA engine yields a vanishingly small power outputs for cycle times dominated by isochoric/adiabatic processes. On the other hand, Fig. 6.5(b) shows that the power output in the STA engine gets vanishingly small only for the cycle times dominated by adiabatic processes. However, Fig. 6.5(c) shows a clear advantage of using STÆ engine, in which power output is much larger compared to the UNA and STA engines, specially when we consider isochoric or adiabatic process dominated cycle times. The figure shows that similar to the case of single cycle, for the STAÆ engine in its limit cycle, the power output is higher for smaller values of τ_{adi} and τ_{iso}. The grey areas in Fig. 6.5(d) show that for a considerable section of the

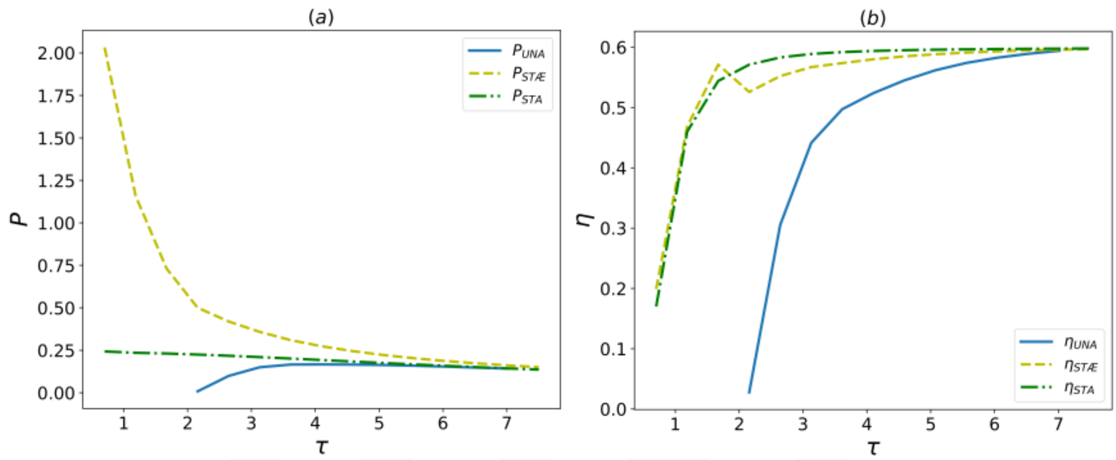

Figure 6.6: Limit cycle power and efficiency characteristics of the controlled and uncontrolled finite time Otto engines for an equally allocated time for their isochoric and adiabatic branches, $\tau_{iso} = \tau_{adi} = \tau$. (a) Limit cycle power vs τ: UNA engine (solid blue), STA engine (green dash-dotted), STÆ engine (yellow dashed) of the engine with STA on its adiabatic strokes and STE on its hot isochore. (b) Limit cycle efficiency vs τ: UNA engine (solid blue), STA engine (green dash-dotted), STÆ engine (yellow dashed). Negative power and efficiency results for the finite time Otto engine are not displayed.

considered allocated times for the isochoric and adiabatic strokes, the uncontrolled engine doesn't act as a proper heat engine. In its limit cycle the efficiency of the UNA engine is low compared to the STÆ and the STA engines except when τ_{iso} and τ_{adi} are both large. Comparing Fig. 6.5(e) and Fig. 6.5(f) we see that surprisingly, for cycles with small τ_{iso}, the efficiency of the STÆ engine is smaller than that of the STA engine except when τ_{adi} is also small. Although, this doesn't mean that the STA-only engine is superior to the STÆ engine for the mentioned cycle time allocations because in this case, as seen in Fig. 6.5(b) the power output of the STA-only engine becomes much smaller than the STÆ engine. An interesting aspect of the STÆ protocol limit cycles is that the performance is non-monotonous in τ_{adi}. As a result, high-power/high-efficiency islands appear, such as the one observed around $\tau_{adi} = \tau_{iso} \approx 1.6$ in Fig. 6.5(f). In order to make a more detailed comparison of the performance metrics of the engines for a subset of the stroke times considered in this study, in Fig. 6.6 we present efficiency and power of the heat engines for $\tau_{adi} = \tau_{iso} = \tau$. In Fig. 6.6(a) we can see that the STÆ engine yields a much higher power output than the STA and UNA engines. Comparing Fig. 6.3(a) and Fig. 6.6(a) we see that in their limit cycle, the power of the STA and UNA engines get reduced, as compared with the case of single cycle, throughout the cycle times. However, for the STÆ engine the power output for the limit cycle is higher than that of the single cycle for the entirety of the considered cycle durations. As shown in Fig. 6.6(b), in its limit cycle, the efficiency of the STÆ engine is no longer monotonic in the cycle time. The difference between the efficiencies of the uncontrolled engine and the controlled engines is more dramatic in their limit cycles and their efficiency values don't approach each other to the ideal value of $1 - \omega_c/\omega_h = 0.6$ unless the cycle time is very large. The results show that the STÆ engine has higher efficiency than the STA engine, for smaller cycle times. However, after a certain value for the stroke durations, efficiency of the STA engine exceeds that of the STÆ engine. Inspecting Fig. 6.3(a) and Fig. 6.3(b) we see that there exists a time interval for which the STÆ engine achieves higher efficiency and power than the STA engine.

In Fig. 6.7 the costs for CD-driving at the limit cycle for the STÆ engine are presented. Similar to the case of single cycle, we can see that the cost of the hot isochoric and adiabatic strokes are highest for short τ_{iso} and τ_{adi} respectively. Additionally, for short cycle times in the limit cycle the share of the thermalization cost is the highest in the total control cost similar to the case of single cycle. Again, as τ_{adi} and τ_{iso} is increased, the control costs of the adiabatic and hot isochoric strokes decreases. However, for small τ_{adi} in the limit cycle, the cost for CD-driving during

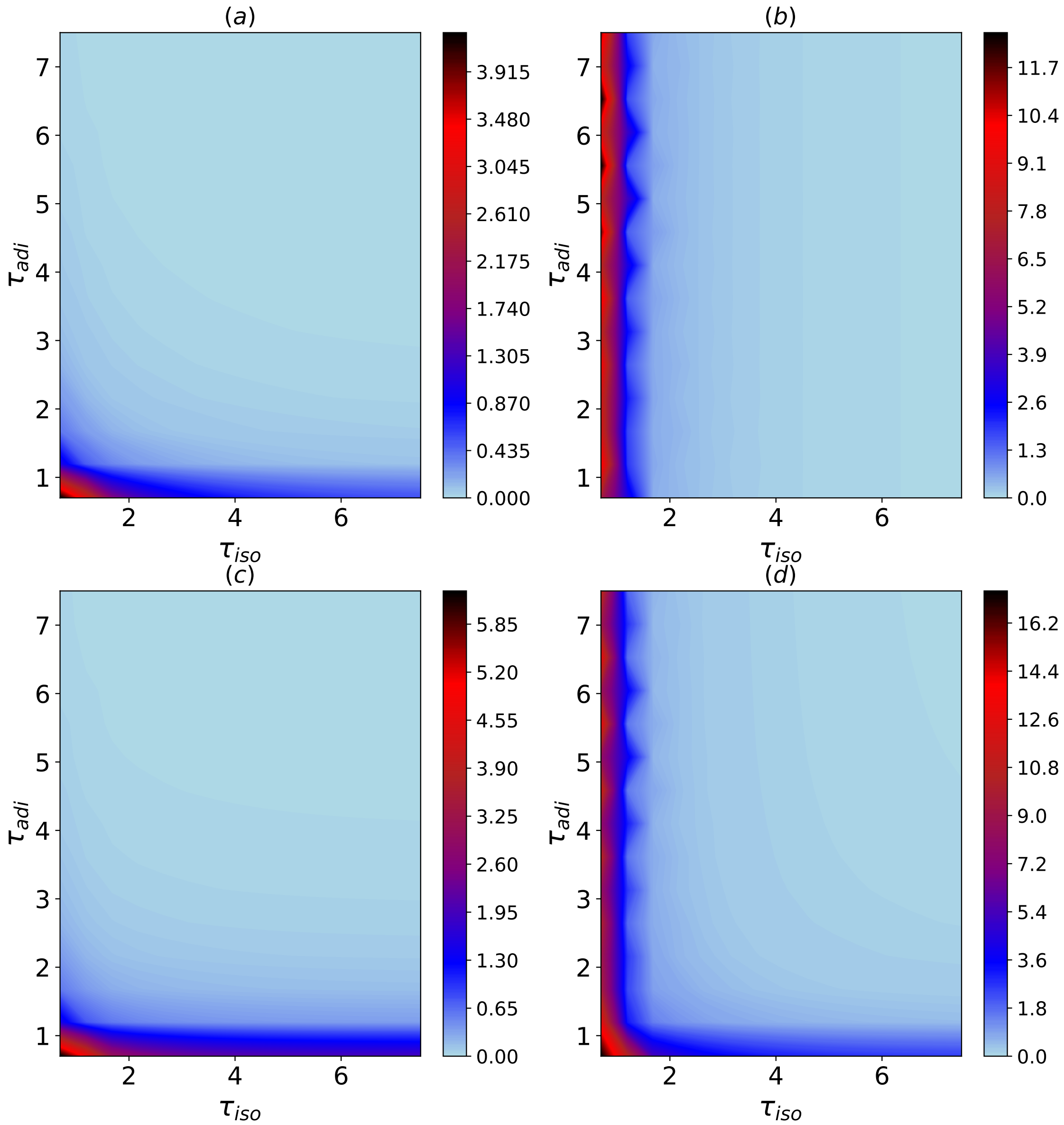

Figure 6.7: Cost of the STA and STE driving for the limit cycle of the STÆ engine vs τ_{adi} and τ_{iso}. (a) Cost of the STA driving for adiabatic compression; (b) cost of the STE driving for hot isochore; (c) cost of the STA driving for adiabatic expansion; (d) total costs for one cycle.

the expansion and compression strokes becomes relatively small for larger τ_{iso} as opposed to what we see for a single cycle.

Comparing Fig. 6.4 and Fig. 6.7 we see that for the limit cycle, the control costs tend to increase as compared to the single cycle case. The difference between the behavior of the cost functions for a single cycle and limit cycle can be explained by the fact that for short cycle durations, specifically for a short cold isochoric stroke, upon completion of a single cycle the system doesn't return to the thermal state at T_c and ω_c. Additionally, non-commutativity of the system Hamiltonian at different times and also non-commutativity of the system and control Hamiltonians will induce diabatic transition of the populations and also generate coherence in the system's density matrix in the energy eigenbasis. It is evident from the definition of the cost functions Eq. (6.27) and Eq. (6.39) that both the diagonals and off-diagonals of the density matrix influences the cost value along their respective processes. Therefore due to the mentioned diabatic transitions and generated coherences, which are more pronounced for smaller cycle durations, in the limit cycle the total control cost in the limit cycle will be larger than that of a single cycle.

Fig. 6.8 shows the fidelity between the density matrix at the end of each stroke and their counterparts in an ideal quasistatic quantum Otto engine for different time allocation of the cycle durations. The density matrices at the end of each stroke for an ideal quasistatic heat engine are thermal states at (T_i, ω_i) in which $i = 1, 2, 3, 4$. The results are shown for a single cycle and an equal time duration for the isochoric and adiabatic strokes. If the fidelity between the density matrix at the end of a finite-time stroke in a controlled heat engine and its corresponding quasistatic counterpart is one, it is an indicator that the quantum evolution governing the dynamics of the stroke has successfully achieved its control target. From Fig. 6.8(a) we see that in the UNA engine none of the four branches yield a high fidelity unless the stroke times are very large. From Fig. 6.8(b) we see that implementation of STA drives the density matrix at the end of the compression stroke to its corresponding

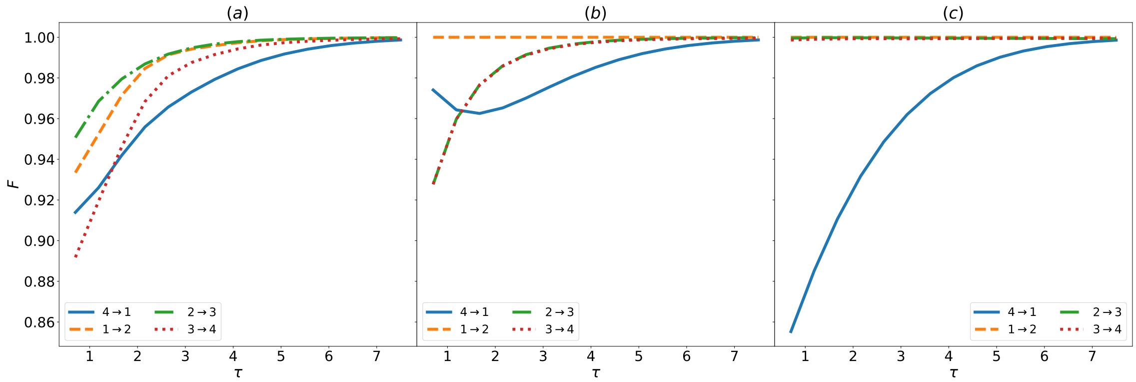

Figure 6.8: Fidelity between the density matrix at the end of each stroke and their respective counterparts for an ideal quasistatic quantum Otto engine vs the stroke duration $\tau = \tau_{adi} = \tau_{iso}$. The calculations are carried out for a single cycle for (a) UNA engine (b) STA engine (c) STÆ engine. The solid blue, dot-dashed green, dashed orange and dotted red curves are for the cold isochore, hot isochore, compression and expansion strokes respectively.

quasistatic counterpart with almost perfect fidelity regardless of the stroke duration. It is worth mentioning that the same doesn't happen for the expansion stroke because the thermalization stroke doesn't thermalize the system for smaller duration of this branch and the control law for the expansion presumes that the temperature at the beginning of the stroke is $T_3 = T_h$. From Fig. 6.8(c) we see that all of the controlled strokes in the STÆ achieve perfect fidelity regardless of their duration.

In Fig. 6.9 we show the fidelity between the density matrix at the end of each stroke and their counterparts in an ideal quasistatic quantum Otto engine for limit cycle and an equal time duration for the isochoric and adiabatic strokes. Since the three engines under investigation have different cycle propagators, they will reach different limit cycles at different times. This fact is evident upon comparing the fidelity curves for the cold isochore process of the UNA, STA and STÆ engines in Fig. 6.9 for different times. Also from Fig. 6.9(b) and Fig. 6.9(c), we see that in the limit cycle, non of the controlled branches in the STA and STÆ engines achieve

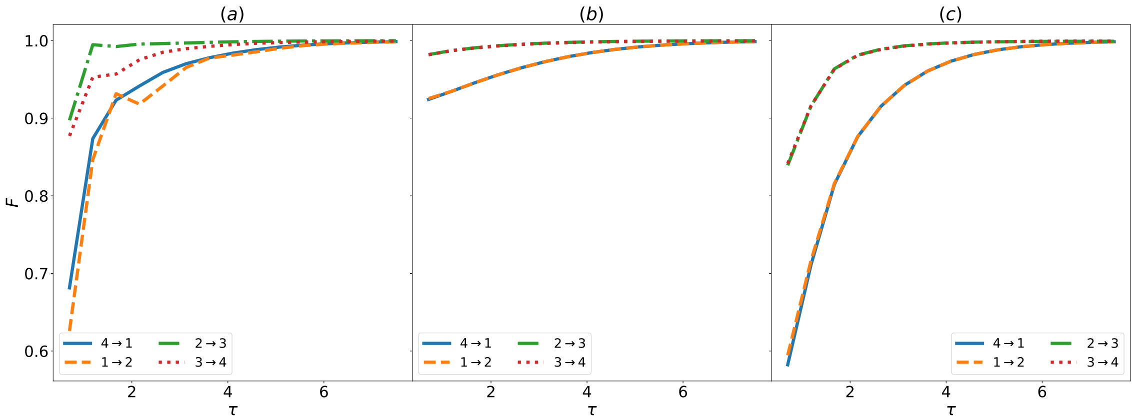

Figure 6.9: Fidelity between the density matrix at the end of each stroke and their respective counterparts for an ideal quasistatic quantum Otto engine vs the stroke duration $\tau = \tau_{adi} = \tau_{iso}$. The calculations are carried out for the limit cycle for (a) UNA engine (b) STA engine (c) STÆ engine. The solid blue, dot-dashed green, dashed orange and dotted red curves are for the cold isochore, hot isochore, compression and expansion strokes respectively.

unit fidelity unlike what was the case for a single cycle as displayed in Fig. 6.8(b) and Fig. 6.8(c). As explained earlier, this is due to the diabatic populations transitions and accumulated coherence in the energy eigenbasis (which increase the cost in limit cycle) and the differences between the fidelities for a single cycle and limit cycle shows confirms this fact.

In Fig. 6.10 we provide the coherence accumulated in the density matrix for different $\tau = \tau_{iso} = \tau_{adi}$ calculated for each cycle number until the limit cycle is reached. To quantify coherence, l1-norm of coherence is used. The results show that as a general trend, for shorter cycle durations more coherence is accumulated in the density matrix. Also, as the cycle number increases, until the limit cycle is reached, the amount of coherence gets larger. The results displayed in Fig. 6.10 also demonstrate a clear reason based on the contribution of the off-diagonals of the density matrix that why the cost functions yield larger values at the limit cycle.

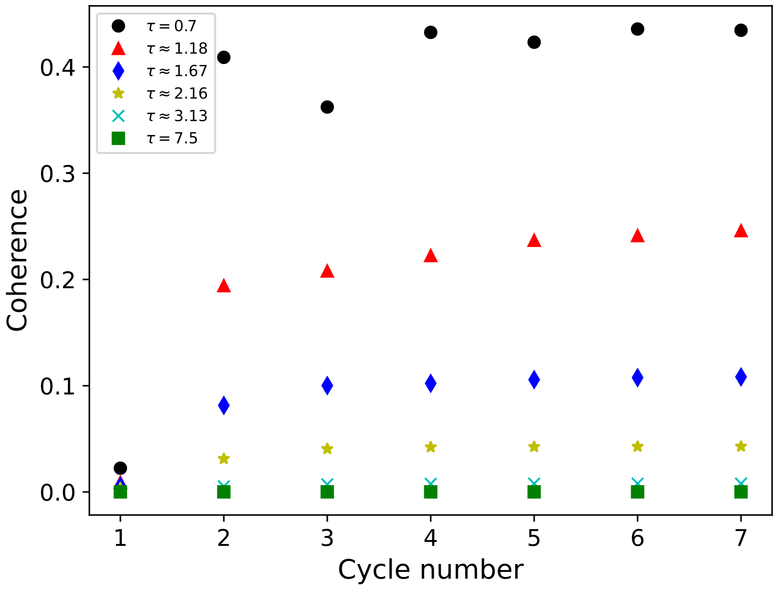

Figure 6.10: l1-norm coherence of the density matrix at the end of cold isochore vs cycle number for different durations of cycle. $\tau = \tau_{adi} = \tau_{iso}$ for the STÆ engine.

Chapter 7

CONCLUSION

In Chapter 2, we studied the metrological capability of different states of light for probing a simple model of the retinal network. Our objective was to analyze the parameter estimation error by calculating the Fisher information matrix for gain parameters in this network, given a photon distribution by Fock, coherent and thermal states of light. These calculations are performed for in-vitro and in-vivo scenarios which include both lossless conditions and including optical losses. We investigated the error bounds for the single parameter and multi-parameter cases using the inverse of the Fisher information (CRLB) and the volume of the error ellipsoid as their corresponding figures of merit.

Our study shows that the minimum error ellipsoid volume for thermal light is much larger than coherent and Fock state light for all parameters. When η is considered very small, Fock and coherent states outperform thermal state for parameter estimation task, Fock state having a smaller error bound. Error ellipsoid volume difference between Fock and coherent states increases with η. This difference becomes even more significant when smaller mean photon numbers are considered. In all cases, the Fock state has superior metrological advantage even for more complicated network topologies (increased numbers of cells and layers). The smallest value for the error ellipsoid volume is obtained for large values of η and $\bar{n}$. This intuitively makes sense, because a large photoreceptor efficiency and a larger stimuli result in a stronger response, from which a more accurate estimation of the underlying parameters would be possible.

Including optical losses increases the error bound for all states. Calculating for the case with equal and unequal weight factors, we showed that similar to the case with no optical losses, Fock state and thermal state yield the smallest and largest error ellipsoid volumes, respectively. Hence the advantage of quantum states of light for parameter estimation on the retina network persists even when considerable optical losses are introduced.

In Chapter 3, our theoretical and experimental framework illustrates that employing nonlocal polarimetry with an initially entangled state leads to improved precision and accuracy in extracting information about sample characteristics compared to the case of local polarimetry. Our results show that using quantum entanglement can increase the precision and accuracy depending on the chosen estimators and existing noise channels. We have seen that the experimental noise induces bias in our estimators and therefore reduces the accuracy of the estimated results. Therefore, to harness the full potential of quantum states for metrological tasks, one needs to address the issue of noise-induced bias as well.

Our investigation reveals the presence of a quantum nonlocality advantage within the ambit of two-channel entangled state quantum polarimetry. However, it is pertinent to note that this quantum advantage remains suboptimal. Within the realm of quantum metrology, the utilization of NOON states, expressed in the form $(|HH\rangle + |VV\rangle)/\sqrt{2}$, could conceivably offer a higher enhancement in precision compared to local polarimetry [Dowling and Seshadreesan, 2015]. Furthermore, such states could potentially be harnessed to attain quadratic advantages with increasing photon numbers. While our current study identifies the nonlocal advantage, the pursuit of optimization for this nonlocal scheme remains an open challenge, awaiting exploration in future investigations.

In Chapter 4, we studied the precision limits for single parameter estimation of the rotation angle of the Stokes vector in a polarimetric setup, within the framework of quantum polarimetry. We have incorporated the effects of depolarization and diattenuation channels within our numerical calculations and considered different orders of implementations of these channels. For the sake of completeness, we have utilized three different depolarization channels found in the literature in our calculations. The results show that, for our chosen sets of parameters and operators, QFI greatly diminishes upon implementation of the depolarization channel. For depolarization based on convex combination of rotations and the isotropic depolarization, there exists a minimal difference between forward and reverse decomposition in the final result for the QFI for weak depolarization and the difference is slightly more pronounced in the strong depolarization regime. However, for the anisotropic depolarization, after applying the depolarization channel, the reverse and forward decompositions yield different behavior with the average number of photons for Kings of Quantumness and the NOON state.

The scaling of coherent state remains monotonic with the average number of photons and both decompositions yield the same result. However, for NOON state and Kings of Quantumness QFI becomes non-monotonic with the average photon number in the strong depolarization regime. As expected, implementing diattenuation decreases QFI for all cases. However, our results demonstrate that metrological power of the NOON state diminishes more than that of Kings of Quantumness such that for larger average photon numbers the latter yields a higher QFI. Therefore our results suggest that, although HL scaling is lost after applying the noise channels, one can potentially utilize low photon number NOON states to gain a quantum advantage in polarimetric retardation measurements on a lossy medium. Possible experimental procedure for carrying out such a task is proposed.

In Chapter 5, inspired by the recent developments concerning the constructive effect of noise in energy transport in biological light harvesting complexes, we have studied the effect of an auxiliary, HSE interacting with a linear system of three qubits on heat transport from a hot bath to the cold bath, connected by this system. We saw that such a coupling modulates, and in a broad range of parameters, enhances, the transient and steady state heat transport. This is partly due to the changes in the energy levels of the total system Hamiltonian, including the interaction with the HSE. Due to these changes, the thermal baths can access and induce transitions in the energy levels of the system more easily, hence enhancing the heat transport.

We conducted a full scale numerical characterization of the steady-state heat flux, with the independent parameters being the system-HSE coupling, inter-HSE coupling and coherence of the HSE qubits. Our results indicate that, for the parameter regime considered in this study, an increase in system-HSE and inter-HSE couplings corresponds to an increase in the steady-state heat current, especially for the larger values of the coupling constants. Coherence within the HSE generally has a smaller effect on the steady-state heat flux and its effect is only noticeable within a smaller parameter regime. The enhancement of the energy transfer due to the HSE coherence is more pronounced for the larger coupling constants g_a and g_b considered in this study.

As a future direction, one might consider the effect of non-Markovianity within the heat baths or the HSE on the heat flux by considering long range interactions between their corresponding qubits. It might also be worthwhile to study the effect of system-environment correlations or the correlations in the bath on heat transfer. Finally, our work in a sense can be understood as an open-loop control of the thermal energy through a simple network by an auxiliary environment. One might consider a more complex network of qubits and study where and how strong the local interactions with the HSE should be in order to optimally modulate the heat flux.

In Chapter 6, we studied the thermodynamic performance of a quantum harmonic Otto engine in finite time and compared three cases of Otto engine with no CD-driving, Otto engine with STA on the adiabatic strokes and Otto engine with STA on the adiabatic strokes and STE on the hot isochoric branch. We have included the costs of driving the engine for calculating the thermodynamic figures of merit. In our calculations we have considered two modes of operation. First we studied the thermodynamic performance criteria for a single cycle and then we calculated the same figures of merit for the engines running in their respective limit cycles.

Our results for single cycle indicate that controlling the hot thermalization process in the Otto engine greatly increases the power output of the engine for the entirety of the considered stroke times, specifically for short cycle time durations. Taking the control costs into account, the STÆ engine yields a lower efficiency than the STA and UNA engines for cycle times dominated by τ_{adi}. At this mode of operation, the STA engine outperforms STÆ engine in terms of efficiency. However, for short cycle durations the STÆ engine results in a larger efficiency than the UNA engine. For a single cycle starting from the thermal state of the cold bath, the control costs for thermalization is larger than that of the compression and expansion strokes. In total, the control costs decline as we increase the time allocated for the isochoric and adiabatic branches. Our calculations show that for the UNA engine the parameter regime of the stroke time durations for which the power output and efficiency are negative greatly increases in its limit cycle as compared to only a single cycle of operation. For the CD-driven engines (both STA and STÆ), the power output remains positive throughout the stroke times considered in this study.

For limit cycle the STÆ engine displays a far more superior performance in terms of power output than the STA and UNA engines. The power for the STÆ engine in this mode of operation increases unlike the STA and UNA engines compared to the single cycle case. Our numerical calculations show that in the limit cycle, the efficiency vs cycle time is not necessarily monotonic for cycle time for the STÆ engine. This is of practical importance because it means that one can design an STÆ engine which has larger power output and efficiency compared to the STA engine. In its limit cycle, the thermalization cost dominates the control costs for the STÆ engine, specially for small time allocation for the isochoric branches. However, similar to the single cycle case, the costs decline as the cycle time is increases. Due to the generation of coherence and also diabatic population transfer, the costs in the limit cycle are larger than that of a single cycle, specially for shorter stroke durations. In addition to illuminating the fundamental potential and energetic cost limitations of finite-time quantum heat engines with shortcuts to adiabaticity and equilibration, our results can be significant for their practical implementations with optimum power and efficiency.

BIBLIOGRAPHY

[SAV, 1997] (1997). Oscillating anisotropies in a bacteriochlorophyll protein: Evidence for quantum beating between exciton levels. *Chemical Physics*, 223(2):303–312.

[YAN, 2002] (2002). Influence of phonons on exciton transfer dynamics: comparison of the redfield, förster, and modified redfield equations. *Chemical Physics*, 275(1):355–372. Photoprocesses in Multichromophoric Molecular Assemblies.

[TAO, 2020] (2020). Coherent and incoherent theories for photosynthetic energy transfer. *Science Bulletin*, 65(4):318–328.

[MAN, 2020] (2020). A decade with quantum coherence: How our past became classical and the future turned quantum. *Chemical Physics*, 532:110663.

[CIC, 2022] (2022). Quantum collision models: Open system dynamics from repeated interactions. *Physics Reports*, 954:1–70. Quantum collision models: Open system dynamics from repeated interactions.

[Abah and Lutz, 2018] Abah, O. and Lutz, E. (2018). Performance of shortcut-to-adiabaticity quantum engines. *Phys. Rev. E*, 98:032121.

[Abah and Paternostro, 2019] Abah, O. and Paternostro, M. (2019). Shortcut-to-adiabaticity otto engine: A twist to finite-time thermodynamics. *Phys. Rev. E*, 99:022110.

[Abah et al., 2020] Abah, O., Paternostro, M., and Lutz, E. (2020). Shortcut-to-adiabaticity quantum otto refrigerator. *Phys. Rev. Res.*, 2:023120.

[Abah et al., 2012] Abah, O., Roßnagel, J., Jacob, G., Deffner, S., Schmidt-Kaler, F., Singer, K., and Lutz, E. (2012). Single-ion heat engine at maximum power. *Phys. Rev. Lett.*, 109:203006.

[Abouraddy et al., 2002] Abouraddy, A. F., Toussaint, K. C., Sergienko, A. V., Saleh, B. E. A., and Teich, M. C. (2002). Entangled-photon ellipsometry. *J. Opt. Soc. Am. B*, 19(4):656–662.

[Adamson et al., 2007] Adamson, R. B. A., Shalm, L. K., Mitchell, M. W., and Steinberg, A. M. (2007). Multiparticle state tomography: Hidden differences. *Phys. Rev. Lett.*, 98:043601.

[Adesso et al., 2009] Adesso, G., Dell'Anno, F., De Siena, S., Illuminati, F., and Souza, L. A. M. (2009). Optimal estimation of losses at the ultimate quantum limit with non-gaussian states. *Phys. Rev. A*, 79:040305.

[Agarwalla et al., 2017] Agarwalla, B. K., Jiang, J.-H., and Segal, D. (2017). Quantum efficiency bound for continuous heat engines coupled to noncanonical reservoirs. *Phys. Rev. B*, 96:104304.

[Aiello et al., 2007] Aiello, A., Puentes, G., and Woerdman, J. P. (2007). Linear optics and quantum maps. *Phys. Rev. A*, 76:032323.

[Albarelli et al., 2018] Albarelli, F., Rossi, M. A. C., Tamascelli, D., and Genoni, M. G. (2018). Restoring Heisenberg scaling in noisy quantum metrology by monitoring the environment. *Quantum*, 2:110.

[Alicki, 1979] Alicki, R. (1979). The quantum open system as a model of the heat engine. 12(5):L103–L107.

[Alipour et al., 2020] Alipour, S., Chenu, A., Rezakhani, A. T., and del Campo, A. (2020). Shortcuts to Adiabaticity in Driven Open Quantum Systems: Balanced Gain and Loss and Non-Markovian Evolution. *Quantum*, 4:336.

[Alipour et al., 2014] Alipour, S., Mehboudi, M., and Rezakhani, A. T. (2014). Quantum metrology in open systems: Dissipative cramér-rao bound. *Phys. Rev. Lett.*, 112:120405.

[Alipour et al., 2022] Alipour, S., Rezakhani, A. T., Chenu, A., del Campo, A., and Ala-Nissila, T. (2022). Entropy-based formulation of thermodynamics in arbitrary quantum evolution. *Phys. Rev. A*, 105:L040201.

[Allahverdyan et al., 2008] Allahverdyan, A. E., Johal, R. S., and Mahler, G. (2008). Work extremum principle: Structure and function of quantum heat engines. *Phys. Rev. E*, 77:041118.

[Alodjants and Arakelian, 1999] Alodjants, A. P. and Arakelian, S. M. (1999). Quantum phase measurements and non-classical polarization states of light. *Journal of Modern Optics*, 46(3):475–507.

[Altepeter et al., 2005] Altepeter, J., Jeffrey, E., and Kwiat, P. (2005). Photonic state tomography. volume 52 of *Advances In Atomic, Molecular, and Optical Physics*, pages 105–159. Academic Press.

[Andreou and Kalayjian, 2002] Andreou, A. and Kalayjian, Z. (2002). Polarization imaging: principles and integrated polarimeters. *IEEE Sensors Journal*, 2(6):566–576.

[Arısoy et al., 2019] Arısoy, O., Campbell, S., and Müstecaplıoğlu, O. E. (2019). Thermalization of finite many-body systems by a collision model. *Entropy*, 21(12).

[Atkinson et al., 2021] Atkinson, G., Allen, E., Ferranti, G., McMillan, A., and Matthews, J. (2021). Quantum enhanced precision estimation of transmission with bright squeezed light. *Phys. Rev. Appl.*, 16:044031.

[Augusiak et al., 2016] Augusiak, R., Kołodyński, J., Streltsov, A., Bera, M. N., Acín, A., and Lewenstein, M. (2016). Asymptotic role of entanglement in quantum metrology. *Physical Review A*, 94(1):012339.

[Aulbach et al., 2010] Aulbach, M., Markham, D., and Murao, M. (2010). The maximally entangled symmetric state in terms of the geometric measure. *New Journal of Physics*, 12(7):073025.

[Azzam, 2016] Azzam, R. M. A. (2016). Stokes-vector and mueller-matrix polarimetry]. *J. Opt. Soc. Am. A*, 33(7):1396–1408.

[Baecklund, 2013] Baecklund, A. (2013). *Maximization of the Wehrl Entropy in Finite Dimensions*. Master of science thesis, KTH Royal Institute of Technology.

[Baecklund and Bengtsson, 2014] Baecklund, A. and Bengtsson, I. (2014). Four remarks on spin coherent states. *Physica Scripta*, 2014(T163):014012.

[Bagan et al., 2001] Bagan, E., Baig, M., and Muñoz Tapia, R. (2001). Aligning reference frames with quantum states. *Phys. Rev. Lett.*, 87:257903.

[Baguette et al., 2014] Baguette, D., Bastin, T., and Martin, J. (2014). Multiqubit symmetric states with maximally mixed one-qubit reductions. *Phys. Rev. A*, 90:032314.

[Bancelin et al., 2014] Bancelin, S., Nazac, A., Ibrahim, B. H., Dokládal, P., Decencière, E., Teig, B., Haddad, H., Fernandez, H., Schanne-Klein, M.-C., and Martino, A. D. (2014). Determination of collagen fiber orientation in histological slides using mueller microscopy and validation by second harmonic generation imaging. *Opt. Express*, 22(19):22561–22574.

[Bargmann, 1961] Bargmann, V. (1961). On a hilbert space of analytic functions and an associated integral transform part i. *Communications on Pure and Applied Mathematics*, 14(3):187–214.

[Barlow, 1956] Barlow, H. B. (1956). Retinal noise and absolute threshold. *J. Opt. Soc. Am.*, 46(8):634–639.

[Barnett, 2009] Barnett, S. M. (2009). *Quantum Information*. Oxford Master Series in Physics. Oxford University Press, London, England.

[Baylor et al., 1979a] Baylor, D. A., Lamb, T. D., and Yau, K. W. (1979a). The membrane current of single rod outer segments. *The Journal of Physiology*, 288(1):589–611.

[Baylor et al., 1979b] Baylor, D. A., Lamb, T. D., and Yau, K. W. (1979b). Responses of retinal rods to single photons. *The Journal of Physiology*, 288(1):613–634.

[Baylor et al., 1984] Baylor, D. A., Nunn, B. J., and Schnapf, J. L. (1984). The photocurrent, noise and spectral sensitivity of rods of the monkey macaca fascicularis. *The Journal of Physiology*, 357(1):575–607.

[Beau et al., 2016] Beau, M., Jaramillo, J., and Del Campo, A. (2016). Scaling-up quantum heat engines efficiently via shortcuts to adiabaticity. *Entropy*, 18(5).

[Belsley and Matthews, 2022] Belsley, A. and Matthews, J. C. F. (2022). Estimating the concentration of chiral media with bright squeezed light. *Applied Physics Letters*, 121(18):184001.

[Bengtsson and Zyczkowski, 2006] Bengtsson, I. and Zyczkowski, K. (2006). *Geometry of Quantum States: An Introduction to Quantum Entanglement*. Cambridge University Press.

[Bennett et al., 1993] Bennett, C. H., Brassard, G., Crépeau, C., Jozsa, R., Peres, A., and Wootters, W. K. (1993). Teleporting an unknown quantum state via dual classical and einstein-podolsky-rosen channels. *Phys. Rev. Lett.*, 70:1895–1899.

[Benoit et al., 2001] Benoit, A. M., Naoun, K., Louis-Dorr, V., Mala, L., and Raspiller, A. (2001). Linear dichroism of the retinal nerve fiber layer expressed with mueller matrices. *Appl. Opt.*, 40(4):565–569.

[Berchera and Degiovanni, 2019] Berchera, I. R. and Degiovanni, I. P. (2019). Quantum imaging with sub-poissonian light: challenges and perspectives in optical metrology. *Metrologia*, 56(2):024001.

[Berry et al., 2009] Berry, D. W., Higgins, B. L., Bartlett, S. D., Mitchell, M. W., Pryde, G. J., and Wiseman, H. M. (2009). How to perform the most accurate possible phase measurements. *Phys. Rev. A*, 80:052114.

[Berry, 2009] Berry, M. V. (2009). Transitionless quantum driving. *Journal of Physics A: Mathematical and Theoretical*, 42(36):365303.

[Besaga et al., 2023] Besaga, V. R., Zhang, L., Vega, A., Chauhan, P. S., Siefke, T., Steinlechner, F., Pertsch, T., Sukhorukov, A. A., and Setzpfandt, F. (2023). Non-local quantum differentiation between polarization objects using entanglement.

[Bialek, 2012] Bialek, W. (2012). *Biophysics: searching for principles.* Princeton University Press.

[Björk et al., 2010] Björk, G., Söderholm, J., Sánchez-Soto, L. L., Klimov, A. B., Ghiu, I., Marian, P., and Marian, T. A. (2010). Quantum degrees of polarization. *Optics Communications*, 283(22):4440–4447. Electromagnetic Coherence and Polarization.

[Blankenship, 2014] Blankenship, R. (2014). *Molecular Mechanisms of Photosynthesis.* Wiley.

[Bouchard et al., 2017] Bouchard, F., de la Hoz, P., Björk, G., Boyd, R. W., Grassl, M., Hradil, Z., Karimi, E., Klimov, A. B., Leuchs, G., Řeháček, J., and Sánchez-Soto, L. L. (2017). Quantum metrology at the limit with extremal majorana constellations. *Optica*, 4(11):1429–1432.

[Bouman, 2012] Bouman, M. A. (2012). *History and present status of quantum theory in vision.* Sensory Communication. The MIT Press.

[Bouton et al., 2021] Bouton, Q., Nettersheim, J., Burgardt, S., Adam, D., Lutz, E., and Widera, A. (2021). A quantum heat engine driven by atomic collisions. *Nature Communications*, 12(1):2063.

[Bouwmeester et al., 1997] Bouwmeester, D., Pan, J.-W., Mattle, K., Eibl, M., Weinfurter, H., and Zeilinger, A. (1997). Experimental quantum teleportation. *Nature*, 390(6660):575–579.

[Brambilla et al., 2008] Brambilla, E., Caspani, L., Jedrkiewicz, O., Lugiato, L. A., and Gatti, A. (2008). High-sensitivity imaging with multi-mode twin beams. *Phys. Rev. A*, 77:053807.

[Braunstein and Caves, 1994] Braunstein, S. L. and Caves, C. M. (1994). Statistical distance and the geometry of quantum states. *Phys. Rev. Lett.*, 72:3439–3443.

[Brendel et al., 1999] Brendel, J., Gisin, N., Tittel, W., and Zbinden, H. (1999). Pulsed energy-time entangled twin-photon source for quantum communication. *Phys. Rev. Lett.*, 82:2594–2597.

[Brunner et al., 2008] Brunner, N., Branciard, C., and Gisin, N. (2008). Possible entanglement detection with the naked eye. *Phys. Rev. A*, 78:052110.

[B.S et al., 2022] B.S, R., Mukherjee, V., and Divakaran, U. (2022). Bath engineering enhanced quantum critical engines. *Entropy*, 24(10).

[Bueno, 2000] Bueno, J. M. (2000). Measurement of parameters of polarization in the living human eye using imaging polarimetry. *Vision Research*, 40(28):3791–3799.

[Burnham and Weinberg, 1970] Burnham, D. C. and Weinberg, D. L. (1970). Observation of simultaneity in parametric production of optical photon pairs. *Phys. Rev. Lett.*, 25:84–87.

[Cable and Durkin, 2010] Cable, H. and Durkin, G. A. (2010). Parameter estimation with entangled photons produced by parametric down-conversion. *Phys. Rev. Lett.*, 105:013603.

[Çakmak, 2021] Çakmak, B. (2021). Finite-time two-spin quantum otto engines: Shortcuts to adiabaticity vs. irreversibility. *Turkish Journal of Physics*, 45(1):59–73.

[Calhoun et al., 2009] Calhoun, T. R., Ginsberg, N. S., Schlau-Cohen, G. S., Cheng, Y.-C., Ballottari, M., Bassi, R., and Fleming, G. R. (2009). Quantum coherence enabled determination of the energy landscape in light-harvesting complex ii. *The Journal of Physical Chemistry B*, 113(51):16291–16295.

[Campbell et al., 2019] Campbell, S., Çakmak, B., Müstecaplıoğlu, O. E., Paternostro, M., and Vacchini, B. (2019). Collisional unfolding of quantum darwinism. *Phys. Rev. A*, 99:042103.

[Campbell and Vacchini, 2021] Campbell, S. and Vacchini, B. (2021). Collision models in open system dynamics: A versatile tool for deeper insights? *Europhysics Letters*, 133(6):60001.

[Campisi and Fazio, 2016] Campisi, M. and Fazio, R. (2016). The power of a critical heat engine. *Nature Communications*, 7(1):11895.

[Campo and Boshier, 2012] Campo, A. d. and Boshier, M. G. (2012). Shortcuts to adiabaticity in a time-dependent box. *Scientific Reports*, 2(1):648.

[Campo et al., 2014] Campo, A. d., Goold, J., and Paternostro, M. (2014). More bang for your buck: Super-adiabatic quantum engines. *Scientific Reports*, 4(1):6208.

[Cao et al., 2020] Cao, J., Cogdell, R. J., Coker, D. F., Duan, H.-G., Hauer, J., Kleinekathöfer, U., Jansen, T. L. C., Mančal, T., Miller, R. J. D., Ogilvie,

J. P., Prokhorenko, V. I., Renger, T., Tan, H.-S., Tempelaar, R., Thorwart, M., Thyrhaug, E., Westenhoff, S., and Zigmantas, D. (2020). Quantum biology revisited. *Science Advances*, 6(14):eaaz4888.

[Cappellaro et al., 2005] Cappellaro, P., Emerson, J., Boulant, N., Ramanathan, C., Lloyd, S., and Cory, D. G. (2005). Entanglement assisted metrology. *Phys. Rev. Lett.*, 94:020502.

[Cario and Franck, 1922] Cario, G. and Franck, J. (1922). Über zerlegung von wasserstoffmolekülen durch angeregte quecksilberatome. *Zeitschrift für Physik*, 11(1):161–166.

[Carlo, 1922] Carlo, G. (1922). Über entstehung wahrer lichtabsorption und scheinbare koppelung von quantensprüngen. *Zeitschrift für Physik*, 10(1):185–199.

[Carnot et al.,] Carnot, S., Thurston, R. H., Carnot, R. H., and Kelvin, William Thomson, B. *Reflections on the motive power of heat and on machines fitted to develop that power.* New York :J. Wiley,. https://www.biodiversitylibrary.org/bibliography/17778.

[Cattaneo et al., 2021] Cattaneo, M., De Chiara, G., Maniscalco, S., Zambrini, R., and Giorgi, G. L. (2021). Collision models can efficiently simulate any multipartite markovian quantum dynamics. *Phys. Rev. Lett.*, 126:130403.

[Caves, 1981] Caves, C. M. (1981). Quantum-mechanical noise in an interferometer. *Phys. Rev. D*, 23:1693–1708.

[Çakmak et al., 2019] Çakmak, B., Campbell, S., Vacchini, B., Müstecaplıoğlu, O. E., and Paternostro, M. (2019). Robust multipartite entanglement generation via a collision model. *Phys. Rev. A*, 99:012319.

[Çakmak and Müstecaplıoğlu, 2019] Çakmak, B. and Müstecaplıoğlu, O. E. (2019). Spin quantum heat engines with shortcuts to adiabaticity. *Phys. Rev. E*, 99:032108.

[Çakmak et al., 2017] Çakmak, B., Pezzutto, M., Paternostro, M., and Müstecaplıoğlu, O. E. (2017). Non-markovianity, coherence, and system-environment correlations in a long-range collision model. *Phys. Rev. A*, 96:022109.

[Chang et al., 2023] Chang, S., Yang, J., Novoseltseva, A., Abdelhakeem, A., Hyman, M., Fu, X., Li, C., Chen, S.-C., Augustinack, J. C., Magnain, C., Fischl, B., Mckee, A. C., Boas, D. A., Chen, I. A., and Wang, H. (2023). Multi-scale label-free human brain imaging with integrated serial sectioning polarization sensitive optical coherence tomography and two-photon microscopy. *Advanced Science*, 10(35):2303381.

[Chen et al., 2017] Chen, F., Gao, Y., and Galperin, M. (2017). Molecular heat engines: Quantum coherence effects. *Entropy*, 19(9).

[Chen et al., 2010] Chen, X., Ruschhaupt, A., Schmidt, S., del Campo, A., Guéry-Odelin, D., and Muga, J. G. (2010). Fast optimal frictionless atom cooling in harmonic traps: Shortcut to adiabaticity. *Phys. Rev. Lett.*, 104:063002.

[Chen et al., 2011] Chen, X., Torrontegui, E., and Muga, J. G. (2011). Lewis-riesenfeld invariants and transitionless quantum driving. *Phys. Rev. A*, 83:062116.

[Chenu and Scholes, 2015] Chenu, A. and Scholes, G. D. (2015). Coherence in energy transfer and photosynthesis. *Annual Review of Physical Chemistry*, 66(1):69–96.

[Chiribella et al., 2004] Chiribella, G., D'Ariano, G. M., Perinotti, P., and Sacchi, M. F. (2004). Efficient use of quantum resources for the transmission of a reference frame. *Phys. Rev. Lett.*, 93:180503.

[Chisholm et al., 2021] Chisholm, D. A., García-Pérez, G., Rossi, M. A. C., Palma, G. M., and Maniscalco, S. (2021). Stochastic collision model approach to transport phenomena in quantum networks. *New Journal of Physics*, 23(3):033031.

[Chryssomalakos and Hernández-Coronado, 2017] Chryssomalakos, C. and Hernández-Coronado, H. (2017). Optimal quantum rotosensors. *Phys. Rev. A*, 95:052125.

[Ciccarello,] Ciccarello, F.

[Ciccarello et al., 2013] Ciccarello, F., Palma, G. M., and Giovannetti, V. (2013). Collision-model-based approach to non-markovian quantum dynamics. *Phys. Rev. A*, 87:040103.

[Collini et al., 2010] Collini, E., Wong, C. Y., Wilk, K. E., Curmi, P. M. G., Brumer, P., and Scholes, G. D. (2010). Coherently wired light-harvesting in photosynthetic marine algae at ambient temperature. *Nature*, 463(7281):644–647.

[Collins and Stephens, 2015] Collins, D. and Stephens, J. (2015). Depolarizing-channel parameter estimation using noisy initial states. *Phys. Rev. A*, 92:032324.

[Crowley et al., 2014] Crowley, P. J. D., Datta, A., Barbieri, M., and Walmsley, I. A. (2014). Tradeoff in simultaneous quantum-limited phase and loss estimation in interferometry. *Phys. Rev. A*, 89:023845.

[Curutchet and Mennucci, 2017] Curutchet, C. and Mennucci, B. (2017). Quantum chemical studies of light harvesting. *Chemical Reviews*, 117(2):294–343.

[Curzon and Ahlborn, 1975] Curzon, F. L. and Ahlborn, B. (1975). Efficiency of a carnot engine at maximum power output. *American Journal of Physics*, 43(1):22–24.

[Czekaj et al., 2015] Czekaj, Ł., Przysiężna, A., Horodecki, M., and Horodecki, P. (2015). Quantum metrology: Heisenberg limit with bound entanglement. *Physical Review A*, 92(6):062303.

[Czerwinski, 2021] Czerwinski, A. (2021). Quantum tomography of pure states with projective measurements distorted by experimental noise. *Acta Physica Polonica A*, 139(2):164–168.

[Czerwinski, 2022] Czerwinski, A. (2022). Entanglement characterization by single-photon counting with random noise. *Quantum Information and Computation*, 22(1 & 2):1–16.

[Danaci et al., 2021] Danaci, O., Lohani, S., Kirby, B. T., and Glasser, R. T. (2021). Machine learning pipeline for quantum state estimation with incomplete measurements. *Machine Learning: Science and Technology*, 2(3):035014.

[Dann and Kosloff, 2020] Dann, R. and Kosloff, R. (2020). Quantum signatures in the quantum carnot cycle. *New Journal of Physics*, 22(1):013055.

[Dann et al., 2018] Dann, R., Levy, A., and Kosloff, R. (2018). Time-dependent markovian quantum master equation. *Phys. Rev. A*, 98:052129.

[Dann et al., 2019] Dann, R., Tobalina, A., and Kosloff, R. (2019). Shortcut to equilibration of an open quantum system. *Phys. Rev. Lett.*, 122:250402.

[D'Ariano et al., 2003] D'Ariano, G. M., Paris, M. G. A., and Sacchi, M. F. (2003). Quantum tomography.

[Deffner et al., 2010] Deffner, S., Abah, O., and Lutz, E. (2010). Quantum work statistics of linear and nonlinear parametric oscillators. *Chemical Physics*, 375(2):200–208. Stochastic processes in Physics and Chemistry (in honor of Peter Hänggi).

[Deffner and Campbell, 2019] Deffner, S. and Campbell, S. (2019). *Quantum Thermodynamics*. 2053-2571. Morgan & Claypool Publishers.

[Deffner et al., 2014] Deffner, S., Jarzynski, C., and del Campo, A. (2014). Classical and quantum shortcuts to adiabaticity for scale-invariant driving. *Phys. Rev. X*, 4:021013.

[Deffner and Lutz, 2008] Deffner, S. and Lutz, E. (2008). Nonequilibrium work distribution of a quantum harmonic oscillator. *Phys. Rev. E*, 77:021128.

[del Campo, 2011] del Campo, A. (2011). Frictionless quantum quenches in ultracold gases: A quantum-dynamical microscope. *Phys. Rev. A*, 84:031606.

[del Campo et al., 2018] del Campo, A., Chenu, A., Deng, S., and Wu, H. (2018). *Friction-Free Quantum Machines*, pages 127–148. Springer International Publishing, Cham.

[Demirplak and Rice, 2003] Demirplak, M. and Rice, S. A. (2003). Adiabatic population transfer with control fields. *The Journal of Physical Chemistry A*, 107(46):9937–9945.

[Demirplak and Rice, 2005] Demirplak, M. and Rice, S. A. (2005). Assisted adiabatic passage revisited. *The Journal of Physical Chemistry B*, 109(14):6838–6844. PMID: 16851769.

[Demkowicz-Dobrzański and Maccone, 2014] Demkowicz-Dobrzański, R. and Maccone, L. (2014). Using entanglement against noise in quantum metrology. *Physical Review Letters*, 113(25):250801.

[Deng et al., 2003] Deng, F.-G., Long, G. L., and Liu, X.-S. (2003). Two-step quantum direct communication protocol using the einstein-podolsky-rosen pair block. *Phys. Rev. A*, 68:042317.

[Denis and Martin, 2022] Denis, J. and Martin, J. (2022). Extreme depolarization for any spin. *Phys. Rev. Res.*, 4:013178.

[Dodel et al., 2017] Dodel, A., Mayinda, A., Oudot, E., Martin, A., Sekatski, P., Bancal, J.-D., and Sangouard, N. (2017). Proposal for witnessing non-classical light with the human eye. *Quantum*, 1:7.

[Dowling, 2008] Dowling, J. P. (2008). Quantum optical metrology – the lowdown on high-n00n states. *Contemporary Physics*, 49(2):125–143.

[Dowling and Seshadreesan, 2015] Dowling, J. P. and Seshadreesan, K. P. (2015). Quantum optical technologies for metrology, sensing, and imaging. *Journal of Lightwave Technology*, 33(12):2359–2370.

[Duan et al., 2017] Duan, H.-G., Prokhorenko, V. I., Cogdell, R. J., Ashraf, K., Stevens, A. L., Thorwart, M., and Miller, R. J. D. (2017). Nature does not rely on long-lived electronic quantum coherence for photosynthetic energy transfer. *Proceedings of the National Academy of Sciences*, 114(32):8493–8498.

[Dupays et al., 2020] Dupays, L., Egusquiza, I. L., del Campo, A., and Chenu, A. (2020). Superadiabatic thermalization of a quantum oscillator by engineered dephasing. *Phys. Rev. Research*, 2:033178.

[Duysens, 1951] Duysens, L. N. M. (1951). Transfer of light energy within the pigment systems present in photosynthesizing cells. *Nature*, 168(4274):548–550.

[Engel et al., 2007] Engel, G. S., Calhoun, T. R., Read, E. L., Ahn, T.-K., Mančal, T., Cheng, Y.-C., Blankenship, R. E., and Fleming, G. R. (2007). Evidence for wavelike energy transfer through quantum coherence in photosynthetic systems. *Nature*, 446(7137):782–786.

[Engelsen et al., 2017] Engelsen, N. J., Krishnakumar, R., Hosten, O., and Kasevich, M. A. (2017). Bell correlations in spin-squeezed states of 500 000 atoms. *Phys. Rev. Lett.*, 118:140401.

[Eriksson et al., 2023] Eriksson, M., Goldberg, A., Hiekkamäki, M., Bouchard, F., Rehacek, J., Hradil, Z., Leuchs, G., Fickler, R., and Sánchez-Soto, L. (2023). Sensing rotations with multiplane light conversion. *Phys. Rev. Appl.*, 20:024052.

[Feldmann et al., 1996] Feldmann, T., Geva, E., Kosloff, R., and Salamon, P. (1996). Heat engines in finite time governed by master equations. *American Journal of Physics*, 64(4):485–492.

[Feldmann and Kosloff, 2003] Feldmann, T. and Kosloff, R. (2003). Quantum four-stroke heat engine: Thermodynamic observables in a model with intrinsic friction. *Phys. Rev. E*, 68:016101.

[Feldmann and Kosloff, 2004] Feldmann, T. and Kosloff, R. (2004). Characteristics of the limit cycle of a reciprocating quantum heat engine. *Phys. Rev. E*, 70:046110.

[Franck, 1922] Franck, J. (1922). Einige aus der theorie von klein und bosseland zu ziehende folgerungen über fluoreszenz, photochemische prozesse und die elektronenemission glühender körper. *Zeitschrift für Physik*, 9(1):259–266.

[Frey et al., 2011] Frey, M., Collins, D., and Gerlach, K. (2011). Probing the qudit depolarizing channel. *Journal of Physics A: Mathematical and Theoretical*, 44(20):205306.

[Frigerio, 1977] Frigerio, A. (1977). Quantum dynamical semigroups and approach to equilibrium. *Letters in Mathematical Physics*, 2(2):79–87.

[Frigerio, 1978] Frigerio, A. (1978). Stationary states of quantum dynamical semigroups. *Communications in Mathematical Physics*, 63(3):269–276.

[Funo et al., 2019] Funo, K., Lambert, N., Karimi, B., Pekola, J. P., Masuyama, Y., and Nori, F. (2019). Speeding up a quantum refrigerator via counterdiabatic driving. *Phys. Rev. B*, 100:035407.

[Furusawa et al., 1998] Furusawa, A., Sørensen, J. L., Braunstein, S. L., Fuchs, C. A., Kimble, H. J., and Polzik, E. S. (1998). Unconditional quantum teleportation. *Science*, 282(5389):706–709.

[Förster, 1946] Förster, T. (1946). Energiewanderung und fluoreszenz. *Naturwissenschaften*, 33(6):166–175.

[Förster, 1948] Förster, T. (1948). Zwischenmolekulare energiewanderung und fluoreszenz. *Annalen der Physik*, 437(1-2):55–75.

[Förster, 1959] Förster, T. (1959). 10th spiers memorial lecture. transfer mechanisms of electronic excitation. *Discuss. Faraday Soc.*, 27:7–17.

[Gallina et al., 2022] Gallina, F., Bruschi, M., and Fresch, B. (2022). Strategies to simulate dephasing-assisted quantum transport on digital quantum computers. *New Journal of Physics*, 24(2):023039.

[Gao, 2021] Gao, W. (2021). Mueller matrix decomposition methods for tissue polarization tomography. *Optics and Lasers in Engineering*, 147:106735.

[Gardiner, 1991] Gardiner, C. (1991). *Quantum Noise*, chapter 8, pages 257–258. Springer series in synergetics. Springer-Verlag, 2 edition.

[Gazeau, 2009] Gazeau, J. (2009). *Coherent States in Quantum Physics*. Wiley.

[Gelbwaser-Klimovsky and Kurizki, 2014] Gelbwaser-Klimovsky, D. and Kurizki, G. (2014). Heat-machine control by quantum-state preparation: From quantum engines to refrigerators. *Phys. Rev. E*, 90:022102.

[Gerry and Knight, 2004] Gerry, C. and Knight, P. (2004). *Introductory quantum optics*. Cambridge University Press.

[Geva and Kosloff, 1992] Geva, E. and Kosloff, R. (1992). A quantum-mechanical heat engine operating in finite time. a model consisting of spin-1/2 systems as the working fluid. *The Journal of Chemical Physics*, 96(4):3054–3067.

[Geva and Kosloff, 1996] Geva, E. and Kosloff, R. (1996). The quantum heat engine and heat pump: An irreversible thermodynamic analysis of the three-level amplifier. *The Journal of Chemical Physics*, 104(19):7681–7699.

[Ghosh and Vitkin, 2011] Ghosh, N. and Vitkin, A. I. (2011). Tissue polarimetry: concepts, challenges, applications, and outlook. *Journal of Biomedical Optics*, 16(11):110801.

[Ghosh et al., 2009] Ghosh, N., Wood, M. F. G., Li, S.-h., Weisel, R. D., Wilson, B. C., Li, R.-K., and Vitkin, I. A. (2009). Mueller matrix decomposition for polarized light assessment of biological tissues. *Journal of Biophotonics*, 2(3):145–156.

[Gil et al., 2013] Gil, J. J., José, I. S., and Ossikovski, R. (2013). Serial-parallel decompositions of mueller matrices. *J. Opt. Soc. Am. A*, 30(1):32–50.

[Giovannetti et al., 2004] Giovannetti, V., Lloyd, S., and Maccone, L. (2004). Quantum-enhanced measurements: Beating the standard quantum limit. *Science*, 306(5700):1330–1336.

[Giovannetti et al., 2006] Giovannetti, V., Lloyd, S., and Maccone, L. (2006). Quantum metrology. *Phys. Rev. Lett.*, 96:010401.

[Giraud et al., 2015] Giraud, O., Braun, D., Baguette, D., Bastin, T., and Martin, J. (2015). Tensor representation of spin states. *Phys. Rev. Lett.*, 114:080401.

[Giraud et al., 2010] Giraud, O., Braun, P., and Braun, D. (2010). Quantifying quantumness and the quest for queens of quantum. *New Journal of Physics*, 12(6):063005.

[Glorot et al., 2011] Glorot, X., Bordes, A., and Bengio, Y. (2011). Deep sparse rectifier neural networks. In Gordon, G., Dunson, D., and Dudík, M., editors, *Proceedings of the Fourteenth International Conference on Artificial Intelligence and Statistics*, volume 15 of *Proceedings of Machine Learning Research*, pages 315–323, Fort Lauderdale, FL, USA. PMLR.

[Goldberg, 2020] Goldberg, A. Z. (2020). Quantum theory of polarimetry: From quantum operations to mueller matrices. *Phys. Rev. Res.*, 2:023038.

[Goldberg, 2021] Goldberg, A. Z. (2021). *Disquisitions on Quantum-Enhanced Polarimetry*. PhD thesis.

[Goldberg, 2022a] Goldberg, A. Z. (2022a). Chapter three - quantum polarimetry. volume 67 of *Progress in Optics*, pages 185–274. Elsevier.

[Goldberg, 2022b] Goldberg, A. Z. (2022b). Quantum polarimetry. volume 67 of *Progress in Optics*, pages 185–274. Elsevier.

[Goldberg et al., 2021a] Goldberg, A. Z., de la Hoz, P., Björk, G., Klimov, A. B., Grassl, M., Leuchs, G., and Sánchez-Soto, L. L. (2021a). Quantum concepts in optical polarization. *Adv. Opt. Photon.*, 13(1):1–73.

[Goldberg and James, 2018] Goldberg, A. Z. and James, D. F. V. (2018). Quantum-limited euler angle measurements using anticoherent states. *Phys. Rev. A*, 98:032113.

[Goldberg et al., 2020] Goldberg, A. Z., Klimov, A. B., Grassl, M., Leuchs, G., and Sánchez-Soto, L. L. (2020). Extremal quantum states. *AVS Quantum Science*, 2(4):044701.

[Goldberg et al., 2021b] Goldberg, A. Z., Klimov, A. B., Leuchs, G., and Sánchez-Soto, L. L. (2021b). Rotation sensing at the ultimate limit. *Journal of Physics: Photonics*, 3(2):022008.

[Goldberg et al., 2023] Goldberg, A. Z., Steinberg, A. M., and Heshami, K. (2023). Beyond transcoherent states: Field states for effecting optimal coherent rotations on single or multiple qubits. *Quantum*, 7:963.

[Gramatikov, 2014] Gramatikov, B. I. (2014). Modern technologies for retinal scanning and imaging: an introduction for the biomedical engineer. *BioMedical Engineering OnLine*, 13(1):52.

[Griffiths, 2008] Griffiths, D. J. (2008). *Introduction to elementary particles.* John Wiley and Sons, 2 edition.

[Grimmett and Stirzaker, 2020] Grimmett, G. and Stirzaker, D. (2020). *Probability and random processes.* Oxford University Press.

[Guéry-Odelin et al., 2019] Guéry-Odelin, D., Ruschhaupt, A., Kiely, A., Torrontegui, E., Martínez-Garaot, S., and Muga, J. G. (2019). Shortcuts to adiabaticity: Concepts, methods, and applications. *Rev. Mod. Phys.*, 91:045001.

[Hall, 1994] Hall, B. (1994). The segal-bargmann ”coherent state” transform for compact lie groups. *Journal of Functional Analysis*, 122(1):103–151.

[Hannonen et al., 2020] Hannonen, A., Hoenders, B. J., Elsässer, W., Friberg, A. T., and Setälä, T. (2020). Ghost polarimetry using stokes correlations. *J. Opt. Soc. Am. A*, 37(5):714–719.

[Hardal et al., 2017] Hardal, A. U. C., Aslan, N., Wilson, C. M., and Müstecaplıoğlu, O. E. (2017). Quantum heat engine with coupled superconducting resonators. *Phys. Rev. E*, 96:062120.

[Hardal and Müstecaplıoğlu, 2015] Hardal, A. Ü. C. and Müstecaplıoğlu, Ö. E. (2015). Superradiant quantum heat engine. *Scientific Reports*, 5(1):12953.

[Hartmann et al., 2020] Hartmann, A., Mukherjee, V., Niedenzu, W., and Lechner, W. (2020). Many-body quantum heat engines with shortcuts to adiabaticity. *Phys. Rev. Res.*, 2:023145.

[Harush and Dubi, 2021] Harush, E. Z. and Dubi, Y. (2021). Do photosynthetic complexes use quantum coherence to increase their efficiency? probably not. *Science Advances*, 7(8):eabc4631.

[Hayat et al., 1999] Hayat, M. M., Joobeur, A., and Saleh, B. E. A. (1999). Reduction of quantum noise in transmittance estimation using photon-correlated beams. *J. Opt. Soc. Am. A*, 16(2):348–358.

[He et al., 2021a] He, C., He, H., Chang, J., Chen, B., Ma, H., and Booth, M. J. (2021a). Polarisation optics for biomedical and clinical applications: a review. *Light: Science & Applications*, 10(1):194.

[He et al., 2021b] He, C., He, H., Chang, J., Chen, B., Ma, H., and Booth, M. J. (2021b). Polarisation optics for biomedical and clinical applications: a review. *Light: Science & Applications*, 10(1):194.

[Hecht, 2017] Hecht, E. (2017). *Optics*. Pearson Education, Incorporated.

[Hecht et al., 1942] Hecht, S., Shlaer, S., and Pirenne, M. H. (1942). Energy, quanta, and vision . *Journal of General Physiology*, 25(6):819–840.

[Heidmann et al., 1987] Heidmann, A., Horowicz, R. J., Reynaud, S., Giacobino, E., Fabre, C., and Camy, G. (1987). Observation of quantum noise reduction on twin laser beams. *Phys. Rev. Lett.*, 59:2555–2557.

[Helstrom, 1967] Helstrom, C. (1967). Minimum mean-squared error of estimates in quantum statistics. *Physics Letters A*, 25(2):101–102.

[Helstrom, 1968] Helstrom, C. (1968). The minimum variance of estimates in quantum signal detection. *IEEE Transactions on Information Theory*, 14(2):234–242.

[Helstrom, 1969] Helstrom, C. W. (1969). Quantum detection and estimation theory. *Journal of Statistical Physics*, 1(2):231–252.

[Holmes, 2017] Holmes, R. (2017). *Testing the limits of human vision with quantum states of light*. PhD thesis, University of Illinois at Urbana-Champaign.

[Holmes et al., 2017] Holmes, R., Victora, M., Wang, R. F., and Kwiat, P. G. (2017). Measuring temporal summation in visual detection with a single-photon source. *Vision Research*, 140:33 – 43.

[Hong and Mandel, 1985] Hong, C. K. and Mandel, L. (1985). Theory of parametric frequency down conversion of light. *Phys. Rev. A*, 31:2409–2418.

[Hong et al., 1987] Hong, C. K., Ou, Z. Y., and Mandel, L. (1987). Measurement of subpicosecond time intervals between two photons by interference. *Phys. Rev. Lett.*, 59:2044–2046.

[Horn and Jennewein, 2019] Horn, R. and Jennewein, T. (2019). Auto-balancing and robust interferometer designs for polarization entangled photon sources. *Opt. Express*, 27(12):17369–17376.

[Hossein-Nejad et al., 2012] Hossein-Nejad, H., Olaya-Castro, A., and Scholes, G. D. (2012). Phonon-mediated path-interference in electronic energy transfer. *The Journal of Chemical Physics*, 136(2):024112.

[Hotta et al., 2005] Hotta, M., Karasawa, T., and Ozawa, M. (2005). Ancilla-assisted enhancement of channel estimation for low-noise parameters. *Phys. Rev. A*, 72:052334.

[Hu et al., 1997] Hu, X., Ritz, T., Damjanović, A., and Schulten, K. (1997). Pigment organization and transfer of electronic excitation in the photosynthetic unit of purple bacteria. *The Journal of Physical Chemistry B*, 101(19):3854–3871.

[Huang and Zeng, 2020] Huang, P. and Zeng, G. (2020). Entanglement transmission through dense scattering medium. *New Journal of Physics*, 22(5):053021.

[Huang and Knighton, 2003] Huang, X.-R. and Knighton, R. W. (2003). Theoretical model of the polarization properties of the retinal nerve fiber layer in reflection. *Appl. Opt.*, 42(28):5726–5736.

[Huang et al., 2016] Huang, Z., Macchiavello, C., and Maccone, L. (2016). Usefulness of entanglement-assisted quantum metrology. *Phys. Rev. A*, 94:012101.

[Hübener et al., 2009] Hübener, R., Kleinmann, M., Wei, T.-C., González-Guillén, C., and Gühne, O. (2009). Geometric measure of entanglement for symmetric states. *Phys. Rev. A*, 80:032324.

[Humphrey et al., 2002] Humphrey, T. E., Newbury, R., Taylor, R. P., and Linke, H. (2002). Reversible quantum brownian heat engines for electrons. *Phys. Rev. Lett.*, 89:116801.

[Insinga et al., 2018] Insinga, A., Andresen, B., Salamon, P., and Kosloff, R. (2018). Quantum heat engines: Limit cycles and exceptional points. *Phys. Rev. E*, 97:062153.

[Ioannou et al., 2021] Ioannou, C., Nair, R., Fernandez-Corbaton, I., Gu, M., Rockstuhl, C., and Lee, C. (2021). Optimal circular dichroism sensing with quantum light: Multiparameter estimation approach. *Phys. Rev. A*, 104:052615.

[Ishizaki and Fleming, 2009a] Ishizaki, A. and Fleming, G. R. (2009a). On the adequacy of the redfield equation and related approaches to the study of quantum dynamics in electronic energy transfer. *The Journal of Chemical Physics*, 130(23):234110.

[Ishizaki and Fleming, 2009b] Ishizaki, A. and Fleming, G. R. (2009b). Unified treatment of quantum coherent and incoherent hopping dynamics in electronic energy transfer: Reduced hierarchy equation approach. *The Journal of Chemical Physics*, 130(23):234111.

[Iskhakov et al., 2011] Iskhakov, T. S., Agafonov, I. N., Chekhova, M. V., Rytikov, G. O., and Leuchs, G. (2011). Polarization properties of macroscopic bell states. *Phys. Rev. A*, 84:045804.

[Israel et al., 2012] Israel, Y., Afek, I., Rosen, S., Ambar, O., and Silberberg, Y. (2012). Experimental tomography of noon states with large photon numbers. *Phys. Rev. A*, 85:022115.

[Israel et al., 2014a] Israel, Y., Rosen, S., and Silberberg, Y. (2014a). Supersensitive polarization microscopy using noon states of light. *Phys. Rev. Lett.*, 112:103604.

[Israel et al., 2014b] Israel, Y., Rosen, S., and Silberberg, Y. (2014b). Supersensitive polarization microscopy using noon states of light. *Phys. Rev. Lett.*, 112:103604.

[Jakeman and Rarity, 1986] Jakeman, E. and Rarity, J. (1986). The use of pair production processes to reduce quantum noise in transmission measurements. *Optics Communications*, 59(3):219–223.

[James et al., 2001] James, D. F. V., Kwiat, P. G., Munro, W. J., and White, A. G. (2001). Measurement of qubits. *Phys. Rev. A*, 64:052312.

[Jang, 2009] Jang, S. (2009). Theory of coherent resonance energy transfer for coherent initial condition. *The Journal of Chemical Physics*, 131(16):164101.

[Jang, 2011] Jang, S. (2011). Theory of multichromophoric coherent resonance energy transfer: A polaronic quantum master equation approach. *The Journal of Chemical Physics*, 135(3):034105.

[Jarzyna, 2021] Jarzyna, M. (2021). Quantum limits to polarization measurement of classical light.

[Ji et al., 2008] Ji, Z., Wang, G., Duan, R., Feng, Y., and Ying, M. (2008). Parameter estimation of quantum channels. *IEEE Transactions on Information Theory*, 54(11):5172–5185.

[Johansson et al., 2012a] Johansson, J., Nation, P., and Nori, F. (2012a). Qutip: An open-source python framework for the dynamics of open quantum systems. *Computer Physics Communications*, 183(8):1760–1772.

[Johansson et al., 2013] Johansson, J., Nation, P., and Nori, F. (2013). Qutip 2: A python framework for the dynamics of open quantum systems. *Computer Physics Communications*, 184(4):1234–1240.

[Johansson et al., 2012b] Johansson, J. R., Nation, P. D., and Nori, F. (2012b). Qutip: An open-source python framework for the dynamics of open quantum systems. *Computer Physics Communications*, 183:1760–1772.

[Jones, 2003] Jones, D. K. (2003). Determining and visualizing uncertainty in estimates of fiber orientation from diffusion tensor mri. *Magnetic Resonance in Medicine*, 49(1):7–12.

[Kakitani et al., 1999] Kakitani, T., Kimura, A., and Sumi, H. (1999). Theory of excitation transfer in the intermediate coupling case. *The Journal of Physical Chemistry B*, 103(18):3720–3726.

[Kaminsky et al., 2004] Kaminsky, W., Claborn, K., and Kahr, B. (2004). Polarimetric imaging of crystals. *Chem. Soc. Rev.*, 33:514–525.

[Kassal et al., 2013] Kassal, I., Yuen-Zhou, J., and Rahimi-Keshari, S. (2013). Does coherence enhance transport in photosynthesis? *The Journal of Physical Chemistry Letters*, 4(3):362–367.

[Kenkre and Knox, 1974] Kenkre, V. M. and Knox, R. S. (1974). Generalized-master-equation theory of excitation transfer. *Phys. Rev. B*, 9:5279–5290.

[Kessler et al., 2014] Kessler, E. M., Lovchinsky, I., Sushkov, A. O., and Lukin, M. D. (2014). Quantum error correction for metrology. *Phys. Rev. Lett.*, 112:150802.

[Kieu, 2004] Kieu, T. D. (2004). The second law, maxwell's demon, and work derivable from quantum heat engines. *Phys. Rev. Lett.*, 93:140403.

[Killoran et al., 2015] Killoran, N., Huelga, S. F., and Plenio, M. B. (2015). Enhancing light-harvesting power with coherent vibrational interactions: A quantum heat engine picture. *The Journal of Chemical Physics*, 143(15):155102.

[Kim et al., 2016] Kim, J., Sangjun, O., Kim, Y., and Lee, M. (2016). Convolutional neural network with niologically inspired retinal structure. *Procedia Computer Science*, 88:145–154. 7th Annual International Conference on Biologically Inspired Cognitive Architectures, BICA 2016, held July 16 to July 19, 2016 in New York City, NY, USA.

[Kim et al., 2022] Kim, M., Scully, M., and Svidzinsky, A. (2022). A supercharged photonic quantum heat engine. *Nature Photonics*, 16(10):669–670.

[Kimble, 2008] Kimble, H. J. (2008). The quantum internet. *Nature*, 453(7198):1023–1030.

[Kimura, 2009] Kimura, A. (2009). General theory of excitation energy transfer in donor-mediator-acceptor systems. *The Journal of Chemical Physics*, 130(15):154103.

[Kimura and Kakitani, 2007] Kimura, A. and Kakitani, T. (2007). Advanced theory of excitation energy transfer in dimers. *The Journal of Physical Chemistry A*, 111(47):12042–12048.

[Kimura et al., 2000] Kimura, A., Kakitani, T., and Yamato, T. (2000). Theory of excitation energy transfer in the intermediate coupling case. ii. criterion for intermediate coupling excitation energy transfer mechanism and application to the photosynthetic antenna system. *The Journal of Physical Chemistry B*, 104(39):9276–9287.

[Klatzow et al., 2019] Klatzow, J., Becker, J. N., Ledingham, P. M., Weinzetl, C., Kaczmarek, K. T., Saunders, D. J., Nunn, J., Walmsley, I. A., Uzdin, R., and Poem, E. (2019). Experimental demonstration of quantum effects in the operation of microscopic heat engines. *Phys. Rev. Lett.*, 122:110601.

[Klimov et al., 2010] Klimov, A. B., Björk, G., Söderholm, J., Madsen, L. S., Lassen, M., Andersen, U. L., Heersink, J., Dong, R., Marquardt, C., Leuchs, G., and Sánchez-Soto, L. L. (2010). Assessing the polarization of a quantum field from stokes fluctuations. *Phys. Rev. Lett.*, 105:153602.

[Klimov et al., 2006] Klimov, A. B., Romero, J. L., and Sánchez-Soto, L. L. (2006). Simple quantum model for light depolarization. *J. Opt. Soc. Am. B*, 23(1):126–133.

[Klimov et al., 2008] Klimov, A. B., Romero, J. L., Sánchez-Soto, L. L., Messina, A., and Napoli, A. (2008). Quantum light depolarization: The phase-space perspective. *Phys. Rev. A*, 77:033853.

[Klimov et al., 2005] Klimov, A. B., Sánchez-Soto, L. L., Yustas, E. C., Söderholm, J., and Björk, G. (2005). Distance-based degrees of polarization for a quantum field. *Phys. Rev. A*, 72:033813.

[Klyshko, 1992] Klyshko, D. (1992). Multiphoton interference and polarization effects. *Physics Letters A*, 163(5):349–355.

[Knighton et al., 2002] Knighton, R. W., Huang, X.-R., and Greenfield, D. S. (2002). Analytical Model of Scanning Laser Polarimetry for Retinal Nerve Fiber Layer Assessment. *Investigative Ophthalmology & Visual Science*, 43(2):383–392.

[Kok et al., 2007] Kok, P., Munro, W. J., Nemoto, K., Ralph, T. C., Dowling, J. P., and Milburn, G. J. (2007). Linear optical quantum computing with photonic qubits. *Rev. Mod. Phys.*, 79:135–174.

[Kolenderski and Demkowicz-Dobrzanski, 2008] Kolenderski, P. and Demkowicz-Dobrzanski, R. (2008). Optimal state for keeping reference frames aligned and the platonic solids. *Phys. Rev. A*, 78:052333.

[Koochakie et al., 2021] Koochakie, M. M. R., Jannesary, V., and Karimipour, V. (2021). Ghz states as near-optimal states for reference frame alignment. *Quantum Information Processing*, 20(10):329.

[Köse et al., 2019] Köse, E., Çakmak, S., Gençten, A., Kominis, I. K., and Müstecaplıoğlu, O. E. (2019). Algorithmic quantum heat engines. *Phys. Rev. E*, 100:012109.

[Kosloff, 1984] Kosloff, R. (1984). A quantum mechanical open system as a model of a heat engine. *The Journal of Chemical Physics*, 80(4):1625–1631.

[Kosloff and Feldmann, 2002] Kosloff, R. and Feldmann, T. (2002). Discrete four-stroke quantum heat engine exploring the origin of friction. *Phys. Rev. E*, 65:055102.

[Kosloff and Levy, 2014] Kosloff, R. and Levy, A. (2014). Quantum heat engines and refrigerators: Continuous devices. *Annual Review of Physical Chemistry*, 65(1):365–393. PMID: 24689798.

[Kosloff and Rezek, 2017] Kosloff, R. and Rezek, Y. (2017). The quantum harmonic otto cycle. *Entropy*, 19:136.

[Kothe et al., 2013] Kothe, C., Madsen, L. S., Andersen, U. L., and Björk, G. (2013). Experimental determination of the degree of polarization of quantum states. *Phys. Rev. A*, 87:043814.

[Kozyrev, 2019] Kozyrev, S. V. (2019). Model of vibrons in quantum photosynthesis as an analog of a model of laser. *Proceedings of the Steklov Institute of Mathematics*, 306(1):145–156.

[Kurizki and Kofman, 2022] Kurizki, G. and Kofman, A. G. (2022). *Thermodynamics and Control of Open Quantum Systems*. Cambridge University Press.

[Kuzmich and Mandel, 1998] Kuzmich, A. and Mandel, L. (1998). Sub-shot-noise interferometric measurements with two-photon states. *Quantum and Semiclassical Optics: Journal of the European Optical Society Part B*, 10(3):493.

[Langley, 1889] Langley, S. (1889). I. energy and vision. *The London, Edinburgh, and Dublin Philosophical Magazine and Journal of Science*, 27(164):1–23.

[Lee, 1988] Lee, C. T. (1988). Wehrl's entropy of spin states and lieb's conjecture. *Journal of Physics A: Mathematical and General*, 21(19):3749.

[Leegwater, 1996] Leegwater, J. A. (1996). Coherent versus incoherent energy transfer and trapping in photosynthetic antenna complexes. *The Journal of Physical Chemistry*, 100(34):14403–14409.

[Levi et al., 2016] Levi, E. K., Irish, E. K., and Lovett, B. W. (2016). Coherent exciton dynamics in a dissipative environment maintained by an off-resonant vibrational mode. *Phys. Rev. A*, 93:042109.

[Li et al., 2022] Li, J., Sherman, E. Y., and Ruschhaupt, A. (2022). Quantum heat engine based on a spin-orbit- and zeeman-coupled bose-einstein condensate. *Phys. Rev. A*, 106:L030201.

[Li et al., 2021] Li, L., Li, H., Yu, W., Hao, Y., Li, L., and Zou, J. (2021). Shortcut-to-adiabaticity quantum tripartite otto cycle. *Journal of Physics B: Atomic, Molecular and Optical Physics*, 54(21):215501.

[Li and Li, 2021] Li, Y. and Li, L. (2021). Hierarchical-environment-assisted non-markovian and its effect on thermodynamic properties. *EPJ Quantum Technology*, 8(1):9.

[Lieb, 1978] Lieb, E. H. (1978). Proof of an entropy conjecture of wehrl. *Communications in Mathematical Physics*, 62(1):35–41.

[Lieb and Solovej, 2014] Lieb, E. H. and Solovej, J. P. (2014). Proof of an entropy conjecture for Bloch coherent spin states and its generalizations. *Acta Mathematica*, 212(2):379 – 398.

[Lindblad, 1975] Lindblad, G. (1975). Completely positive maps and entropy inequalities. *Communications in Mathematical Physics*, 40(2):147–151.

[Lisboa et al., 2022] Lisboa, V. F., Dieguez, P. R., Guimarães, J. R., Santos, J. F. G., and Serra, R. M. (2022). Experimental investigation of a quantum heat engine powered by generalized measurements. *Phys. Rev. A*, 106:022436.

[Liu and Fu, 2016] Liu, H. D. and Fu, L. B. (2016). Berry phase and quantum entanglement in majorana's stellar representation. *Phys. Rev. A*, 94:022123.

[Lohani et al., 2020] Lohani, S., Kirby, B. T., Brodsky, M., Danaci, O., and Glasser, R. T. (2020). Machine learning assisted quantum state estimation. *Machine Learning: Science and Technology*, 1(3):035007.

[Long and Liu, 2002] Long, G. L. and Liu, X. S. (2002). Theoretically efficient high-capacity quantum-key-distribution scheme. *Phys. Rev. A*, 65:032302.

[Long et al., 2022] Long, X., He, W.-T., Zhang, N.-N., Tang, K., Lin, Z., Liu, H., Nie, X., Feng, G., Li, J., Xin, T., Ai, Q., and Lu, D. (2022). Entanglement-enhanced quantum metrology in colored noise by quantum zeno effect. *Phys. Rev. Lett.*, 129:070502.

[Lorenzo et al., 2017a] Lorenzo, S., Ciccarello, F., and Palma, G. M. (2017a). Composite quantum collision models. *Phys. Rev. A*, 96:032107.

[Lorenzo et al., 2017b] Lorenzo, S., Ciccarello, F., Palma, G. M., and Vacchini, B. (2017b). Quantum non-markovian piecewise dynamics from collision models. *Open Systems & Information Dynamics*, 24(04):1740011.

[Losero et al., 2018] Losero, E., Ruo-Berchera, I., Meda, A., Avella, A., and Genovese, M. (2018). Unbiased estimation of an optical loss at the ultimate quantum limit with twin-beams. *Scientific Reports*, 8(1):7431.

[Losurdo et al., 2009] Losurdo, M., Bergmair, M., Bruno, G., Cattelan, D., Cobet, C., de Martino, A., Fleischer, K., Dohcevic-Mitrovic, Z., Esser, N., Galliet, M., Gajic, R., Hemzal, D., Hingerl, K., Humlicek, J., Ossikovski, R., Popovic, Z. V., and Saxl, O. (2009). Spectroscopic ellipsometry and polarimetry for materials and systems analysis at the nanometer scale: state-of-the-art, potential, and perspectives. *Journal of Nanoparticle Research*, 11(7):1521–1554.

[Loudon, 2000] Loudon, R. (2000). *The Quantum Theory of Light*, chapter 6, pages 271–278. Oxford University Press, 3 edition.

[Loulakis et al., 2017] Loulakis, M., Blatsios, G., Vrettou, C. S., and Kominis, I. K. (2017). Quantum biometrics with retinal photon counting. *Phys. Rev. Applied*, 8:044012.

[Lozano et al., 2018] Lozano, A., Soto-Sánchez, C., Garrigós, J., Martínez, J. J., Ferrández, J. M., and Fernández, E. (2018). A 3d convolutional neural network to model retinal ganglion cell's responses to light patterns in mice. *International Journal of Neural Systems*, 28(10):1850043. PMID: 30556459.

[Lu and Chipman, 1996a] Lu, S.-Y. and Chipman, R. A. (1996a). Interpretation of mueller matrices based on polar decomposition. *J. Opt. Soc. Am. A*, 13(5):1106–1113.

[Lu and Chipman, 1996b] Lu, S.-Y. and Chipman, R. A. (1996b). Interpretation of mueller matrices based on polar decomposition. *J. Opt. Soc. Am. A*, 13(5):1106–1113.

[Luis, 2002] Luis, A. (2002). Degree of polarization in quantum optics. *Phys. Rev. A*, 66:013806.

[Luis, 2005] Luis, A. (2005). Quantum polarization for three-dimensional fields via stokes operators. *Phys. Rev. A*, 71:023810.

[Luis, 2007a] Luis, A. (2007a). Degree of polarization of type-ii unpolarized light. *Phys. Rev. A*, 75:053806.

[Luis, 2007b] Luis, A. (2007b). Polarization distributions and degree of polarization for quantum gaussian light fields. *Optics Communications*, 273(1):173–181.

[Luis, 2016] Luis, A. (2016). Chapter five - polarization in quantum optics. volume 61 of *Progress in Optics*, pages 283–331. Elsevier.

[Luis and Sánchez-Soto, 1993] Luis, A. and Sánchez-Soto, L. L. (1993). Phase-difference operator. *Phys. Rev. A*, 48:4702–4708.

[Lum et al., 2021] Lum, D. J., Mazurek, M. D., Mikhaylov, A., Parzuchowski, K. M., Wilson, R. N., Jimenez, R., Gerrits, T., Stevens, M. J., Cicerone, M. T., and Camp, C. H. (2021). Witnessing the survival of time-energy entanglement through biological tissue and scattering media. *Biomed. Opt. Express*, 12(6):3658–3670.

[Luo et al., 2023] Luo, W., Cao, L., Shi, Y., Wan, L., Zhang, H., Li, S., Chen, G., Li, Y., Li, S., Wang, Y., Sun, S., Karim, M. F., Cai, H., Kwek, L. C., and Liu, A. Q. (2023). Recent progress in quantum photonic chips for quantum communication and internet. *Light: Science & Applications*, 12(1):175.

[Ma et al., 2011] Ma, J., Wang, X., Sun, C., and Nori, F. (2011). Quantum spin squeezing. *Physics Reports*, 509(2):89–165.

[Magnitskiy et al., 2020] Magnitskiy, S., Agapov, D., and Chirkin, A. (2020). Ghost polarimetry with unpolarized pseudo-thermal light. *Opt. Lett.*, 45(13):3641–3644.

[Magnitskiy et al., 2022] Magnitskiy, S., Agapov, D., and Chirkin, A. (2022). Quantum ghost polarimetry with entangled photons. *Opt. Lett.*, 47(4):754–757.

[Magnitskiy et al., 2021] Magnitskiy, S. A., Agapov, D. P., Belovolov, I. A., Gostev, P. P., Frolovtsev, D. N., and Chirkin, A. S. (2021). Ghost polarimetry in classical and quantum light. *Moscow University Physics Bulletin*, 76(6):424–439.

[Majorana, 1932] Majorana, E. (1932). Atomi orientati in campo magnetico variabile. *Il Nuovo Cimento (1924-1942)*, 9(2):43–50.

[Mamani et al., 2018] Mamani, S., Shi, L., Ahmed, T., Karnik, R., Rodríguez-Contreras, A., Nolan, D., and Alfano, R. (2018). Transmission of classically entangled beams through mouse brain tissue. *Journal of Biophotonics*, 11(12):e201800096.

[Martin et al., 2020] Martin, J., Weigert, S., and Giraud, O. (2020). Optimal Detection of Rotations about Unknown Axes by Coherent and Anticoherent States. *Quantum*, 4:285.

[Masuda and Nakamura, 2010] Masuda, S. and Nakamura, K. (2010). Fast-forward of adiabatic dynamics in quantum mechanics. *Proceedings of the Royal Society A: Mathematical, Physical and Engineering Sciences*, 466(2116):1135–1154.

[Masuda and Nakamura, 2011] Masuda, S. and Nakamura, K. (2011). Acceleration of adiabatic quantum dynamics in electromagnetic fields. *Phys. Rev. A*, 84:043434.

[Mattiotti et al., 2021] Mattiotti, F., Brown, W. M., Piovella, N., Olivares, S., Gauger, E. M., and Celardo, G. L. (2021). Bio-inspired natural sunlight-pumped lasers. *New Journal of Physics*, 23(10):103015.

[McIntosh et al., 2016] McIntosh, L., Maheswaranathan, N., Nayebi, A., Ganguli, S., and Baccus, S. (2016). Deep learning models of the retinal response to natural scenes. In Lee, D., Sugiyama, M., Luxburg, U., Guyon, I., and Garnett, R., editors, *Advances in Neural Information Processing Systems*, volume 29. Curran Associates, Inc.

[Menzel et al., 2017] Menzel, M., Reckfort, J., Weigand, D., Köse, H., Amunts, K., and Axer, M. (2017). Diattenuation of brain tissue and its impact on 3d polarized light imaging. *Biomed. Opt. Express*, 8(7):3163–3197.

[Mishima and Izumida, 2017] Mishima, H. and Izumida, Y. (2017). Transition probability generating function of a transitionless quantum parametric oscillator. *Phys. Rev. E*, 96:012133.

[Mohseni et al., 2008] Mohseni, M., Rebentrost, P., Lloyd, S., and Aspuru-Guzik, A. (2008). Environment-assisted quantum walks in photosynthetic energy transfer. *The Journal of Chemical Physics*, 129(17):174106.

[Monras and Paris, 2007] Monras, A. and Paris, M. G. A. (2007). Optimal quantum estimation of loss in bosonic channels. *Phys. Rev. Lett.*, 98:160401.

[Morio and Goudail, 2004] Morio, J. and Goudail, F. (2004). Influence of the order of diattenuator, retarder, and polarizer in polar decomposition of mueller matrices. *Opt. Lett.*, 29(19):2234–2236.

[Muga et al., 2010] Muga, J. G., Chen, X., Ibáñez, S., Lizuain, I., and Ruschhaupt, A. (2010). Transitionless quantum drivings for the harmonic oscillator. *Journal of Physics B: Atomic, Molecular and Optical Physics*, 43(8):085509.

[Nagata et al., 2007] Nagata, T., Okamoto, R., O'Brien, J. L., Sasaki, K., and Takeuchi, S. (2007). Beating the standard quantum limit with four-entangled photons. *Science*, 316(5825):726–729.

[Nair, 2018] Nair, R. (2018). Quantum-limited loss sensing: Multiparameter estimation and bures distance between loss channels. *Phys. Rev. Lett.*, 121:230801.

[Naseem and Özgür E. Müstecaplıoğlu, 2019] Naseem, M. T. and Özgür E. Müstecaplıoğlu (2019). Quantum heat engine with a quadratically coupled optomechanical system. *J. Opt. Soc. Am. B*, 36(11):3000–3008.

[Nesse and Nesse, 2004] Nesse, W. and Nesse, P. (2004). *Introduction to Optical Mineralogy*. Oxford University Press.

[Newman et al., 2017] Newman, D., Mintert, F., and Nazir, A. (2017). Performance of a quantum heat engine at strong reservoir coupling. *Phys. Rev. E*, 95:032139.

[Niedenzu et al., 2018] Niedenzu, W., Mukherjee, V., Ghosh, A., Kofman, A. G., and Kurizki, G. (2018). Quantum engine efficiency bound beyond the second law of thermodynamics. *Nature Communications*, 9(1):165.

[Nogueira et al., 2013] Nogueira, K., Silva, J. B. R., Gonçalves, J. R., and Vasconcelos, H. M. (2013). Polarization and entanglement of photon-added coherent states. *Physical Review A*, 87(4):043821.

[Olaya-Castro et al., 2008] Olaya-Castro, A., Lee, C. F., Olsen, F. F., and Johnson, N. F. (2008). Efficiency of energy transfer in a light-harvesting system under quantum coherence. *Phys. Rev. B*, 78:085115.

[Ortega-Quijano and Arce-Diego, 2011] Ortega-Quijano, N. and Arce-Diego, J. L. (2011). Mueller matrix differential decomposition. *Opt. Lett.*, 36(10):1942–1944.

[Ossikovski, 2012] Ossikovski, R. (2012). Differential and product mueller matrix decompositions: a formal comparison. *Opt. Lett.*, 37(2):220–222.

[Ossikovski et al., 2008] Ossikovski, R., Anastasiadou, M., Ben Hatit, S., Garcia-Caurel, E., and De Martino, A. (2008). Depolarizing mueller matrices: how to decompose them? *physica status solidi (a)*, 205(4):720–727.

[Ossikovski et al., 2007] Ossikovski, R., Martino, A. D., and Guyot, S. (2007). Forward and reverse product decompositions of depolarizing mueller matrices. *Opt. Lett.*, 32(6):689–691.

[Pancotti et al., 2020] Pancotti, N., Scandi, M., Mitchison, M. T., and Perarnau-Llobet, M. (2020). Speed-ups to isothermality: Enhanced quantum thermal machines through control of the system-bath coupling. *Phys. Rev. X*, 10:031015.

[Panitchayangkoon et al., 2010] Panitchayangkoon, G., Hayes, D., Fransted, K. A., Caram, J. R., Harel, E., Wen, J., Blankenship, R. E., and Engel, G. S. (2010). Long-lived quantum coherence in photosynthetic complexes at physiological temperature. *Proceedings of the National Academy of Sciences*, 107(29):12766–12770.

[Panitchayangkoon et al., 2011] Panitchayangkoon, G., Voronine, D. V., Abramavicius, D., Caram, J. R., Lewis, N. H. C., Mukamel, S., and Engel, G. S. (2011). Direct evidence of quantum transport in photosynthetic light-harvesting complexes. *Proceedings of the National Academy of Sciences*, 108(52):20908–20912.

[Paris and Řeháček, 2004] Paris, M. and Řeháček, J., editors (2004). *Qubit Quantum State Tomography.* Springer Berlin Heidelberg, Berlin, Heidelberg.

[PARIS, 2009] PARIS, M. G. A. (2009). Quantum estimation for quantum technology. *International Journal of Quantum Information*, 07(supp01):125–137.

[Pedram et al., 2024a] Pedram, A., Besaga, V. R., Gassab, L., Setzpfandt, F., and Özgür E. Müstecaplıoğlu (2024a). Quantum estimation of the stokes vector rotation for a general polarimetric transformation.

[Pedram et al., 2024b] Pedram, A., Besaga, V. R., Setzpfandt, F., and Özgür E. Müstecaplıoğlu (2024b). Nonlocality enhanced precision in quantum polarimetry via entangled photons.

[Pedram et al., 2022] Pedram, A., Müstecaplıoğlu, O. E., and Kominis, I. K. (2022). Using quantum states of light to probe the retinal network. *Phys. Rev. Res.*, 4:033060.

[Peng and Zhao, 2023] Peng, Y. and Zhao, Y. (2023). Microfiber quantum sensors for protein measurement with quantum n00n state. *Sensors and Actuators B: Chemical*, 383:133616.

[Peres and Scudo, 2001a] Peres, A. and Scudo, P. F. (2001a). Entangled quantum states as direction indicators. *Phys. Rev. Lett.*, 86:4160–4162.

[Peres and Scudo, 2001b] Peres, A. and Scudo, P. F. (2001b). Transmission of a cartesian frame by a quantum system. *Phys. Rev. Lett.*, 87:167901.

[Perrin, 1932] Perrin, F. (1932). Théorie quantique des transferts d'activation entre molécules de même espèce. cas des solutions fluorescentes. In *Annales de Physique*, volume 10, pages 283–314. EDP Sciences.

[Perrin, 1927] Perrin, J. (1927). Fluorescence et induction moléculaire par résonance. *CR Hebd. Seances Acad. Sci*, 184:1097–1100.

[Peterson et al., 2019] Peterson, J. P. S., Batalhão, T. B., Herrera, M., Souza, A. M., Sarthour, R. S., Oliveira, I. S., and Serra, R. M. (2019). Experimental characterization of a spin quantum heat engine. *Phys. Rev. Lett.*, 123:240601.

[Petz, 1996] Petz, D. (1996). Monotone metrics on matrix spaces. *Linear Algebra and its Applications*, 244:81–96.

[Pezzè et al., 2018] Pezzè, L., Smerzi, A., Oberthaler, M. K., Schmied, R., and Treutlein, P. (2018). Quantum metrology with nonclassical states of atomic ensembles. *Rev. Mod. Phys.*, 90:035005.

[Phan et al., 2014] Phan, N. M., Cheng, M. F., Bessarab, D. A., and Krivitsky, L. A. (2014). Interaction of fixed number of photons with retinal rod cells. *Phys. Rev. Lett.*, 112:213601.

[Plenio and Huelga, 2008] Plenio, M. B. and Huelga, S. F. (2008). Dephasing-assisted transport: quantum networks and biomolecules. *New Journal of Physics*, 10(11):113019.

[Potočnik et al., 2018] Potočnik, A., Bargerbos, A., Schröder, F. A. Y. N., Khan, S. A., Collodo, M. C., Gasparinetti, S., Salathé, Y., Creatore, C., Eichler, C., Türeci, H. E., Chin, A. W., and Wallraff, A. (2018). Studying light-harvesting models with superconducting circuits. *Nature Communications*, 9(1):904.

[Pozas-Kerstjens et al., 2018] Pozas-Kerstjens, A., Brown, E. G., and Hovhannisyan, K. V. (2018). A quantum otto engine with finite heat baths: energy, correlations, and degradation. *New Journal of Physics*, 20(4):043034.

[Prucnal and Teich, 1982] Prucnal, P. R. and Teich, M. C. (1982). Multiplication noise in the human visual system at threshold: 2. probit estimation of parameters. *Biological Cybernetics*, 43(2):87–96.

[Quan et al., 2007] Quan, H. T., Liu, Y.-x., Sun, C. P., and Nori, F. (2007). Quantum thermodynamic cycles and quantum heat engines. *Phys. Rev. E*, 76:031105.

[Quan et al., 2005] Quan, H. T., Zhang, P., and Sun, C. P. (2005). Quantum heat engine with multilevel quantum systems. *Phys. Rev. E*, 72:056110.

[Raja et al., 2021] Raja, S. H., Maniscalco, S., Paraoanu, G. S., Pekola, J. P., and Gullo, N. L. (2021). Finite-time quantum stirling heat engine. *New Journal of Physics*, 23(3):033034.

[Ramella-Roman et al., 2020] Ramella-Roman, J. C., Saytashev, I., and Piccini, M. (2020). A review of polarization-based imaging technologies for clinical and preclinical applications. *Journal of Optics*, 22(12):123001.

[Rebentrost et al., 2009] Rebentrost, P., Mohseni, M., Kassal, I., Lloyd, S., and Aspuru-Guzik, A. (2009). Environment-assisted quantum transport. *New Journal of Physics*, 11(3):033003.

[Reingruber et al., 2013] Reingruber, J., Pahlberg, J., Woodruff, M. L., Sampath, A. P., Fain, G. L., and Holcman, D. (2013). Detection of single photons by toad and mouse rods. *Proceedings of the National Academy of Sciences*, 110(48):19378–19383.

[Restuccia et al., 2022a] Restuccia, S., Gibson, G. M., Cronin, L., and Padgett, M. J. (2022a). Measuring optical activity with unpolarized light: Ghost polarimetry. *Phys. Rev. A*, 106:062601.

[Restuccia et al., 2022b] Restuccia, S., Gibson, G. M., Cronin, L., and Padgett, M. J. (2022b). Measuring optical activity with unpolarized light: Ghost polarimetry. *Phys. Rev. A*, 106:062601.

[Reyes-Ayala et al., 2023] Reyes-Ayala, I., Miotti, M., Hemmerling, M., Dubessy, R., Perrin, H., Romero-Rochin, V., and Bagnato, V. S. (2023). Carnot cycles in a harmonically confined ultracold gas across bose-einstein condensation. *Entropy*, 25(2).

[Rezazadeh et al., 2017] Rezazadeh, F., Mani, A., and Karimipour, V. (2017). Secure alignment of coordinate systems using quantum correlation. *Phys. Rev. A*, 96:022310.

[Rezek and Kosloff, 2006] Rezek, Y. and Kosloff, R. (2006). Irreversible performance of a quantum harmonic heat engine. *New Journal of Physics*, 8(5):83.

[Riberi et al., 2023] Riberi, F., Paz-Silva, G. A., and Viola, L. (2023). Nearly heisenberg-limited noise-unbiased frequency estimation by tailored sensor design. *Phys. Rev. A*, 108:042419.

[Rieke and Baylor, 1998] Rieke, F. and Baylor, D. A. (1998). Single-photon detection by rod cells of the retina. *Rev. Mod. Phys.*, 70:1027–1036.

[Ringsmuth et al., 2012] Ringsmuth, A. K., Milburn, G. J., and Stace, T. M. (2012). Multiscale photosynthetic and biomimetic excitation energy transfer. *Nature Physics*, 8(7):562–567.

[Rivas and Luis, 2013] Rivas, A. and Luis, A. (2013). Su(2)-invariant depolarization of quantum states of light. *Phys. Rev. A*, 88:052120.

[Romero et al., 2017] Romero, E., Novoderezhkin, V. I., and van Grondelle, R. (2017). Quantum design of photosynthesis for bio-inspired solar-energy conversion. *Nature*, 543(7645):355–365.

[Roßnagel et al., 2014] Roßnagel, J., Abah, O., Schmidt-Kaler, F., Singer, K., and Lutz, E. (2014). Nanoscale heat engine beyond the carnot limit. *Phys. Rev. Lett.*, 112:030602.

[Rudnicki et al., 2020] Rudnicki, Ł., Sánchez-Soto, L. L., Leuchs, G., and Boyd, R. W. (2020). Fundamental quantum limits in ellipsometry. *Opt. Lett.*, 45(16):4607–4610.

[Rupp and Gruber, 2019] Rupp, A. I. K. S. and Gruber, P. (2019). Biomimetic groundwork for thermal exchange structures inspired by plant leaf design. *Biomimetics*, 4(4).

[Safranek et al., 2015] Safranek, D., Ahmadi, M., and Fuentes, I. (2015). Quantum parameter estimation with imperfect reference frames. *New Journal of Physics*, 17(3):033012.

[Sakitt, 1972] Sakitt, B. (1972). Counting every quantum. *The Journal of Physiology*, 223(1):131–150.

[Sanaka et al., 2004] Sanaka, K., Jennewein, T., Pan, J.-W., Resch, K., and Zeilinger, A. (2004). Experimental nonlinear sign shift for linear optics quantum computation. *Phys. Rev. Lett.*, 92:017902.

[Sarovar and Whaley, 2013] Sarovar, M. and Whaley, K. B. (2013). Design principles and fundamental trade-offs in biomimetic light harvesting. *New Journal of Physics*, 15(1):013030.

[Sasaki et al., 2002] Sasaki, M., Ban, M., and Barnett, S. M. (2002). Optimal parameter estimation of a depolarizing channel. *Phys. Rev. A*, 66:022308.

[Scarani et al., 2002] Scarani, V., Ziman, M., Štelmachovič, P., Gisin, N., and Bužek, V. (2002). Thermalizing quantum machines: Dissipation and entanglement. *Phys. Rev. Lett.*, 88:097905.

[Schmitz et al., 2020] Schmitz, D., Lippert, T., Amunts, K., and Axer, M. (2020). Quantification of fiber orientation uncertainty in polarized light imaging of the human brain. In Chen, G.-H. and Bosmans, H., editors, *Medical Imaging 2020: Physics of Medical Imaging*, volume 11312, page 1131239. International Society for Optics and Photonics, SPIE.

[Schupp, 1999] Schupp, P. (1999). On lieb's conjecture for the wehrl entropy¶of bloch coherent states. *Communications in Mathematical Physics*, 207(2):481–493.

[Schwinger, 1977] Schwinger, J. (1977). The majorana formula. *Transactions of the New York Academy of Sciences*, 38(1 Series II):170–184.

[Scovil and Schulz-DuBois, 1959] Scovil, H. E. D. and Schulz-DuBois, E. O. (1959). Three-level masers as heat engines. *Phys. Rev. Lett.*, 2:262–263.

[Scully, 2002] Scully, M. O. (2002). Quantum afterburner: Improving the efficiency of an ideal heat engine. *Phys. Rev. Lett.*, 88:050602.

[Scully et al., 2011] Scully, M. O., Chapin, K. R., Dorfman, K. E., Kim, M. B., and Svidzinsky, A. (2011). Quantum heat engine power can be increased by noise-induced coherence. *Proceedings of the National Academy of Sciences*, 108(37):15097–15100.

[Scully et al., 2003] Scully, M. O., Zubairy, M. S., Agarwal, G. S., and Walther, H. (2003). Extracting work from a single heat bath via vanishing quantum coherence. *Science*, 299(5608):862–864.

[Sheng et al., 2021] Sheng, J., Yang, C., and Wu, H. (2021). Realization of a coupled-mode heat engine with cavity-mediated nanoresonators. *Science Advances*, 7(50):eabl7740.

[Shi et al., 2016] Shi, L., Galvez, E. J., and Alfano, R. R. (2016). Photon entanglement through brain tissue. *Scientific Reports*, 6(1):37714.

[Shumovsky and Müstecaplıoğlu, 1998] Shumovsky, A. S. and Müstecaplıoğlu, Ö. E. (1998). Polarization of dipole radiation in quantum domain. *Physical Review Letters*, 80(6):1202–1203.

[Sidhu and Kok, 2020a] Sidhu, J. S. and Kok, P. (2020a). Geometric perspective on quantum parameter estimation. *AVS Quantum Science*, 2(1):014701.

[Sidhu and Kok, 2020b] Sidhu, J. S. and Kok, P. (2020b). Geometric perspective on quantum parameter estimation. *AVS Quantum Science*, 2(1):014701.

[Sim et al., 2012] Sim, N., Cheng, M. F., Bessarab, D., Jones, C. M., and Krivitsky, L. A. (2012). Measurement of photon statistics with live photoreceptor cells. *Phys. Rev. Lett.*, 109:113601.

[Singh and Müstecaplıoğlu, 2020] Singh, V. and Müstecaplıoğlu, O. E. (2020). Performance bounds of nonadiabatic quantum harmonic otto engine and refrigerator under a squeezed thermal reservoir. *Phys. Rev. E*, 102:062123.

[Singh et al., 2022] Singh, V., Singh, S., Abah, O., and Müstecaplıoğlu, O. E. (2022). Unified trade-off optimization of quantum harmonic otto engine and refrigerator. *Phys. Rev. E*, 106:024137.

[Snik and Keller, 2013] Snik, F. and Keller, C. U. (2013). *Astronomical Polarimetry: Polarized Views of Stars and Planets*, pages 175–221. Springer Netherlands, Dordrecht.

[Spohn, 2008] Spohn, H. (2008). Entropy production for quantum dynamical semigroups. *Journal of Mathematical Physics*, 19(5):1227–1230.

[Suri et al., 2018] Suri, N., Binder, F. C., Muralidharan, B., and Vinjanampathy, S. (2018). Speeding up thermalisation via open quantum system variational optimisation. *The European Physical Journal Special Topics*, 227(3):203–216.

[Sánchez-Soto et al., 2013] Sánchez-Soto, L. L., Klimov, A. B., de la Hoz, P., and Leuchs, G. (2013). Quantum versus classical polarization states: when multipoles count. *Journal of Physics B: Atomic, Molecular and Optical Physics*, 46(10):104011.

[Söderholm et al., 2012] Söderholm, J., Björk, G., Klimov, A. B., Sánchez-Soto, L. L., and Leuchs, G. (2012). Quantum polarization characterization and tomography. *New Journal of Physics*, 14(11):115014.

[Taylor and Bowen, 2016] Taylor, M. A. and Bowen, W. P. (2016). Quantum metrology and its application in biology. *Physics Reports*, 615:1–59. Quantum metrology and its application in biology.

[Teich et al., 1982a] Teich, M. C., Prucnal, P. R., Vannucci, G., Breton, M. E., and McGill, W. J. (1982a). Multiplication noise in the human visual system at threshold: 1. quantum fluctuations and minimum detectable energy. *J. Opt. Soc. Am.*, 72(4):419–431.

[Teich et al., 1982b] Teich, M. C., Prucnal, P. R., Vannucci, G., Breton, M. E., and McGill, W. J. (1982b). Multiplication noise in the human visual system at threshold: 3. the role of non-poisson quantum fluctuations. *Biological Cybernetics*, 44(3):157–165.

[Theeten and Aspnes, 1981] Theeten, J. B. and Aspnes, D. E. (1981). Ellipsometry in thin film analysis. *Annual Review of Materials Science*, 11(1):97–122.

[Tian et al., 2021] Tian, F., Zou, J., Li, L., Li, H., and Shao, B. (2021). Effect of inter-system coupling on heat transport in a microscopic collision model. *Entropy*, 23(4).

[Tinbergen, 1996] Tinbergen, J. (1996). *Polarization in astronomy*, page 27–44. Cambridge University Press.

[Tinsley et al., 2016] Tinsley, J. N., Molodtsov, M. I., Prevedel, R., Wartmann, D., Espigulé-Pons, J., Lauwers, M., and Vaziri, A. (2016). Direct detection of a single photon by humans. *Nature Communications*, 7(1):12172.

[Torrontegui et al., 2013] Torrontegui, E., Ibáñez, S., Martínez-Garaot, S., Modugno, M., del Campo, A., Guéry-Odelin, D., Ruschhaupt, A., Chen, X., and Muga, J. G. (2013). Chapter 2 - shortcuts to adiabaticity. In Arimondo, E., Berman, P. R., and Lin, C. C., editors, *Advances in Atomic, Molecular, and Optical Physics*, volume 62 of *Advances In Atomic, Molecular, and Optical Physics*, pages 117–169. Academic Press.

[Torrontegui et al., 2012] Torrontegui, E., Martínez-Garaot, S., Ruschhaupt, A., and Muga, J. G. (2012). Shortcuts to adiabaticity: Fast-forward approach. *Phys. Rev. A*, 86:013601.

[Toussaint et al., 2004] Toussaint, K. C., Di Giuseppe, G., Bycenski, K. J., Sergienko, A. V., Saleh, B. E. A., and Teich, M. C. (2004). Quantum ellipsometry using correlated-photon beams. *Phys. Rev. A*, 70:023801.

[Tran et al., 2015] Tran, D., Bourdev, L., Fergus, R., Torresani, L., and Paluri, M. (2015). Learning spatiotemporal features with 3d convolutional networks. In *2015 IEEE International Conference on Computer Vision (ICCV)*, pages 4489–4497.

[Tratzmiller et al., 2020] Tratzmiller, B., Chen, Q., Schwartz, I., Huelga, S. F., and Plenio, M. B. (2020). Limited-control metrology approaching the heisenberg limit without entanglement preparation. *Phys. Rev. A*, 101:032347.

[Tuncer and Müstecaplıoğlu, 2020] Tuncer, A. and Müstecaplıoğlu, O. E. (2020). Quantum thermodynamics and quantum coherence engines. *Turkish Journal of Physics*, 44:404–436.

[Turkpence et al., 2017] Turkpence, D., Altintas, F., Paternostro, M., and Özgür E. Müstecaplıoğlu (2017). A photonic carnot engine powered by a spin-star network. *Europhysics Letters*, 117(5):50002.

[Uchida et al., 2016] Uchida, K., Tanaka, M., and Okutomi, M. (2016). Coupled convolution layer for convolutional neural network. In *2016 23rd International Conference on Pattern Recognition (ICPR)*, pages 3548–3553.

[van der Velden, 1946] van der Velden, H. A. (1946). The number of quanta necessary for the perception of light of the human eye. *Ophthalmologica*, 111(6):321–331.

[Vega et al., 2021] Vega, A., Pertsch, T., Setzpfandt, F., and Sukhorukov, A. A. (2021). Metasurface-assisted quantum ghost discrimination of polarization objects. *Phys. Rev. Appl.*, 16:064032.

[Vepsäläinen et al., 2019] Vepsäläinen, A., Danilin, S., and Paraoanu, G. S. (2019). Superadiabatic population transfer in a three-level superconducting circuit. *Science Advances*, 5(2):eaau5999.

[Vepsäläinen and Paraoanu, 2020] Vepsäläinen, A. and Paraoanu, G. S. (2020). Simulating spin chains using a superconducting circuit: Gauge invariance, superadiabatic transport, and broken time-reversal symmetry. *Advanced Quantum Technologies*, 3(4):1900121.

[Villazon et al., 2019] Villazon, T., Polkovnikov, A., and Chandran, A. (2019). Swift heat transfer by fast-forward driving in open quantum systems. *Phys. Rev. A*, 100:012126.

[Vitkin et al., 2015a] Vitkin, A., Ghosh, N., and Martino, A. d. (2015a). *Tissue Polarimetry*, chapter 7, pages 239–321. John Wiley & Sons, Ltd.

[Vitkin et al., 2015b] Vitkin, A., Ghosh, N., and Martino, A. d. (2015b). *Tissue Polarimetry*, chapter 7, pages 239–321. John Wiley & Sons, Ltd.

[Wang et al., 2018] Wang, K., Wang, X., Zhan, X., Bian, Z., Li, J., Sanders, B. C., and Xue, P. (2018). Entanglement-enhanced quantum metrology in a noisy environment. *Phys. Rev. A*, 97:042112.

[Watrous, 2018] Watrous, J. (2018). *Unital Channels and Majorization*, page 201–249. Cambridge University Press.

[Wen et al., 2017] Wen, H., Shi, J., Zhang, Y., Lu, K.-H., Cao, J., and Liu, Z. (2017). Neural encoding and decoding with deep learning for dynamic natural vision. *Cerebral Cortex*, 28(12):4136–4160.

[Westner et al., 2021] Westner, B. U., Lubell, J. I., Jensen, M., Hokland, S., and Dalal, S. S. (2021). Contactless measurements of retinal activity using optically pumped magnetometers. *NeuroImage*, 243:118528.

[Wilkins and Dattani, 2015] Wilkins, D. M. and Dattani, N. S. (2015). Why quantum coherence is not important in the fenna–matthews–olsen complex. *Journal of Chemical Theory and Computation*, 11(7):3411–3419.

[Wolfgramm et al., 2010] Wolfgramm, F., Cerè, A., and Mitchell, M. W. (2010). Noon states from cavity-enhanced down-conversion: high quality and super-resolution. *J. Opt. Soc. Am. B*, 27(6):A25–A29.

[Wolfgramm et al., 2013a] Wolfgramm, F., Vitelli, C., Beduini, F. A., Godbout, N., and Mitchell, M. W. (2013a). Entanglement-enhanced probing of a delicate material system. *Nature Photonics*, 7(1):28–32.

[Wolfgramm et al., 2013b] Wolfgramm, F., Vitelli, C., Beduini, F. A., Godbout, N., and Mitchell, M. W. (2013b). Entanglement-enhanced probing of a delicate material system. *Nature Photonics*, 7(1):28–32.

[Yamamoto et al., 2022] Yamamoto, K., Endo, S., Hakoshima, H., Matsuzaki, Y., and Tokunaga, Y. (2022). Error-mitigated quantum metrology via virtual purification. *Phys. Rev. Lett.*, 129:250503.

[Yau et al., 1977] Yau, K., Lamb, T. D., and Baylor, D. A. (1977). Light-induced fluctuations in membrane current of single toad rod outer segments. *Nature*, 269(5623):78–80.

[Yin et al., 2022] Yin, Z., Li, C., Allcock, J., Zheng, Y., Gu, X., Dai, M., Zhang, S., and An, S. (2022). Shortcuts to adiabaticity for open systems in circuit quantum electrodynamics. *Nature Communications*, 13(1):188.

[Yoon et al., 2020] Yoon, S.-J., Lee, J.-S., Rockstuhl, C., Lee, C., and Lee, K.-G. (2020). Experimental quantum polarimetry using heralded single photons. *Metrologia*, 57(4):045008.

[Yu et al., 2021] Yu, W.-L., Li, T., Li, H., Zhang, Y., Zou, J., and Wang, Y.-D. (2021). Heat modulation on target thermal bath via coherent auxiliary bath. *Entropy*, 23(9).

[Yurke et al., 1986] Yurke, B., McCall, S. L., and Klauder, J. R. (1986). Su(2) and su(1,1) interferometers. *Phys. Rev. A*, 33:4033–4054.

[Zhang et al., 2022a] Zhang, J.-W., Zhang, J.-Q., Ding, G.-Y., Li, J.-C., Bu, J.-T., Wang, B., Yan, L.-L., Su, S.-L., Chen, L., Nori, F., Özdemir, Ş. K., Zhou, F., Jing, H., and Feng, M. (2022a). Dynamical control of quantum heat engines using exceptional points. *Nature Communications*, 13(1):6225.

[Zhang et al., 2024] Zhang, L., Besaga, V. R., Rühl, P., Zou, C., Heinemann, S. H., Wang, Y., and Setzpfandt, F. (2024). Probing polarization response of monolayer cell cultures with photon entanglement.

[Zhang et al., 2022b] Zhang, M., Yu, H.-M., Yuan, H., Wang, X., Demkowicz-Dobrzański, R., and Liu, J. (2022b). Quanestimation: An open-source toolkit for quantum parameter estimation. *Phys. Rev. Res.*, 4:043057.

[Zhang et al., 2015] Zhang, Z., Mouradian, S., Wong, F. N. C., and Shapiro, J. H. (2015). Entanglement-enhanced sensing in a lossy and noisy environment. *Phys. Rev. Lett.*, 114:110506.

[Zhou et al., 2020] Zhou, H., Ji, Y., Nie, X., Yang, X., Chen, X., Bian, J., and Peng, X. (2020). Experimental realization of shortcuts to adiabaticity in a nonintegrable spin chain by local counterdiabatic driving. *Phys. Rev. Appl.*, 13:044059.

[Zhou et al., 2018] Zhou, S., Zhang, M., Preskill, J., and Jiang, L. (2018). Achieving the heisenberg limit in quantum metrology using quantum error correction. *Nature Communications*, 9(1):78.

[Zou et al., 2017] Zou, Y., Jiang, Y., Mei, Y., Guo, X., and Du, S. (2017). Quantum heat engine using electromagnetically induced transparency. *Phys. Rev. Lett.*, 119:050602.

[Şener et al.,] Şener, M., Strümpfer, J., Hsin, J., Chandler, D., Scheuring, S., Hunter, C. N., and Schulten, K. Förster energy transfer theory as reflected in the structures of photosynthetic light-harvesting systems. *ChemPhysChem*, 12(3):518–531.